

Remote-sensing based assessment of post-fire changes in land surface temperature in Arctic-Boreal permafrost regions

Master Thesis

submitted by

Jenny Tamm

Supervisors:

Prof. Dr. Guido Grosse

Alexandra Runge

Potsdam, 17. June 2021

Erklärung

Hiermit versichere ich, dass ich die vorliegende Arbeit ohne Hilfe Dritter und ohne Zuhilfenahme anderer als der angegebenen Quellen und Hilfsmittel angefertigt habe. Die den benutzten Quellen wörtlich oder inhaltlich entnommenen Stellen sind als solche kenntlich gemacht.

Die „Richtlinie zur Sicherung guter wissenschaftlicher Praxis für Studierende an der Universität Potsdam (Plagiatsrichtlinie) - Vom 20. Oktober 2010“, im Internet unter

<https://www.uni-potsdam.de/am-up/2011/ambek-2011-01-037-039.pdf>,
habe ich zur Kenntnis genommen.

Potsdam, 17.6.2021

Ort, Datum

Unterschrift

Abstract

In recent years, wildfires became more predominant in northern high latitude permafrost regions. Arctic warming, as a consequence of climate change, causes drying of vegetation being more flammable and promotes lightning incidents. Hence, the Arctic wildfire season extents accompanied by an increase in wildfire frequency as well as burn severity (BS). By now, boreal forests are known as carbon sink but will become a carbon source, further enhancing climate change. Within loss in surface organic layer due to wildfires, the thermal conductivity of the soils changes, impacting the underlying permafrost. Thawing permafrost again releases greenhouse gasses, resulting in a positive feedback, further accelerating climate warming. Regarding these global consequences of wildfires, a better understanding of small regional scale processes is necessary for reliable future predictions.

Therefore, the aim of this study is to assess post-fire impacts on permafrost in the north-eastern Siberian Yana river catchment using remote sensing data. As previous studies announced a future spread of wildfires northward from Taiga to Tundra ecosystems, both will be considered in the study analysis to distinguish between their influence quantity.

In order to answer the research question, the effects on permafrost after wildfire were investigated using 9 Siberian fire sites including their accompanied control sites, along the Yana river. The yearly mean land surface temperature (LST), calculated from Landsat images over a time period from 2006-2020 for the summer months (June, July, August) serves therefore as data basis. Based on that, the Permafrost_CCI products including the yearly mean ground surface temperature (GST) and active layer thickness (ALT) between 1997-2018, were consulted for comparison purposes. Created time series of LST, GST and ALT were individually analyzed by visual interpretation, descriptive statistics and trend analysis. Finally, GST and ALT time series were correlated against LST time series. Additionally, the normalized burn ratio (NBR) was calculated from Landsat images to get supportive information about the BS and vegetation recovery, as these factors play a very important role in influencing the magnitude of permafrost variations due to wildfires.

The main findings show a correlation between LST and ALT resulting in a decrease of permafrost as the ALT increases within increasing LST after a wildfire. The coherence between LST and GST does not show unique results though, but result in increasingly warmer temperatures in the soil as well. Regarding differences between Taiga and Tundra ecosystems, impacts are causing a greater threat for permafrost in Tundra regions, especially in context with future predicted increase of wildfire frequency and BS. Nevertheless, studying permafrost remains still challenging due to the remoteness of the study area, resulting in a lack of in-situ data, as well as remote sensing data.

Zusammenfassung

In den letzten Jahren haben Waldbrände in den Permafrostgebieten nördlicher hoher Breiten immer häufiger zugenommen. Die Erwärmung der Arktis als Folge des Klimawandels führt dazu, dass die Vegetation durch Austrocknung entzündlicher wird und Blitzeinfälle begünstigt werden. Daher verlängert sich die arktische Waldbrandsaison, begleitet von einer Zunahme der Häufigkeit von Waldbränden sowie deren Ausmaß. Inzwischen sind boreale Wälder als Kohlenstoffsенke bekannt, werden aber zu einer Kohlenstoffquelle, die den Klimawandel weiter verstärkt. Durch den Verlust der organischen Oberflächenschicht durch Waldbrände ändert sich die Wärmeleitfähigkeit der Böden, was sich auf den darunter liegenden Permafrostboden auswirkt. Das Auftauen des Permafrosts setzt wieder Treibhausgase frei, was zu einer positiven Rückkopplung führt und die Klimaerwärmung weiter beschleunigt. Im Hinblick auf diese globalen Folgen von Waldbränden, ist ein besseres Verständnis der kleinräumigen Prozesse notwendig, um zuverlässige Zukunftsvorhersagen treffen zu können.

Das Ziel dieser Studie ist es daher, die Auswirkungen nach einem Waldbrand auf den Permafrost im nordöstlichen sibirischen Yana Flusseinzugsgebiets mit Hilfe von Fernerkundungsdaten zu bewerten. Da frühere Studien eine zukünftige Ausbreitung von Waldbränden nach Norden von Taiga- bis Tundra-Ökosystemen angekündigt haben, werden beide in der Studienanalyse berücksichtigt, um zwischen ihrer Einflussgrößen zu unterscheiden.

Um die Forschungsfrage zu beantworten, wurden die Auswirkungen auf den Permafrost nach einem Waldbrand anhand von 9 sibirischen Feuerstellen und deren Kontrollstellen entlang des Yana-Flusses untersucht. Als Datengrundlage dient daher die jährliche mittlere Landoberflächentemperatur (LST), berechnet aus Landsat-Bildern über einen Zeitraum von 2006-2020 für die Sommermonate (Juni, Juli, August). Darauf aufbauend wurden zu Vergleichszwecken die Permafrost_cci Produkte, einschließlich der jährlichen mittleren Bodenoberflächentemperatur (GST) und der aktiven Permafrost Schichtdicke (ALT) zwischen 1997-2018, herangezogen. Erstellte Zeitreihen von LST, GST und ALT wurden einzeln durch visuelle Interpretation, deskriptive Statistik und Trendanalyse analysiert. Schließlich wurden GST- und ALT-Zeitserien mit LST-Zeitserien korreliert. Darüber hinaus wurde die normalisierte Verbrennungsrate (NBR) aus Landsat-Bildern berechnet, um unterstützende Informationen über den Verbrennungsgrad (BS) und die Vegetationserholung zu erhalten, da diese Faktoren eine sehr wichtige Rolle bei der Beeinflussung des Ausmaßes der Permafrostvariationen aufgrund von Waldbränden spielen.

Die wichtigsten Ergebnisse zeigen eine Korrelation zwischen LST und ALT, welche zu einer Abnahme des Permafrosts führt, da nach einem Flächenbrand ALT mit ansteigender LST zunimmt. Die Kohärenz zwischen LST und GST zeigt jedoch keine eindeutigen Ergebnisse, führt aber auch zu zunehmend wärmeren Temperaturen im Boden. Was die Unterschiede zwischen Taiga- und Tundra-Ökosystemen betrifft, so führen die Auswirkung zu einer größeren Bedrohung für den Permafrost in Tundra-Regionen, insbesondere im Zusammenhang mit der künftig prognostizierten Zunahme von Waldbränden und BS. Dennoch bleibt die Untersuchung von Permafrost aufgrund der Abgelegenheit des Untersuchungsgebiets eine Herausforderung, was zu einem Mangel an In-situ-Daten sowie Fernerkundungsdaten führt.

Contents

1. Introduction	1
1.1. Current status of satellite-derived LST	3
1.2. Permafrost	4
1.3. Siberian forests and forest fires	6
1.3.1. Relation to permafrost	7
1.4. Objectives	8
2. Study area and data acquisition	9
2.1. Study area	9
2.2. Data	11
2.2.1. Landsat imagery	11
2.2.2. Auxiliary data	12
3. Method	14
3.1. Pre-processing	14
3.2. Multispectral index calculation	15
3.3. Change detection to extract fire areas	16
3.4. Retrieval of Land surface temperature	17
3.5. Statistical analysis	19
4. Results	21
4.1. Visual interpretation of time series	21
4.1.1. Yearly mean summer LST	21
4.1.1.1. Yearly mean summer NBR and dNBR	24
4.1.2. Yearly mean GST	27
4.1.2.1. Residual analysis of GST	29
4.1.3. Yearly mean ALT	30
4.1.3.1. Residual analysis of ALT	32
4.2. Trend analysis	32
4.2.1. Yearly summer mean LST	32
4.2.2. Yearly mean GST	33
4.2.3. Yearly mean ALT	34
4.3. Correlation analysis	34

5. Discussion	36
5.1. LST	36
5.1.1. NBR and dNBR	37
5.2. GST and correlation with LST	39
5.3. ALT and correlation with LST	41
6. Conclusion and outlook	43
A. Values and coefficients	44
B. Graphs and tables	45
Bibliography	55

List of Figures

1.1. Amount of wildfires in the Yana river catchment from 1999-2020.	3
1.2. Schematic permafrost soil profile.	5
1.3. Tundra post-wildfire effects on the soil temperature, ALT and permafrost based on Heim et al. (2021).	8
2.1. Study area including the selected wildfires.	9
2.2. Overview of available Landsat images for the entire study site over the time period from 2006 to 2020.	12
3.1. Processing chain divided into data basis, including pre-processing, index calculation, as well as fire area detection and LST calculation, together with the statistical analysis as second part.	14
3.2. History of Tundra fire (2014) pixels, experiencing a period of relative stability, rapid loss of vegetation due to wildfire, and subsequent regeneration.	17
4.1. LST time series, together with dLST. The gray bar marks the year of fire disturbance, while the red and blue areas mark the standard deviation for the fire and control area, respectively.	22
4.2. NBR time series of fire areas, with recovery rate colored as the blue area in between.	24
4.3. Spatio-temporal BS for each wildfire.	26
4.4. GST time series, together with dGST. The gray bar marks the year of fire disturbance.	27
4.5. GST residuals over the time period from 1997-2018.	29
4.6. ALT time series, together with dALT. The gray bar marks the year of fire disturbance.	30
4.7. ALT residuals over the time period from 1997-2018.	32
B1. Yearly summer mean LST time series of fire and control areas.	46
B2. Yearly summer mean NBR time series of fire and control areas.	47
B3. Yearly mean GST time series of fire and control areas.	48
B4. Visualization of GST residuals.	49
B5. Yearly mean ALT time series of fire and control areas.	51
B6. Visualization of ALT residuals.	52
B7. Correlation of LST and GST.	54
B8. Correlation of LST and ALT.	55

List of Tables

1.1. Permafrost zones (Brown et al., 1997).	4
2.1. List of studied wildfires and their characteristics. The landcover classes are subdivided in 90: Open needleleaved deciduous or evergreen forest; 110: Mosaic Forest-Shrubland/Grassland; 120: Mosaic Grassland/Forest-Shrubland; 150: sparse vegetation; 200: Bare areas (GLOB Cover 2009 Land Cover Map).	10
3.1. Burn severity classes by Key and Benson (2006).	16
4.1. Summary of LST RMSE statistics, including mean, min and max of the study areas with corresponding p-values and the mean dLST before and after the fire event.	23
4.2. Summary of NBR RMSE statistics, including mean, min and max of the study areas with corresponding p-values and the mean difference (dNBR) before and after the fire event.	25
4.3. Summary of GST RMSE statistics, including mean, min and max of the study areas with corresponding p-values and the mean difference (dGST) before and after the fire event.	28
4.4. Summary of ALT RMSE statistics, including mean, min and max of the study areas with corresponding p-values and the mean difference (dALT) before and after the fire event.	31
4.5. LST Sen's slopes before and after the fire event for the fire and control areas, together with p-value and intercept.	33
4.6. GST Sen's slopes before and after the fire event for the fire and control areas, together with p-value and intercept.	33
4.7. ALT Sen's slopes before and after the fire event for the fire and control areas, together with p-value and intercept.	34
4.8. Correlation results of yearly mean LST with GST and ALT.	34
A1. Parameters used for the LT algorithm.	44
A2. Coefficients used to calculate the AFs.	44
B1. Residuals of GST.	50
B2. Residuals of ALT.	53

Nomenclature

AFs	Atmospheric functions
ALT	Active layer thickness
BT	Brightness temperature
DEM	Digital elevation model
DN	Digital numbers
dNBR	Difference Normalized Burn Ratio
GEE	Google Earth Engine
GST	Ground surface temperature
LSE	Land surface emissivity
LST	Land surface temperature
LT	Landsat-based detection of Trends in Disturbance and Recovery algorithm (LandTrendr)
LTS	Landsat image time series
MWA	Mono Window Algorithm
NBR	Normalized burn ratio
NCAR	National Center for Atmospheric Research
NCEP	National Centers for Environmental Prediction
NDVI	Normalized difference vegetation index
NHL	Northern hemisphere latitude
NIR	Near infrared
RMSE	Root Mean Squared Error
RTE	Radiative Transfer Equation
SCA	Single Channel Algorithm

Nomenclature

SR	Surface reflectance
SRTM	Shuttle Radar Topography Mission
SWA	Split Window Algorithm
SWIR	Short wave infrared band
T-S	Theil-Sen regression method
TIR	Thermal infrared
TOA	Top-of-Atmosphere
WMO	World Meteorological Organization
WV	waper vapor

1. Introduction

Due to climate change, the Arctic has warmed at more than twice to global average over the last 30 years (Cohen et al., 2014), also known as the Arctic amplification. According to Northern High Latitudes weather stations, the annual mean surface air temperatures have risen by almost 2°C since 1900 (Serreze and Barry, 2011). This becomes noticeable in a period of unusually high temperatures, Siberia experienced in the first 6 months of 2020, hitting record-breaking temperatures of 38°C in the town of Verkhoyansk (World Meteorological Organization (WMO)). The phenomenon of the Arctic amplification is evidenced by shrinking sea ice cover, decreasing land snow cover by 7-11% during 1970-2010 in the northern Hemisphere (Brown and Robinson, 2011), permafrost thawing and may also lead to an increase of wildfire occurrence (McCarty et al., 2020).

Wildfires are the most widespread ecosystem disturbance in the Boreal biome (Gibson et al., 2018). Their regeneration strongly depends on a complex interplay between numerous drivers in the pre- and post-fire habitat (Chu et al., 2017) and it may take decades to return to pre-fire conditions, if ever possible. The assessment of these drivers, such as vegetation, landforms, fire regimes, hydrology, regional climate, soil properties and the time since fire, states the basis in understanding the long-term effects of fire disturbances. Chu et al. (2017) found out, that, especially in larch forests, the primary controllers were burn severity and water content.

Especially the Sakha Republic of Siberia has been one of the most active fire regions in the last 2-3 years. According to Russia's Federal Forestry Agency, in 2019 almost three million hectares of land were considered being affected by fires in Siberia. Long-term statistics of annual wildfires show that they have strongly increased in scale and intensity, showing a positive trend ($R^2 = 0.69$ and 0.47 , respectively; $p < 0.05$; Ponomarev et al. (2016)). The highest correlation of air temperature anomalies and annual number of fires occurred during June-July ($r = 0.67$; Ponomarev et al. (2016)). Therefore, correlations between precipitation anomalies within all Siberia and the annual burned area, were not significant but might be relevant at a smaller timescale Ponomarev et al. (2016). For example in central Siberia and the Trans-Baikal region a relation between the occurrence of extreme wildfire events and soil moisture, same as precipitation anomalies, was found (Bartsch et al., 2009; Forkel et al., 2012).

Another sign for rapid changes in the Arctic region is the occurrence of an even longer Arctic wildfire season due to temperature rise (McCarty et al., 2020). Although the typical Arctic fire season begins in July and ends in August (+/- a few weeks), many 2020 fires were already detected in May, even though the aboveground vegetation was not yet flammable (McCarty et al., 2020). This may be due to the occurrence of zombie fires, which are fires of previous growing seasons, smouldering below the surface for months or even years (Hu et al., 2018). Thus, they are independent from ignition sources such as lightning or campfires.

Additionally, the shortening of the frozen season in recent years have resulted in Arctic greening

1. Introduction

(Kim et al., 2012). This leads to a future projection in which at least half of the vegetated areas will shift to a different vegetation class until 2050 (Barrett et al., 2012; Pearson et al., 2013). The shift in vegetation, as well as the rise in temperatures, may lead to wildfires moving northward. Northern tundra landscapes are typically too cold, wet and icy to burn, but the hot and dry weather dried out its vegetation, enabling fires (McCarty et al., 2020). If wildfires were to become a regular occurrence on the thawing tundra, they could reshape entire ecosystems dramatically, which could lead to new species taking over, and perhaps, causing even more fires to evolve. It still remains unclear how far north fires are spreading and what kind of ecosystem states the prime ignition source (Stone, 2020).

Boreal forests encompass $\sim 30\%$ ($\sim 1,135$ Mha) of the global forest area (Brandt et al., 2013; Gauthier et al., 2015) and are a significant large sink of carbon dioxide, usually helping to mitigate the impact of global climate change. However, due to the increase in wildfire occurrence, much more toxic gases and pollutants are released into the atmosphere, converting the carbon sink to a source for greenhouse gasses (Guo et al., 2019). Arctic fires can release around 50 megatonnes of carbon dioxide in June alone (WMO). This can be compared to Sweden's total annual emissions (WMO).

Depending on the drivers, previous studies have indicated, that forest wildfires could result in irreversible degradation of permafrost (Gibson et al., 2018). Still, the impacts of wildfires on ecosystems and permafrost ecosystems in general are not well understood. A central question is how long and to which degree wildfires influence the thermal regime (Gibson et al., 2018).

Due to this knowledge gap and the complex interactions between wildfires and permafrost, their consequences are expected to be strongly underestimated in climate change scenarios and projections of future permafrost thawing. Considering recent trends of increasing fire activity, more attention should be paid to the research on this topic.

The aim of this study is to assess the impacts of wildfires on the permafrost environment in the Siberian Yana river catchment with the help of remote sensing techniques. This area is extremely affected by a strong increase of wildfires in recent years (Figure 1.1). As wildfires lead to an increase in canopy temperatures, it can be detected by remote sensing measurements in the thermal infrared (TIR) as a deviation of land surface temperatures (LST). A positive relationship is expected between LST as data basis, permafrost and ground surface temperatures (GST), same as active layer thickness (ALT). Due to the expansion of wildfires further north, both Taiga and Tundra wildfires will be compared.

1. Introduction

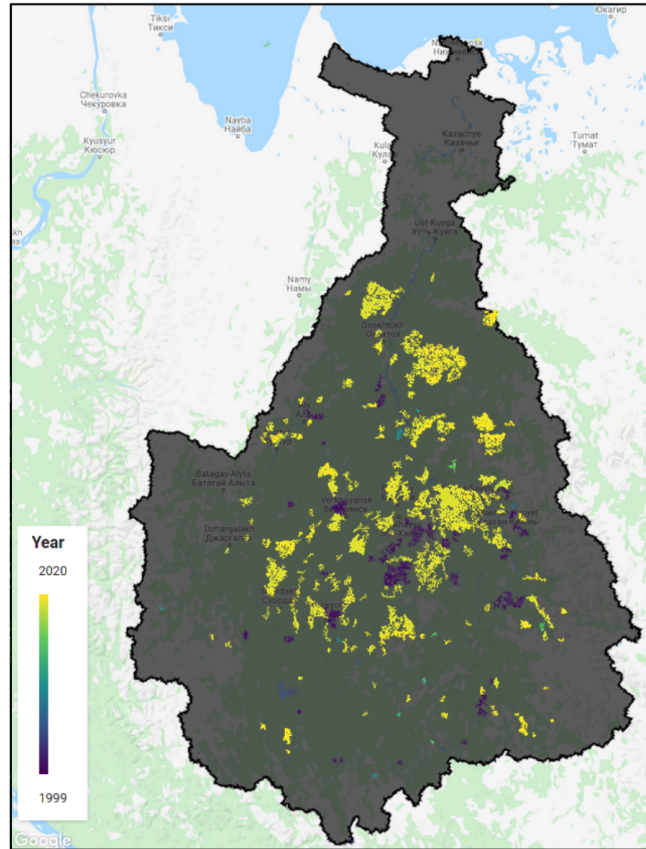


Figure 1.1.: Amount of wildfires in the Yana river catchment from 1999-2020.

1.1. Current status of satellite-derived LST

LST is the radiative skin temperature of the surface and states one of the key parameter for various scientific disciplines, as it describes the interaction (e.g water/energy exchange) between the land surface and the atmosphere (Li et al., 2013a). It can be estimated from the Top-of-Atmosphere brightness temperatures gained from geostationary satellites. An accurately understanding of LST at both, global and regional scales improves the evaluation of land surface-atmosphere processes, providing a valuable description of the surface state in regard to physical properties (e.g vegetation, soil moisture).

Due to the importance of LST, there is strong interest in developing algorithms to measure satellite-based LST. Typical algorithms are the Mono Window Algorithm (MWA), Radiative Transfer Equation (RTE) method, Single Channel Algorithm (SCA) and the Split Window Algorithm (SWA) (Parastatidis et al., 2017; Vlassova et al., 2014; Wang et al., 2015). Their accuracy is primarily constituted by the quality of the Land Surface Emissivity (LSE) and radiometric measurements (Sekertekin and Bonafoni, 2020). Due to the variability of the Earth surfaces and the necessary knowledge about the atmosphere, LSE, sensor specifications (e.g. viewing angle, spectral and spatial resolution) and meteorological states, the retrieving of LST remains still challenging (Li et al., 2013a; Sobrino et al., 2008). Until now, no universal method reliably providing accurate LSTs from all satellite thermal infrared (TIR) data exist (Li et al., 2013b).

Remote sensing techniques enable the detection and monitoring of Arctic changes in vegetation for a

1. Introduction

variety of spatial and temporal scales. Aircraft observations are constrained by logistical difficulties in remote Arctic locations, inclement weather and cost, resulting in a lack of data consistency. In contrast, satellites are able to theoretically cover large regions on a regular basis, but also faces a number of challenges (Stow et al., 2004). This includes frequent cloud cover conditions concerning optical remote sensing systems. By contrast, radar systems have the benefit of providing data regardless of cloud cover, but are influenced by a different set of associated problems, such as terrain effects and view angle dependencies (Stow et al., 2004).

1.2. Permafrost

Permafrost is a ground layer (sediment, soil, rocks) that remains below 0°C for at least two consecutive years (French, 1999). It captures a fifth of the global northern land surface and is therefore an essential component of the cryosphere (Brown et al., 1997). Depending on the percentages of frozen ground in a specific area, the Permafrost is segmented into different zones (Table 1.1):

Continuous	Discontinuous	Sporadic	Isolated
100 - 90 %	90 - 50 %	50 - 10 %	< 10 %

Table 1.1.: Permafrost zones (Brown et al., 1997).

The top of the permafrost is set by the overlying base of the active layer, while the base is given by a ground temperature greater than 0°C at depth (Figure 1.2). The active layer at the surface thaws during the warmer summer months and freezes again in autumn each year. It plays a very important role in preservation of the permafrost, as it represents the boundary between permafrost and the atmosphere. Together with the vegetation in summer and snow cover in winter, the active layer drives the transmission of heat, moisture or gases from and to the permafrost and the atmosphere respectively. For the assessment of permafrost degradation an understanding of the ALT dynamics in correlation to the thermal state of permafrost is crucial (Westermann et al., 2015). The more the ALT increases on average (e.g due to longer and warmer summer), the more difficult it is to freeze again in winter, leading to a shrinking of the permafrost layer in total.

1. Introduction

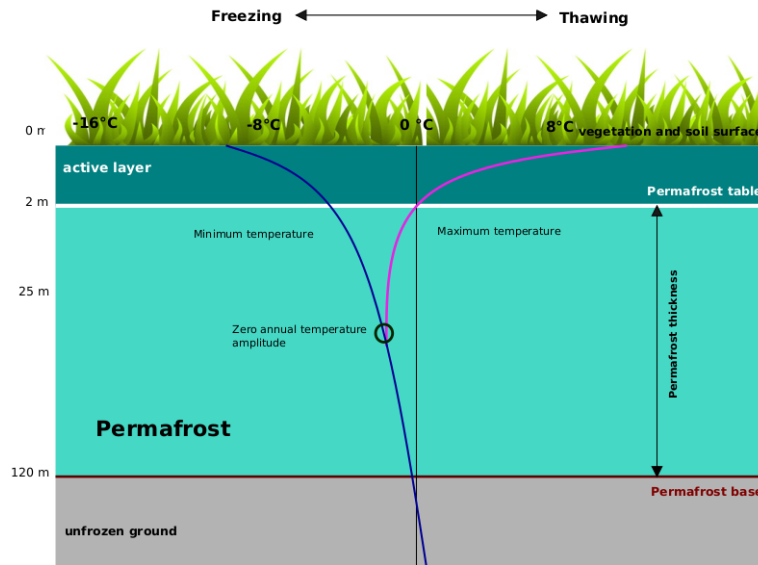


Figure 1.2.: Schematic permafrost soil profile.

Most of the northern regions with frozen ground have been experiencing an increase in temperatures of permafrost, which are reported by the IPCC Special Report on the Ocean and Cryosphere in Changing Climate (Pörtner et al., 2019). Accordingly, averaged temperatures across high-mountain and polar regions have reached a record high since the 1980s showing a recent warming of $0.29^{\circ}\text{C} \pm 0.12^{\circ}\text{C}$ from 2007–2016 (Zhao et al., 2019). This results in future projections that show a drastic reduction of permafrost distribution (Pörtner et al., 2019). The thawing of permafrost has strong local and global impacts on the environment. Locally, it affects ecosystems, landscape, economy and topography. Warming and thawing of frozen ground weakens its physical stability, which causes slope instabilities, landslides, thaw slumps, and erosion (Philipp et al., 2021). Hence, permafrost thawing has also an impact on human infrastructure and could result in damaged railroads, buildings or pipelines (Hinzman et al., 2005).

On a global scale, thawing permafrost accelerates global warming due to the irreversible Permafrost-CO₂-feedback cycle. According to recent estimates, permafrost stores almost twice the amount of carbon than the atmosphere (1460-1600 billion tones; Schuur et al., 2015). A continuing degradation of Permafrost could enhance the release of greenhouse gases, resulting in a positive feedback as these gases further accelerate climate change (Pörtner et al., 2019). Scientists argue that the Arctic greening, as a result of climate change, could be seen as carbon sink to a certain degree. But so far, there is still little agreement on the role of northern hemisphere latitudes (NHL) vegetation in CO₂ absorption (Abbott et al., 2016; Trofaier et al., 2017; Voigt et al., 2017). An increase of organic carbon release of up to 75% by the year 2100 due to collapsing coastlines and Arctic rivers is predicted by Abbott et al. (2016). Together with carbon emissions caused by wildfires, he assumes a carbon increase multiplied by a factor four. Regardless of the warming scenario, both boreal forests as well as permafrost regions might become carbon sources by the end of the century. However, a reduction of human emission rates could potentially still avoid 65–85% of permafrost carbon release (Abbott et al., 2016).

1.3. Siberian forests and forest fires

Wildfires are a crucial element in controlling the dynamics of forest ecosystem in the circumpolar Boreal zone. An enhanced understanding of their direct and indirect, short- to long term impacts on permafrost LST coupling is explicitly meaningful for future prediction of changes in water cycles, nutrient and carbon in regard to global warming. Next to the warming triggered by permafrost thaw, the global warming fastens due to the absence of CO₂ emitting plants.

Siberian forests are rich in accumulated fuel and provide perfect conditions for forest fires. Additionally, humidity, precipitation, drying period, forest type, air temperature, topography (elevation, slope steepness, aspect), solar radiation and the ignition source (human-caused or lightning) are important factors to light a fuel. Elevation in particular influences lightning frequency, fuel load and precipitation. The aspect affects the fuel condition because steeper south-facing slopes tend to dry faster than others. Moreover, with an increase in slope, the speed of the fire seems to increase as well (Kharuk et al., 2007). As the solar radiation decreases from south to north and fuels in the north generally receive less heat, Tundra wildfires were relatively rare in the past (Kharuk et al., 2016).

Regarding the ignition source, a strong correlation in fire activity and proximity to roads and human settlements has been observed (Kovacs et al., 2004). Again, elevation plays a crucial role: the higher the latitude, the lower the likelihood of human-caused fires due to less population density. Therefore, lightning is the main cause of fires ($\leq 90\%$) in the northern latitudes, which occur especially during rain-less anticyclonic periods (Ivanova et al., 2010). Moreover, lightning events may cause fires at several sites at once due to multiple parallel ignitions, which enhances the amount of fire events. Global warming was predicted to likely lead to an increase in fire frequency, fire intensity and larger fire size, as it causes an increase in the frequency of lightning strike by roughly 12% per 1C° of warming (Heim et al., 2021; Romps et al., 2014). In fact, an increase of Tundra fires could already been observed (Heim et al., 2021; Moritz et al., 2012), which in turn will increase climate warming. While short-term effects of fires on ecosystems are already well documented (Heim et al., 2021), it is crucial to understand their long-term effects for sound future predictions.

For meaningful analysis, it is necessary to distinguish between forest stands that have been affected by fire and stands that were killed by fire, as the effects of a fire are influenced by its type, intensity and the type of forest. There are three types of fires: surface, crown, and peat fires. The majority of forest fires in Siberia (90%) are low-intensity surface fires (de Groot et al., 2013; Kharuk and Ponomarev, 2017) which primarily burn surface litter and the forest floor. Especially pine and larch stands are resistant to forest fires which do not result in a significant stand mortality (Krylov et al., 2014). Surface fires are further divided into runaway (early spring) and sustained (summer, autumn) fires based on their speed and combustion characteristics. Runaway fires causes a maturity of only the upper litter layers, usually damaging no trees. Except for young coniferous stands, surface fires can turn into crown fires. Therefore, sustained surface fires can cause ground cover and undergrowth mortality, root damage and damage on trunks of trees. Since the root habitat zone within the permafrost zone is quite shallow, sustained surface fires are the main cause of forest stand mortality. Crown fires are the most intense type of fire: They start to spread from the surface, burn along the entire length of trees, including the top, and take over the entire forest canopy. High-intensity crown fires occur in closed-

1. Introduction

forest stands mostly in the middle and southern taiga. In the case of crown fires, forest mortality is inevitable; this occurs in 8–10% of the total fire-affected area (Ponomarev et al., 2018a,b).

Half of Arctic wildfires in May and June occur on peatland (Hugelius et al., 2020). As most of the Boreal forests recover from wildfires, peatland fires are problematic since they do not regrow quickly after the fire, resulting in a permanent carbon loss to the atmosphere. Due to the thick layers of peat or other soil rich organic matter, burning through those layers often causes fires to sustain for a long time. Although, peatlands helped to cool the climate for thousands of years by storing carbon as they accumulate, they might probably become a net carbon source by the end of the century (Hugelius et al., 2020).

As larch forests are the dominant forest communities in the Siberian Taiga, the majority (>50%) of wildfires were observed in larch stands (Ponomarev et al., 2016). Due to their low crown closure, the main fuel source are not the trees themselves but lichen and moss, spreading surface fires (Sapozhnikov and Krechetov., 1982). Shrub extent increases in the Tundra due to climate change and may be enhanced due to wildfires (Hollingsworth et al., 2021). The increase in lichen and moss matrix and decrease in forest causes an increase in mean burned area up to the Arctic circle. The burned area provides perfect environmental conditions for larch, as it is extremely shade-intolerant and regenerates poorly under a closed canopy. This way wildfires contribute to the occurrence of larch, which is why they are considered as pyrophytic species. But the impacts of wildfire vary due to the prevailing forest type for other global permafrost regions.

1.3.1. Relation to permafrost

For the development of permafrost, the Taiga itself is an important contributing factor. The intact forest canopy, summer months insulating moss cover and storage of forest litter leads to a cooling of the underlying soil. The thickness of organic layer has a key influence on permafrost and vegetation changes.

Due to the dark ash from the burn out of ground cover, the surface albedo significantly reduces, resulting in an alteration of the division of energy sources and the net heat balance on the ground for several years. This in turn leads to ground warming, as the absorption of shortwave radiation increases and will be transferred into sensible heat (Ponomarev et al., 2020). Additionally, the increase of emitted longwave radiation strongly supports the increase in land surface temperature. Furthermore, the lack of an intact vegetation cover produces a deeper and more efficient insulating layer of snow stack during winter.

Recent studies show a typical pattern of permafrost recovery after wildfires (Figure 1.3). Permafrost seems to have been stable after fires in most areas, with short-term changes immediately after the fire, returning to pre-fire conditions within a few decades (Rocha et al., 2012). This can be related to vegetation succession (Heim et al., 2021). The impact of wildfires on permafrost and recovery is very complex, depending on the landscape position, organic layer thickness, soil type, burn severity, snow, drainage – and soil moisture conditions, pre-fire permafrost and vegetation conditions. To mention an example, fires on a dry high area with coarse soil will be more vulnerable than a poorly drained lowland, high vegetated area.

1. Introduction

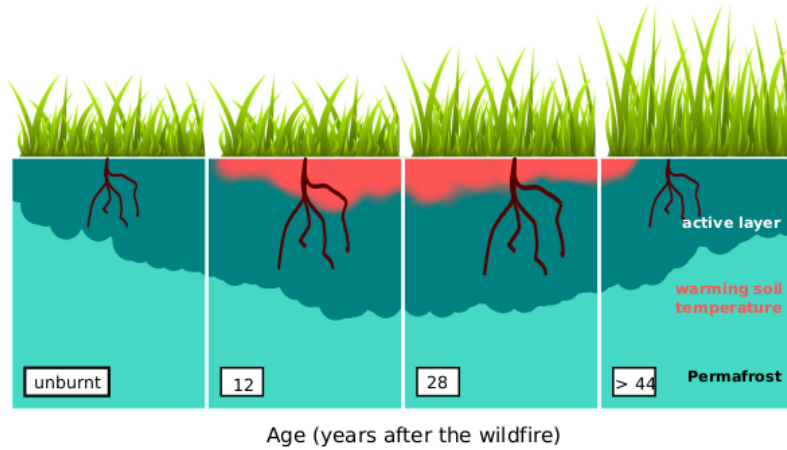


Figure 1.3.: Tundra post-wildfire effects on the soil temperature, ALT and permafrost based on Heim et al. (2021).

1.4. Objectives

The aim of this work is to study the relation between post-fire LST and permafrost in Siberia, regarding a south-northward transect from Taiga to Tundra.

Therefore, the following objectives have been set:

1. Remote-sensing based assessment of post-fire changes in LST
2. to analyze the relationship between LST and BS (NBR, dNBR) to determine the vegetation recovery rate
3. to visualize the temporal thermal state (GST) and ALT of permafrost
4. to evaluate the relationship between LST and permafrost parameters (GST/ALT)

2. Study area and data acquisition

2.1. Study area

The study area is located around the Yana River basin, between 65° to 71°N and 131° to 141°E in the Sakha Republic (northeastern Siberia, Figure 2.1). The river is 872 km long and the catchment covers an area of 238.000 km², crossing two of the world biomes – Taiga and Tundra. Topographically, the study area is enclosed by the Chersky Range in the south/ south-east, the Verkhoyansk Mountains as part of the East-Siberian Mountains in the west/ south-west, the Laptev sea in the north and East-Siberian Lowlands in the east. The entire area is characterized by continuous permafrost.

To study the effects of wildfires depending on the latitude, fire scars were selected in a south-north transect. The transect begins 150 km south of Batagay (67°39′30″N, 134°38′40″E) as the origin of consideration, to 420 km north of it along the western and eastern banks of the Yana River. Al together, 9 wildfires matching the criteria of showing the longest possible time series (6-11 years) after the fire, were observed during 2006 to 2020 (Table 2.1). They vary clearly in size between 8 km² to 243 km² and elevation from ca. 300-950 m of the southernmost fire scar and ca. 10-60 m to the north. As Tundra fires are rather unusual until now, just one fire could be included in the study.

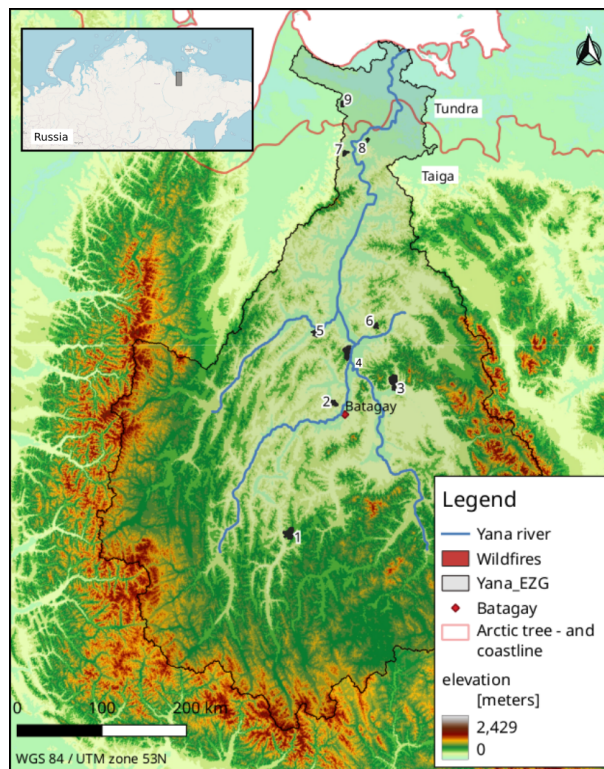


Figure 2.1.: Study area including the selected wildfires.

2. Study area and data acquisition

fire	biome	year of fire	size [km ²]	elevation [m]	landcover
1	Taiga	2009	60	301-949	90,110,120,150
2	Taiga	2014	31	276-401	90,110,120,150
3	Taiga	2014	62	162-738	90,110,120,150
4	Taiga	2009	243	147-703	90,110,120,150
5	Taiga	2009	22	95-409	90,110,120,150
6	Taiga	2009	50	351-631	110,120,150,200
7	Taiga	2010	14	74-302	150
8	Taiga	2014	8	58-114	110,120,150
9	Tundra	2013	11	58-85	150

Table 2.1.: List of studied wildfires and their characteristics. The landcover classes are subdivided in 90: Open needleleaved deciduous or evergreen forest; 110: Mosaic Forest-Shrubland/Grassland; 120: Mosaic Grassland/Forest-Shrubland; 150: sparse vegetation; 200: Bare areas (GLOB Cover 2009 Land Cover Map).

As the study area is subdivided into Taiga and Tundra, their characteristics are explained separately. The Taiga climate (subarctic climate) is milder than tundra climate and moist enough to promote significant vegetation growth, but too cold for rich tree extension. It is characterized by sharply seasonal patterns with extremely cold and long winters, whereas summers are moderately hot and short. In the selected study area, the average temperatures in January are $\sim -40^{\circ}\text{C}$ and $\sim 15^{\circ}\text{C}$ in July. Temperatures being above average in Siberia, even a temperature of 38°C was recorded in Verkhoyansk on 20 June 2020 (WMO). Calculated linear trends for the period of 1966 to 2016 range from 0.4 to $0.5^{\circ}\text{C}/10$ years (Gorokhov and Fedorov, 2018). The precipitation is relatively low, ranging from 150 – 200 mm/year in the lowlands and 400 - 500 mm/year in the mountains. The precipitation tends to increase by 0 to 4 mm/10 years for the southern most parts and decrease the more north by -4 to 0 mm/10 years from 1966-2016 (Gorokhov and Fedorov, 2018). The Taiga vegetation consists of coniferous forests with dominant trees such as larch and silver birch, while Siberian dwarf and lichen are common on the ground.

The Tundra is known for its cold and desert-like conditions, receiving low amounts of precipitation ranging from 150 to 250 mm/year (melting snow included). Here, the precipitation shows even higher negative trends by -8 to -4 mm/ 10years (Gorokhov and Fedorov, 2018). Due to the influence of both continental and ocean processes, the climate of the area is defined as a humid continental climate – cool summer subtype (Koppen classification Dfc). Winters are very long, dark and cold with mean temperatures below 0°C for six to 10 months. The average winter temperatures are ~ -32 to -40°C . Therefore, summers are short and cool with mean temperatures $\sim +4$ to $+12^{\circ}\text{C}$, enabling the ecological zone to sustain. Here, the trend is the same as for the Taiga with 0.4 to $0.5^{\circ}\text{C}/10$ years (Gorokhov and Fedorov, 2018). Therefore, the growing season with ground permafrost thawing allows plants to grow and reproduce during a very short period of 50 to 60 days. The Tundra is also very windy, with winds blowing between 30 to 60 miles per hour. As the water cannot drain through the permafrost during summer, the Tundra is characterized by small lakes and marshes. Dominant vegetation contains dwarf shrubs, grasses, mosses, sedges, and lichens, while few isolated strands of larch taiga grow in the southern Tundra.

Continuous permafrost in the Yana River valley shows a mean annual ground temperature between

2. Study area and data acquisition

-5.5 °C to -8.0 °C at the bottom of the active layer. The ALT varies for forest/moss covered sites between 20 – 40 cm and for open sites between 40 – 120 cm, respectively (Murton et al., 2017).

2.2. Data

2.2.1. Landsat imagery

The entire Landsat image archive (Thematic Mapper (TM), Enhanced Thematic Mapper+ (ETM+) and Observing Land Imager (OLI) sensors) has been included in this study, using both Landsat Top-of-Atmosphere (TOA) reflectance, as well as surface reflectance (SR) data at a map projection WGS84 UTM 53N. The accessibility of steady data for over three decades permits long-term analysis. For the study area, reliable Landsat data was available since 2006, leading to a full time series span of 14 years. Another advantage is given by its spatial resolution of 30 m and largely similar spectral characteristics, compared to other Sensors like MODIS with only 250 m resolution. Therefore, the repetition rate of MODIS/ Sentinel (daily/8-days) is much higher than it is for Landsat (16-days). Many approaches, capturing hemispheric scale pattern at coarser spatial resolution for change detection have been tested (Beck and Goetz, 2011; Goetz et al., 2010; Stow et al., 2004). Landsat provides LST estimates at a high spatial resolution, which is of advantage to cover local and small-scale areas. Capturing rather small-scales would reduce the uncertainty, as small-scale processes would not remain unnoticed. Due to the selection criteria, the fire areas analyzed in this study are rather small in extent, which reinforced the selection of Landsat data. A precise description of the fire areas is necessary to improve the analysis.

For the analysis, only the common bands (blue, green, red, near-infrared / NIR, short-wave-infrared-1 and -2 / SWIR1 and SWIR2) were used. The entire image collection was filtered to acquisition dates of the Arctic summer months (June 1st – August 30th) in order to minimize variations caused by phenology and to enhance the comparability to other Landsat based trend analysis due to the same acquisition dates (Fraser et al., 2014). Additionally, the summer months exhibit less cloud coverage than other seasons, resulting in a more complete consistent data basis. To minimize the domination of confounding elements (such as clouds, shadows), the maximum cloud coverage was set to 80 %. Overall, for all fires, 120 TM, 729 ETM+ and 490 OLI images (1339 altogether) fulfilled the above-listed criteria for a data range from 02-06-2006 to 31-08-2021. Data availability over time shows spatio-temporal variation and is generally inconsistent (Figure 2.2). The amount of image tiles over time including the entire study area varies between a minimum of 36 images in 2006 and steadily increases over time, leading to a maximum of 140 images in 2018, due to the launch of OLI in 2013 and its overlap with ETM+. Likewise, the spatial distribution shows an inhomogeneous pattern, exhibiting 246 images for the most northern fire, ~ 465 images for the most southern fire, and ~ 377 images for the area in between. Due to the high latitude, large overlapping areas of image acquisition paths occur, resulting in a higher frequency (Figure 2.2). As can be seen in Figure 2.2, considerable image overlapping can be found for most of the fire regions. Nevertheless, the potential high acquisition frequency is reduced by cloudiness, short snow-free season, remoteness from receiving stations, and the deficiency of archived TM data (Goward et al., 2006).

Landsat data were accessed and pre-processed via the cloud-based Google Earth Engine (GEE)

2. Study area and data acquisition

platform. The GEE provides a complete list of freely available remote sensing products and can quickly process the requested products online through parallelization, enabling effective, time-saving large-scale geo-spatial studies.

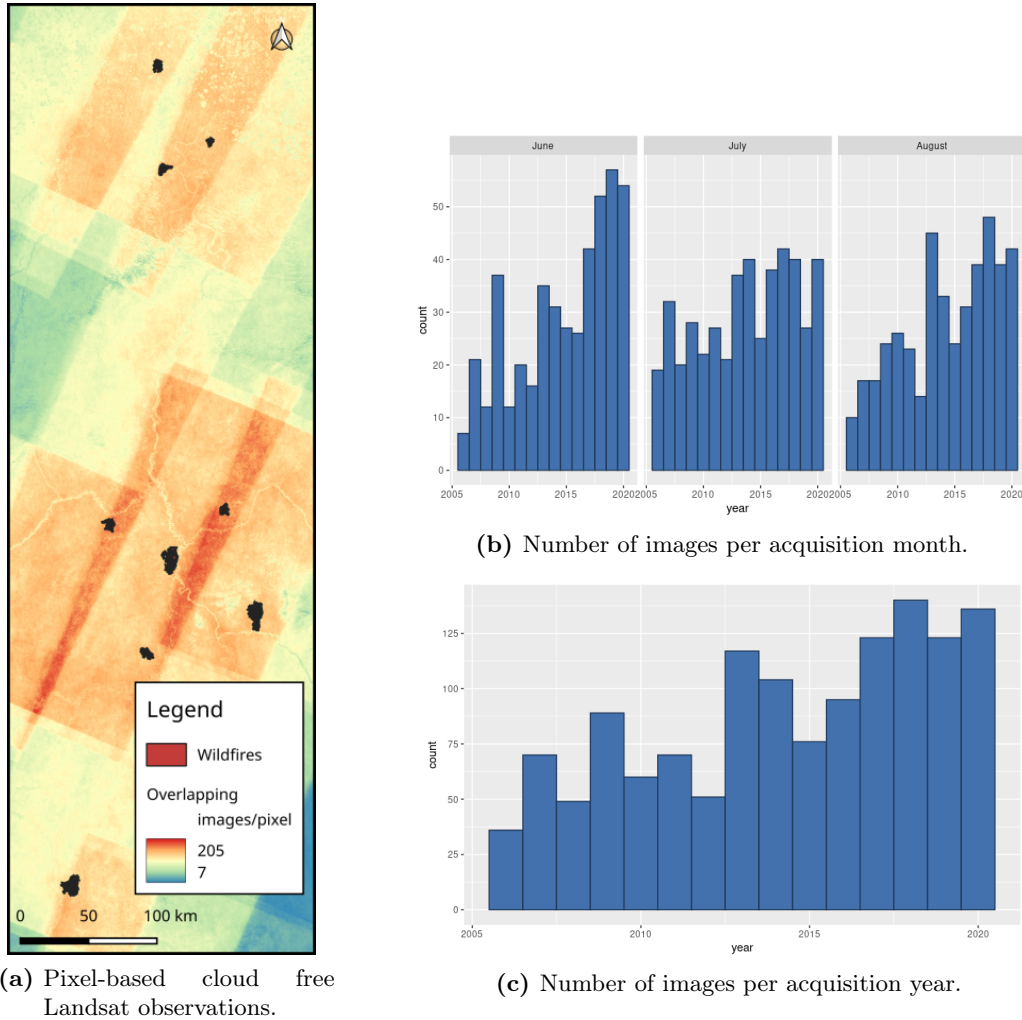


Figure 2.2.: Overview of available Landsat images for the entire study site over the time period from 2006 to 2020.

2.2.2. Auxiliary data

The following non-permafrost related products were not used for statistical analysis but shall give a first impression providing background knowledge concerning the study site.

As the fire impact and regeneration is influenced by factors like elevation and land cover type, classification of the initial state of the fire area before the fire is required. Therefore, the Digital Elevation Model (DEM) obtained from the Shuttle Radar Topography Mission (SRTM) at a resolution of 30 m was added to the data set, which is available from the GEE archive. To describe land cover types, the GlobCover 2009 (Global Land Cover Map) was used. It is produced by an automated classification of MERIS FR time series in 300 m resolution. Additionally, the Hansen-Tree canopy cover for the year 2000 (treecover2000) Landsat-based product was employed, to describe the occurrence of forests at a smaller 30 m scale. To verify the performance of the later used LandTrendr (LT)

2. Study area and data acquisition

algorithm for detecting fire disturbances, the FireCCI51: MODIS Fire_cci Burned Area Pixel product (version 5.1) from the GEE was consulted. It provides monthly global ~ 250 m spatial resolution data, containing information on the burn date in Julian days. Unfortunately, in situ data observation on permafrost conditions are extremely rare in general. Hence, data from the ESA Permafrost Climate Change Initiative (Permafrost_CCI) of the CEDA archive were employed. These data sets were derived from thermal models constrained by satellite data. The initiative offers ALT and ground temperature products, covering the mean for the entire Julian years from the period 1997–2018 at a spatial resolution of 926 km. The satellite data was given by downscaled ERA5 reanalysis near-surface air temperature data (1997-2002) and MODIS land surface temperature (2003-2018). The ground temperature is provided for various depths, including the GST, 1 m, 2 m, 5 m, and 10 m. As most prominent impacts occur on the upper soil layers, only the GST data set has been considered for further analysis.

3. Method

The processing chain (Figure 3.1) applied in this study includes four main steps: 1.) pre-processing of Landsat imagery, 2.) multispectral index calculation, 3.) fire area detection together with LST calculation, and 4.) statistical analysis.

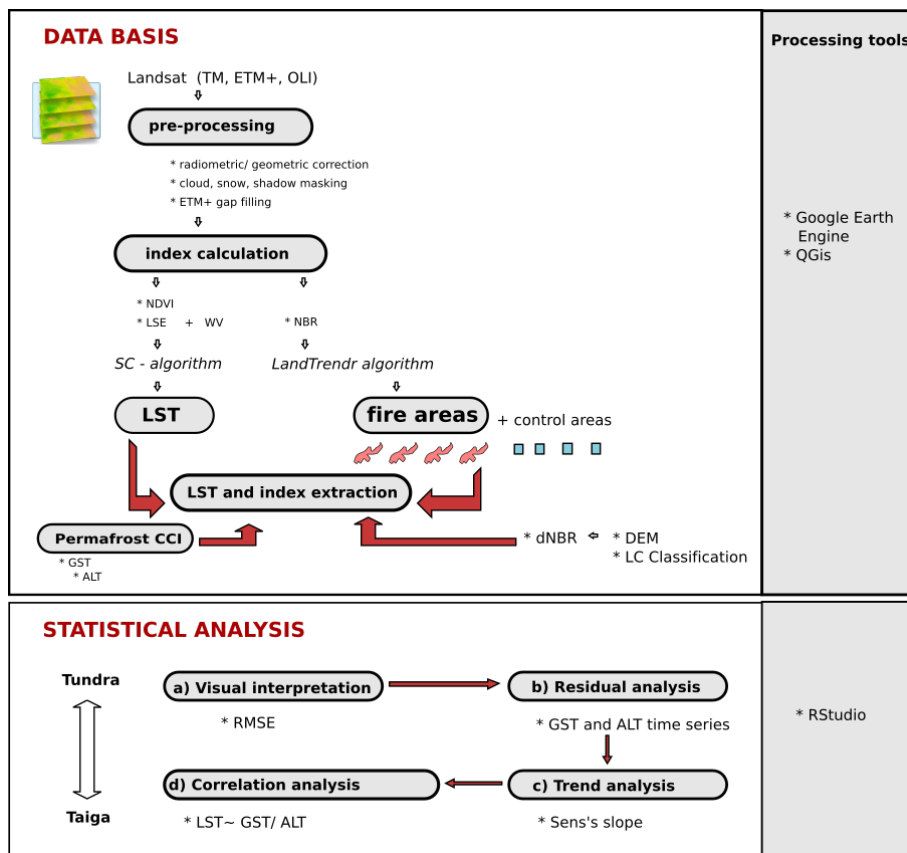


Figure 3.1.: Processing chain divided into data basis, including pre-processing, index calculation, as well as fire area detection and LST calculation, together with the statistical analysis as second part.

3.1. Pre-processing

Pre-processing includes data acquisition via GEE for the filter set by acquisition period, acquisition months, and cloud coverage. Imagery is given as raw digital numbers (DN), incorporating the scaled radiance, surface reflectance (SR) and calibrated Top-of-Atmosphere (TOA) reflectance. The DN rasters needed to be calibrated radiometrically, as the values are influenced by the radiance, reflectance, and atmospheric conditions. This is achieved by using the `ee.Algorithms.Landsat.calibratedRadiance(img)` algorithm in GEE. Firstly, spectral radiance was derived from DNs and based on the result, reflectance

3. Method

(both at sensor) was calculated. Afterward atmospheric correction was performed, whereby atmospheric effects due to absorption and scattering were removed. Using the Quality Assessment Band of the SR product, which was generated from the CFMASK algorithm, all Landsat images were masked for clouds, cloud shadows, and snow/ice.

3.2. Multispectral index calculation

The Normalized Difference Vegetation Index (NDVI) is a crucial parameter for the subsequent LST calculation. It was obtained by the SR product, using the reflectance of near-infrared (NIR; 0.76–0.90 μm) and the red spectrum (RED; 0.64–0.67 μm) and was calculated as follows:

$$NDVI = \left(\frac{NIR - RED}{NIR + RED} \right) \quad (3.1)$$

The NDVI ranges between -1 and 1. The closer the values are to 1, the more vegetation is present. Therefore, the values 0 and 0.1 - 0.2 represent water and soil, respectively.

To identify fire areas and to measure burn severity (BS), the Normalized Burn Ratio (NBR) was determined. Since the NBR was mainly developed for BS assessment, some studies argue that the NBR is not reliable in getting information about an early succession ecosystem reaction (Keeley, 2009; Lentile et al., 2007). On the other hand, good performance of NBR regarding long-term vegetation regeneration has been proved, by many other studies (Chen et al., 2011; Epting et al., 2005; Garcia and Caselles, 1991). Some of them even specify the NBR to be one of the most accurate satellite-driven indices to monitor post-fire environments (Cohen et al., 2018). Instead of the red band in the NDVI-formula (Eq 3.1), the short wave infrared band (SWIR, 2.08–2.35 μm), which is sensitive to water content in vegetation and soils (Miller and Thode, 2007) is used. The equation for NBR is:

$$NBR = \left(\frac{NIR - SWIR}{NIR + SWIR} \right) \quad (3.2)$$

Areas devastated by fire show very low reflectance in the NIR and high reflectance in the SWIR portion of the spectrum, leading to high NBR values (maximum possible NBR=1). The opposite can be seen for healthy vegetation. Non-burnt areas are usually associated with NBR-values close to zero. Additionally, the NBR will be used later on to determine whether the changes in LST are related to the fire event or rather other factors, like seasonality. Furthermore, the NBR is necessary to estimate and extract the fire areas.

To detect the level of fire severity, the difference Normalized Burn Ratio (dNBR) has been proven to be a reliable estimator (Epting et al., 2005; Escuin et al., 2008; Veraverbeke et al., 2014) and was produced in this study for each of the fire areas. It is calculated by the difference between the pre-fire and post-fire NBR obtained from images. High dNBR values indicate more severe damage, while areas with low dNBR values indicate less damage or even regrowth. The formula for calculating the dNBR is shown below:

$$dNBR = (NBR_{pre\,fire} - NBR_{post\,fire}) * 1000 \quad (3.3)$$

3. Method

When it comes to comparisons among fires, it is advisable to incorporate an alternative version of the BS ($\text{dNBR}_{\text{offset}}$) which accounts for the potential phenological differences between pre- and post-fire imagery (Miller and Thode, 2007; Parks et al., 2014). The $\text{dNBR}_{\text{offset}}$ states the mean dNBR of unburned pixels 180 m outside the burned perimeter (Key and Benson, 2006). Testing by Parks et al. (2018) has proven the 180 m distance threshold to produce reliable results, quantifying the dNBR differences between unburned pixels in the Arctic environment. It is necessary, that the vegetation in the fire area and 180 m buffer are similar to provide appropriate results, which was considered for each wildfire. Finally, the subtraction of the fire-specific $\text{dNBR}_{\text{offset}}$ from each dNBR raster gives the requested $\text{dNBR}_{\text{offset}}$ (Key and Benson, 2006). With the given dates of each fire, the designed code use imagery from one year before and one year after each fire event. To minimize uncertainties, the knowledge of the exact time is crucial. The output was classified referring to the BS classes and thresholds proposed by Key and Benson (2006) shown in the following table (Table 3.1). As these threshold values were applied to forested landscapes in the north-western US, they have been considered more reliable than other identified thresholds to define the severity classes.

	Severity level	dNBR Range (scaled by 10^3)
	Low Severity	100 to 269
	Moderate-low Severity	270 to 439
	Miderate-high Severity	440 to 659
	High Severity	660 to 1300

Table 3.1.: Burn severity classes by Key and Benson (2006).

Among others, the BS is important to look at, as within each severity class the LST changes respectively. Regarding high severity classes, the LST is the highest with the greatest difference to the control area. The less the severity, the less the LST differences between fire and control area (Vlassova et al., 2014).

3.3. Change detection to extract fire areas

Altogether, 9 fire areas including their corresponding unburned control areas, were selected as a basis for further data extraction and analysis. Several Landsat image time series (LTS) change-detection techniques exist that have been proven to be robust against spectral differences due to phenology and topography (Griffiths et al., 2012). For this study, the Landsat-based detection of Trends in Disturbance and Recovery algorithm (LandTrendr) was selected as a suitable algorithm to detect fire disturbances associated with vegetation loss (Kennedy et al., 2010). LandTrendr (LT) has been ported to the GEE platform, stating a new version LT-GEE, which provides full access to the Landsat archive and increases the computational speed due to parallel processing (Gorelick et al., 2017). The basic idea behind the LT algorithm (Figure 3.2) is to monitor both short-term radical and long-term moderate changes by examining the temporal-spectral trajectory of each pixel from the annual Landsat time series stacks. The input is given by one spectral band or index, coupled with the date. In this study, the NBR index has been used as input. As vegetation indices can reduce the impacts of external factors like atmosphere and topography on the surface reflectance, they have been regarded as more

3. Method

reliable variables compared to individual spectral bands (Zhu et al., 2019). When applying the LT algorithm a set of control parameters needs to be optimized to find the best model for change detection and to ensure high-quality results. The main parameters (Appendix A Table A1) are the removal of noise-induced spikes (outliers), identifying vertices (breakpoints), the fitting of trajectories, and setting the number of segments (Zhu and Woodcock, 2014). The output of the LT algorithm states the year when changes occurred and the accompanied fire area extent (Figure 3.2). The extent of the fire areas, which fulfill the selection criteria named above, are exported for further LST time series extraction.

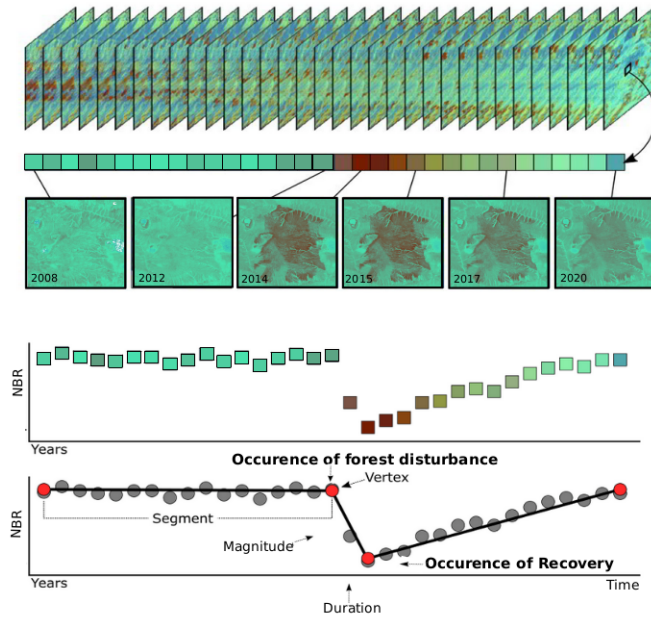


Figure 3.2.: History of Tundra fire (2014) pixels, experiencing a period of relative stability, rapid loss of vegetation due to wildfire, and subsequent regeneration.

To establish the effect of fires on LST, unburned quadratic control areas have been determined. Both areas (fire/control) have the same size and are on the same longitude (east/west position of the adjacent fire area) to reduce uncertainties. The closest distance between fire and control area is 2 km, to make sure, that the transition zone between fire and control area is excluded from the analysis. A greater amount of pixel misclassification shall be prevented. For each fire area, the control areas were chosen individually, whereby homogeneity of land cover and elevation have been considered. Rivers and thermokast lakes close to fire areas were not included. Additionally, control areas exclude fire areas as well as future burned areas to not falsify the results in later time series analysis.

3.4. Retrieval of Land surface temperature

The LST has been calculated using the well established SC-algorithm approach by (Jiménez-Muñoz and Sobrino, 2003). The SC-method can be applied to sensors with just one thermal band such as Landsat TM and ETM+ and is therefore the best choice in terms of comparability between all three sensors involved in this study. Moreover, it is straight-forward in its implementation if all necessary parameters are given (Jiménez-Muñoz and Sobrino, 2003). Nill et al. (2019) applied this algorithm

3. Method

in high latitude environments and considered it to be sufficiently accurate. To implement the SC algorithm, prior knowledge about the LSE and the state of the atmosphere is essential. Based on an approximation of Planck's law, the effective at-satellite calibrated brightness temperature BT_{sen} can be obtained for Landsat infrared data, provided by the SR collection:

$$BT_{sen} = \frac{K_2}{\ln\left(\frac{K_1}{L_{sen}} + 1\right)} \quad (3.4)$$

K_1 and K_2 are band-specific thermal conversion constants given by the metadata. L_{sen} refers to the spectral radiance in $W/(m^2*sr*\mu m)$, which can be obtained by applying the band-specific rescaling factors Gain and Offset also provided with the SR collection metadata file to the pixel values (DN) (Chander et al., 2009).

$$L_{sen} = Gain * DN + Offset \quad (3.5)$$

Regarding Planck's law together with the radiative transfer model, the LST can be retrieved by the following formula (Jiménez-Muñoz and Sobrino, 2003; Jiménez-Muñoz et al., 2008):

$$LST = \gamma \left[\frac{1}{\varepsilon} (\psi_1 L_{sen} + \psi_2) + \psi_3 \right] + \delta \quad (3.6)$$

ε states the surface emissivity, ψ are the atmospheric functions (AFs), γ (Eq 3.7) and δ (Eq 3.8) are parameters based on Planck's law. The latter are defined as follows:

$$\gamma = \frac{BT_{sen}^2}{b\gamma L_{sen}} \quad (3.7)$$

$$\delta = BT_{sen} - \frac{BT_{sen}^2}{b\gamma} \quad (3.8)$$

BT_{sen} is the brightness temperature and b_γ states a sensor-specific constant. It differs from sensor to sensor, respectively. For Landsat TM the value for b_γ is 1256 K, for Landsat ETM+ it is 1277 K and for TIRS it is 1324 K (Jiménez-Muñoz et al., 2008, 2014). The AFs describe downwelling and upwelling radiation, same as transmissivity and represent the atmospherical state. Using a second-degree polynomial fit, they were approximated versus the atmospheric water vapor (WV, Lantz et al. (2010)):

$$\begin{bmatrix} \psi_1 \\ \psi_2 \\ \psi_3 \end{bmatrix} = \begin{bmatrix} c_{11} & c_{12} & c_{13} \\ c_{21} & c_{22} & c_{23} \\ c_{31} & c_{32} & c_{33} \end{bmatrix} \begin{bmatrix} wv^2 \\ wv \\ 1 \end{bmatrix} \quad (3.9)$$

According to literature (Jiménez-Muñoz et al., 2014; Sobrino et al., 2008), the coefficients shown in Appendix A Table A2 are best suited for high latitude environments and were used to fill the matrix (Eq 3.9) in this study. The coefficients c_{ij} were retrieved by Nill et al. (2019) applying simulations by using different atmospheric soundings databases. The outcome shows different coefficients for each sensor with usually low WV content for high latitudes. The reanalyzed atmospheric WV content was retrieved via GEE offered by the National Centers for Environmental Prediction (NCEP) and the National Center for Atmospheric Research (NCAR). The data has been proven to submit accurate

3. Method

results when calculating the LST from Landsat data (Li et al., 2013a; Rosas et al., 2017) and was provided as the total column water vapor at a global scale for every 6 hours (0:00, 6:00, 12:00, 18:00 UTC) at a resolution of 2.5 arc degrees. For the LST calculation, WV values closest to observation time of the Landsat image were chosen instead of taking the mean of all four times. To estimate the LSE for each time step, the Simplified NDVI Threshold Method (SNDVI^{THM}) was used, as both parameters show a linear relationship (Sobrino et al., 2008). To implement this method for deriving pixel emissivity values, certain threshold values for the emissivity and index values for full vegetation cover (ε_v and NDVI_v) and bare soil (ε_s and NDVI_s) need to be chosen. Based on previous studies, the NDVI_s and NDVI_v were chosen to be 0.2 and 0.6, while the emissivity values ε_s and ε_v were set to 0.97 and 0.985 (Li et al., 2013a,b; Sobrino et al., 2004; Wang et al., 2015). Furthermore, the emissivity of NDVI values below zero, representing water bodies, were set to 0.99. The formulas for emissivity are:

$$\varepsilon = \begin{cases} \varepsilon_s & NDVI < NDVI_s \\ \varepsilon_s + (\varepsilon_v - \varepsilon_s)P_v & NDVI_s \leq NDVI \leq NDVI_v \\ \varepsilon_v & NDVI > NDVI_v \end{cases} \quad (3.10)$$

P_v represents the fraction of vegetation cover (Carlson and Ripley, 1997) and is calculated as follows:

$$P_v = \left(\frac{NDVI - NDVI_s}{NDVI_v - NDVI_s} \right)^2 \quad (3.11)$$

Finally, the LST was calculated for each scene, using Equation 3.6. For further time series analysis, the yearly mean LST of all pixels per image was calculated for each fire and control area, as GST and ALT are only available as yearly means. Certain scenes needed to be corrected for remaining outliers after cloud and shadow masking with the CFMask algorithm by setting a threshold of 8 °C (plus pixels with values just above this threshold). Further, the final processing involved mosaicking the multi-temporal layer stacks to get a continuous image surface across the studied areas.

3.5. Statistical analysis

In order to create the base data set for the statistical analysis, the parameters determined in the previous chapter were extracted for each fire area and their corresponding control area. The same was done for the downloaded yearly mean GST and ALT products from the Permafrost_CCI database. The analysis is subdivided into four parts, beginning with the visual interpretation and comparison of LST, NBR, GST, ALT time series and dNBR images, together with the Root Mean Squared Error (RMSE) statistics (such as mean, min, max, standard deviation, and differences between fire and control area). Time series of fire and control areas were plotted for each fire and differencing has been implemented. To show the significance, the pairwise t-test was applied. To show whether the LST differences between fire and control area are rather seasonal related but fire-related, the NBR time series for each fire has been interpreted. Furthermore, the dNBR gives an insight on the fire severity and hence recovery rate of each fire and control area. Afterward same is implemented for the GST and ALT time series, with particular attention to the year the fires occurred. To show if an impact of fire

3. Method

occurs at the year of fire for the GST and ALT time series, the residuals have been computed for each study area. Having regarded the RMSE, the trend analysis defines the next step, regarding trends before and after the fire event for the study areas. Trend analysis has been applied to LST, GST, and ALT. Instead of standard least-squares regression, the Theil-Sen (T-S) regression method (Sen, 1968; Theil, 1992) has been implemented, as it is very robust with insensitivity to around 30% outliers (Fernandes and Leblanc, 2005). Fraser et al. (2014) successfully applied the technique on Landsat time series analysis in the North American Taiga and Tundra regions for forest change detection.

The Sen's slope is the median of paired slope from every point in time to one another and is calculated by the formula below:

$$ts_slope = median \left(\sum_{\substack{j=1 \\ i=1}}^n \frac{(y_i - y_j)}{(t_i - t_j)} \right) \quad (3.12)$$

The intercept is given by:

$$intercept = median(y) - ts_slope * median(t) \quad (3.13)$$

T-S calculations were carried out in RStudio using the `sens.slope()` function. The intercept was also calculated in this study but not further included in the analysis.

Finally, in order to quantify the relationship between LST and GST as well as ALT, correlation analysis was conducted as a final step in the analysis. To calculate the correlation in RStudio, the Spearman's rank correlation (`cor.test(x, y, method = "spearman")`) – a non-parametric test was used as it is very robust as it bases on ranks (Eq. 3.14). The Spearman correlation coefficient r_s describes the relationship between two variables and ranges from -1 to +1, whereby -1 and 1 represent complete correlation and 0 means no correlation. Negative values indicate that with the increase of one variable, the other one decreases. To test the statistical significance, the `cor.test()` function was used. If $p \leq 0.05$, the result is considered significant and the null hypothesis, stating that there is no correlation between both variables, can be rejected. If the p-value is > 0.05 , the null hypothesis will be accepted. Before correlating the LST data with GST and ALT, resampling of the LST data needed to be done beforehand to get more reliable results. The spatial resolution of the permafrost products is 926 m and for LST as already mentioned above is 30 m. Therefore, LST was resampled to 926 m, giving the best correlation results. The Spearman's rank correlation coefficient is calculated as follows:

$$rs = 1 - \frac{6 \sum d_i^2}{n(n^2 - 1)}, \quad (3.14)$$

where n is the number of observations and d_i the difference between ranks of the observations.

4. Results

4.1. Visual interpretation of time series

Four factors influencing permafrost were evaluated: (1) LST, (2) loss of vegetation coverage and recovery rate (NBR, dNBR), (3) GST and (4) ALT.

4.1.1. Yearly mean summer LST

To reveal the post-fire response in temporal LST patterns, the yearly summer mean LST during a 15-yr time period from 2006-2020, was evaluated by visual interpretation. The time series (Figure 4.1 and Appendix B Figure B1) display the yearly area-averaged LST plus standard deviation over the fire and control areas. Regarding the year of fire disturbance for each study site, the time period varies between 3-8 years before the fire and 6-12 years after the fire event. The approximate time when the fire started, is indicated by the gray vertical bar in the figures. Additionally, the difference (dLST) between the fire area and the control is given in the plot below. The entire results part includes visualizations of three selected study areas (fire₁, fire₄ and fire₉), marking a south-north transect. The rest are included in the associated Appendix. Therefore, the statistics are shown for all study areas in the tables below the figures (Table 4.1).

4. Results

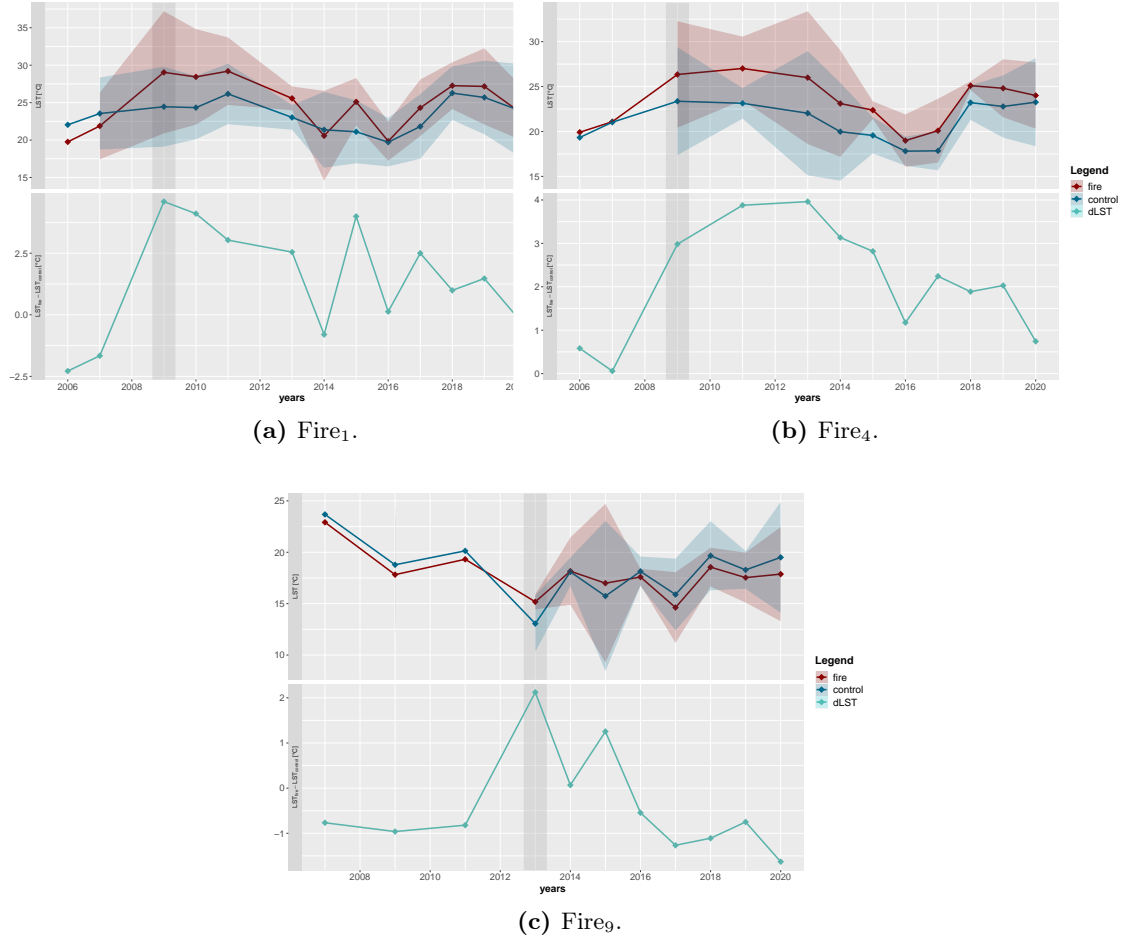


Figure 4.1.: LST time series, together with dLST. The gray bar marks the year of fire disturbance, while the red and blue areas mark the standard deviation for the fire and control area, respectively.

Given the times series (Figure 4.1) and the table (Table 4.1) below, the results show that the mean LST_{fire} is greatest for fire₁ with 25.05°C (min: 19.75°C and max: 29.19°C) and slightly decreases with increasing latitude to a minimum of 17.50°C (min: 14.62°C and max: 22.91°C) for fire₉, including one exception of fire₃ which exhibits lower temperatures with 21.30°C than the fires around. Same pattern becomes apparent for the mean $LST_{control}$ were temperatures also decrease from 23.43°C (min: 19.71°C and max: 26.17°C) for fire₁ to 17.93°C (min: 13.05°C and max: 23.68°C) for fire₉, including the same exception of fire₃ with lower temperatures of 14.96°C. Comparing both, LST_{fire} and $LST_{control}$, the mean of LST_{fire} is higher for the fires_{1–6} and the other way around for fires_{7–9}. A significantly higher LST_{fire} than $LST_{control}$ is given for all fires, except for fires_{5,7} with p-values of 0.13 and 0.20, respectively. The standard deviations partly exhibit values of 8°C, mainly for LST_{fires} and decrease for $LST_{control}$. dLST is low before the fire event, ranging from 0.01°C for fire₁ to -1.82°C for fire₉. After the fire, dLST increases up to a minimum of 0.40°C for fire₈ and up to a maximum of 3.45°C for fire₃. Regarding the southernmost time series, dLST is the highest for 1-5 years after the fire and decreases until the end of time series. Therefore, the northernmost areas exhibit a faster decrease of 1-3 years after the fire.

4. Results

fire	LST _{fire} [°C]			LST _{control} [°C]			p-value	dLST _{before} [°C]	dLST _{after} [°C]
	mean	min	max	mean	min	max			
1	25.05	19.75	29.19	23.43	19.71	26.17	0.04	-1.82	2.05
2	23.80	20.38	28.76	22.50	17.43	26.78	0.05	0.18	2.17
3	21.30	13.69	27.64	19.38	14.96	22.68	0.001	0.65	3.45
4	23.27	18.98	26.34	21.16	17.80	23.36	0.04	-0.79	2.63
5	22.14	17.56	27.59	21.53	16.48	24.85	0.13	0.38	0.78
6	22.39	17.31	26.07	20.69	15.11	24.36	0.0001	0.82	1.86
7	20.46	16.91	24.69	21.00	15.95	25.25	0.208	-0.97	0.47
8	19.71	15.84	26.74	20.02	14.24	26.31	0.028	0.17	0.40
9	17.50	14.62	22.91	17.93	13.05	23.68	0.038	0.01	0.61

Table 4.1.: Summary of LST RMSE statistics, including mean, min and max of the study areas with corresponding p-values and the mean dLST before and after the fire event.

4. Results

4.1.1.1. Yearly mean summer NBR and dNBR

In order to test if the changes in LST are due to fire events rather than other factors, the NBR was calculated for the fires areas. Figure 4.2 and Appendix B Figure B2 show the yearly mean NBR of fire pixels and their corresponding control pixels. The area colored in blue between both areas, marks the recovery rate.

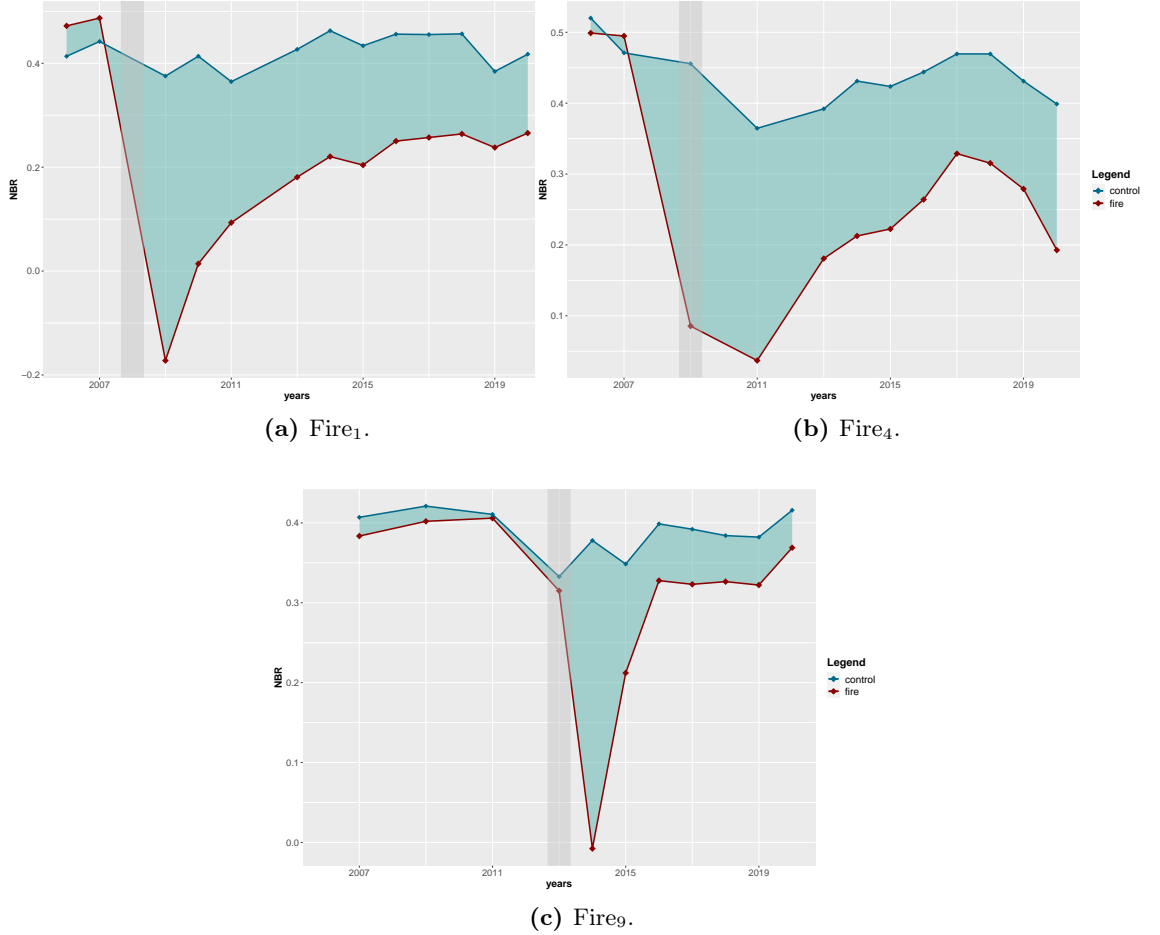


Figure 4.2.: NBR time series of fire areas, with recovery rate colored as the blue area in between.

All plots show an immediate decrease of NBR for the fire area at the year the fire occurred, proving the change in LST to be related to a fire event. But they vary in pattern, regarding the change in latitude. Together with table 4.2, the areas unaffected by fire show mean NBR values between 0.35 (min: -0.16 and max: 0.45) for fire₇ to 0.47 (-0.18 to max: 0.51) for fire₃ with generally higher values in the south than in the north. Therefore, the mean for NBR_{fires} are lower, showing a minimum of 0.18 (min: 0.05 to max: 0.44) for fire₂ and a maximum of 0.31 (min: -0.01 to 0.45) for fire₈. All fires, except fire_{5,6} are significant. Before the fire occurred, the differences ($dNBR = NBR_{fire} - NBR_{control}$) were close to zero with a minimum of $1.67e-05$ for fire₈ and a maximum of -0.05 for fire₆. Therefore, post-fire areas increase negatively with a minimum of -0.11 for fire₇ and a maximum of -0.39 for fire₂. The difference is regarded as the capability to recover, not just as the impact of fire. Even though, all

4. Results

time series experience a clear NBR drop directly after the fire, the recovery rate is remarkably different. Hence, fires₇₋₉ are revealing a faster regeneration after the initial NBR drop, taking 3-4 years of the fire pixels to adjust to the control pixels. In contrast, the fires₁₋₆ show rather intermediate behavior with no to very slow adjustment of fire and control pixels.

fire	NBR _{fire}			NBR _{control}			p-value	dNBR _{before}	dNBR _{after}
	mean	min	max	mean	min	max			
1	0.21	0.01	0.48	0.42	0.36	0.46	4.17e-09	0.04	-0.25
2	0.18	0.05	0.44	0.43	0.30	0.48	3.07e-07	0.03	-0.39
3	0.3	-0.18	0.51	0.47	0.36	0.57	7.45e-05	-0.02	-0.28
4	0.24	0.03	0.49	0.43	0.36	0.52	9.91e-09	-0.01	-0.22
5	0.24	-0.29	0.47	0.44	0.41	0.46	-0.14	-0.02	-0.23
6	0.26	0.03	0.50	0.45	0.39	0.51	-0.15	-0.05	-0.21
7	0.26	-0.16	0.45	0.35	0.33	0.40	-0.04	0.04	-0.11
8	0.31	-0.01	0.45	0.41	0.38	0.45	0.002	1.67e-05	-0.16
9	0.29	-0.01	0.40	0.39	0.33	0.42	0.004	-0.02	-0.12

Table 4.2.: Summary of NBR RMSE statistics, including mean, min and max of the study areas with corresponding p-values and the mean difference (dNBR) before and after the fire event.

After proving that the changes in LST are related to wildfires, the NBR shall be further used to calculate the spatio-temporal BS for each wildfire (Figure 4.3). The images are mapped in yellow-purple color scale. The low dNBR values are represented in yellow, moderate-low in orange, moderate-high in red and high severity pixels are marked in purple. The spatial pattern of BS is clearly visible, showing a clear distinction between low and high severity patches. The figure shows that the BS decreases from south to north. The first three southern most fires show great patches with high severity, while the next three fires show just a few patches and regarding the last three fires, high severity pattern are barely visible. On one hand, the images shall illustrate the BS but on the other hand, they shall give a general impression of the fire appearances.

4. Results

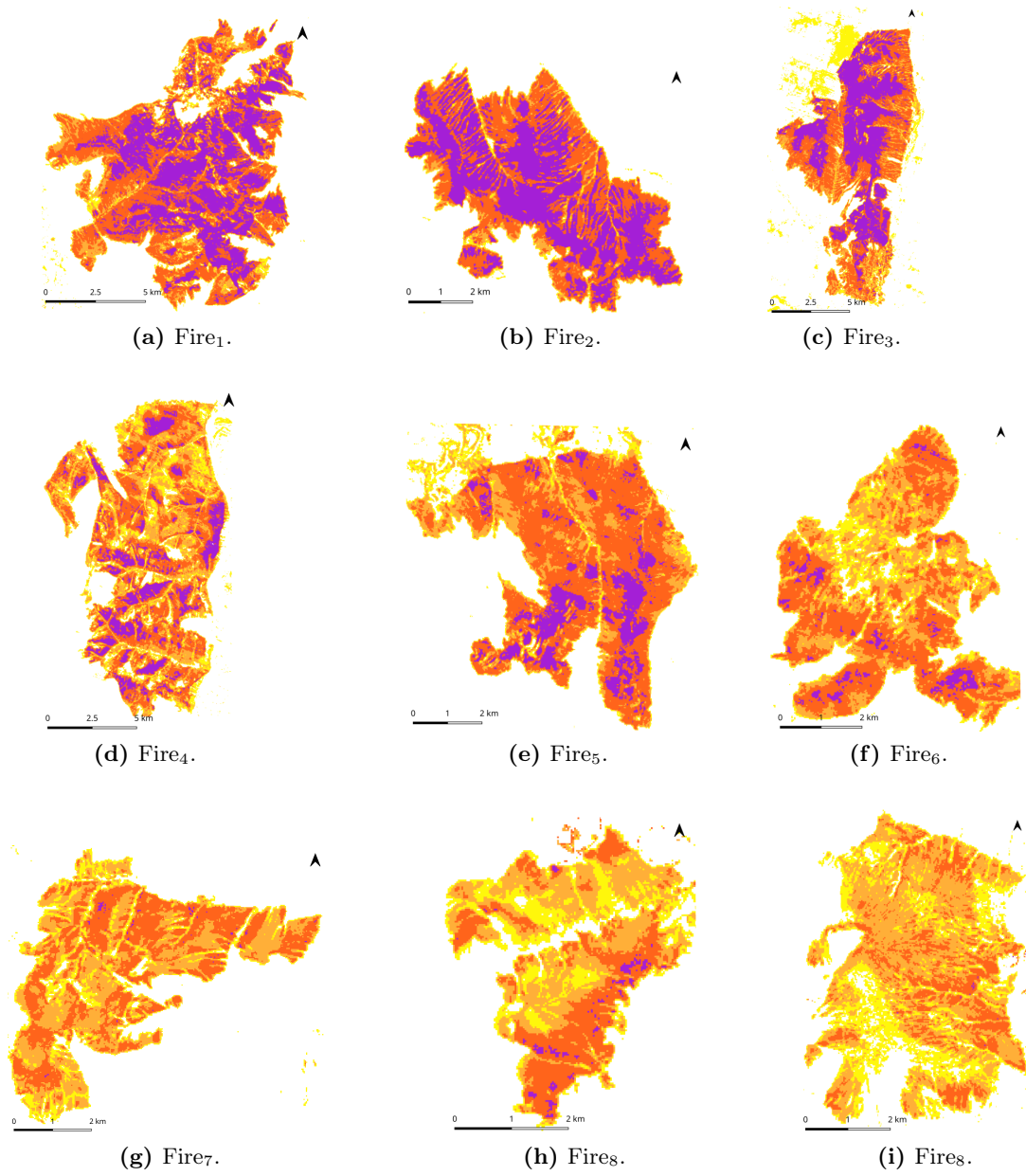


Figure 4.3.: Spatio-temporal BS for each wildfire.

4. Results

4.1.2. Yearly mean GST

Figure 4.4 and the Appendix B Figure B3 display the yearly mean GST time series for the time period 1997-2018.

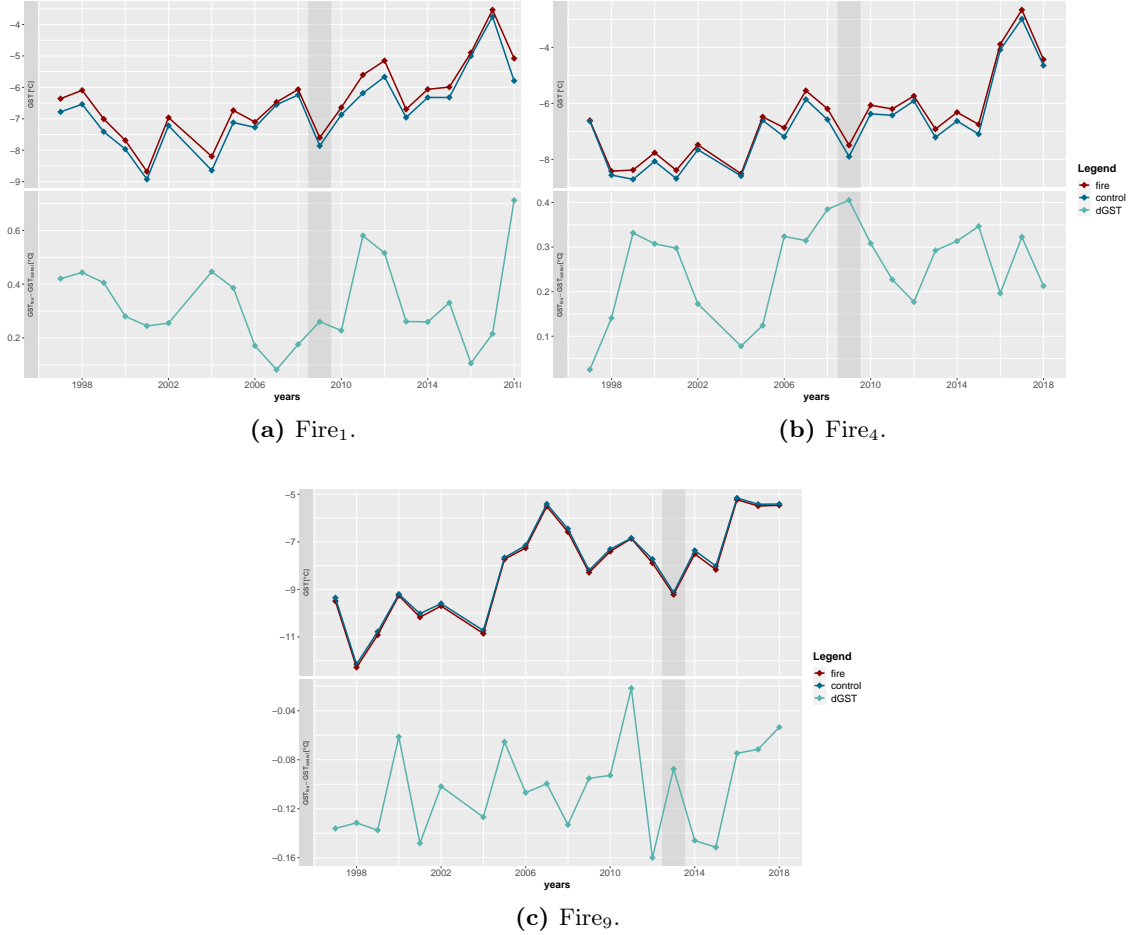


Figure 4.4.: GST time series, together with dGST. The gray bar marks the year of fire disturbance.

The $GST_{control}$ show mean values between -5.56°C (min: -1.74°C and max: -8°C) for fire₆ to -8.14°C (min: -4.47°C and max: -11.95°C) for fire₈, with generally cooler temperatures in the north than in the south (Table 4.3). Exceptions are formed by fires_{3,6} with warmer temperatures of -5.73°C and -5.56°C . Compared to the mean GST_{fire} , the minimum is given by fire₃ with -5.80°C (min: -2.74°C and max: -7.88°C) and the maximum with -8.16°C (min: -5.22°C and max: -12.28°C) for fire₉. Regarding dGST before and after the fire, all fires, except fire₇ with a decrease in temperature from -0.27°C to -0.20°C , show an increase in temperature. Fire₅ (0.09°C to 0.08°C) and fire₉ (-0.11°C to -0.1°C) stay almost the same. Fire₂ shows a strong increase from -0.1°C to 0.35°C , but with no significance showing a p-value of 0.22. The other fires show a significant increase in temperature. Generally, the differences are greater in the south with 0.35°C for fires_{1,2} than in the north with -0.1°C for fire₁, with a few exceptions for fires_{3,5,6}. Conspicuous are the negative differences for fires_{3,6,7,9}, meaning that temperatures for $GST_{control}$ are crossing the temperatures of GST_{fire} .

4. Results

fire	GST _{fire} [°C]			GST _{control} [°C]			p-value	dGST _{before} [°C]	dGST _{after} [°C]
	mean	min	max	mean	min	max			
1	-6.41	-3.53	-8.68	-6.73	-3.75	-8.92	9.639e-09	0.30	0.35
2	-6.41	-3.53	-8.68	-6.25	-2.97	-8.13	0.2223	-0.10	0.35
3	-5.80	-2.74	-7.88	-5.73	-2.65	-7.84	8.746e-05	-0.07	-0.09
4	-6.53	-2.66	-8.51	-6.78	-8.71	-2.98	4.294e-10	0.23	0.28
5	-6.71	-3.00	-8.92	-6.80	-2.98	-9.00	3.468e-07	0.09	0.08
6	-6.15	-2.55	-8.42	-5.56	-1.74	-8.00	6.942e-14	-0.55	-0.63
7	-7.35	-4.15	-10.95	-7.11	-3.97	-10.54	1.807e-08	-0.27	-0.20
8	-8.03	-4.26	-11.97	-8.14	-4.47	-11.95	7.185e-06	0.10	0.13
9	-8.16	-5.22	-12.28	-8.05	-5.15	-12.14	4.682e-11	-0.11	-0.10

Table 4.3.: Summary of GST RMSE statistics, including mean, min and max of the study areas with corresponding p-values and the mean difference (dGST) before and after the fire event.

4. Results

4.1.2.1. Residual analysis of GST

To prove whether the increasing trend is related to the fire event, residuals were calculated for the fire and control area shown graphically (Figure 4.5 and Appendix B Figure B. 4), as well as in table (Appendix B Table B1). In most cases, the residuals show higher values for GST_{fire} than for $GST_{control}$ at the year of fire disturbance. $Fire_2$ shows no crossing of the control residuals by the fire residuals at or after the fire event. For the $fires_{3,4}$, a crossing is visible one year after the fire occurred. Conspicuous is the decrease of consecutive years with fire residuals greater than control residuals after the fire occurred. For the first fire, the residuals are higher for GST_{fire} until five years after the fire. Subsequent, $fires_{3,4}$ show higher residuals for three years and are getting less until one to two years for the last three fires in the north. The residuals will only be used to determine the relation of GST to the fire event and will not be further analyzed.

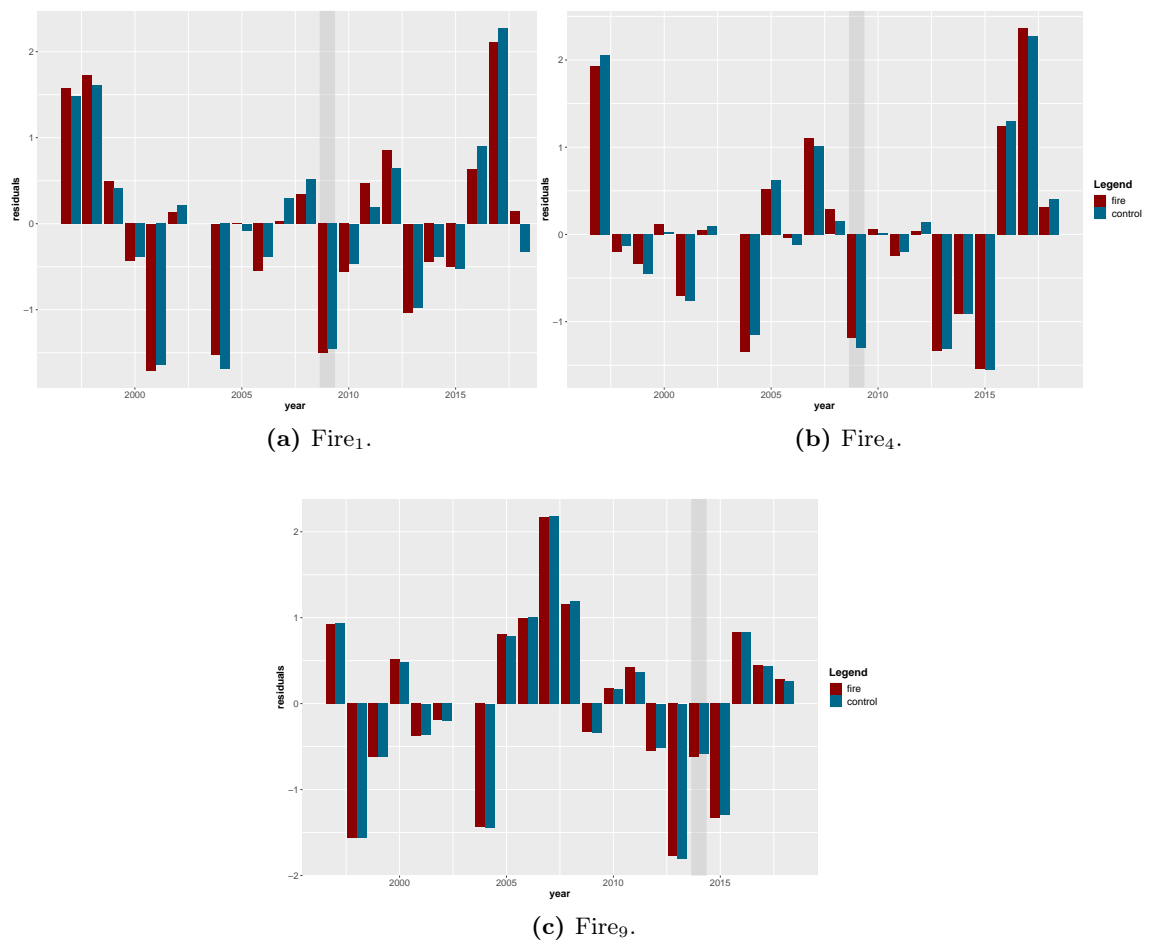


Figure 4.5.: GST residuals over the time period from 1997-2018.

4. Results

4.1.3. Yearly mean ALT

The following Figure 4.6 and the Appendix B: Figure B5 show the yearly mean ALT from 1997-2018.

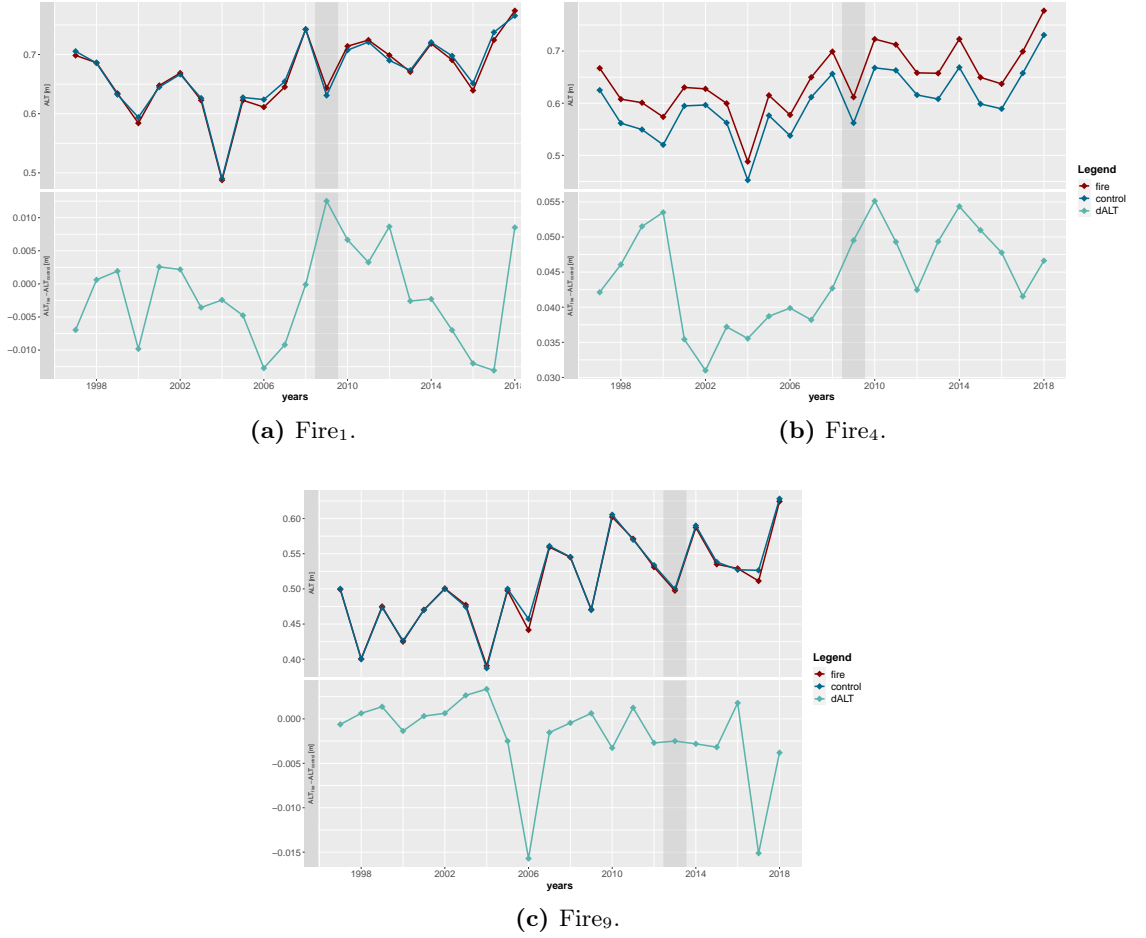


Figure 4.6.: ALT time series, together with dALT. The gray bar marks the year of fire disturbance.

Regarding the time series together with table 4.4, the $ALT_{control}$ show mean values between 0.51m (min: 0.38m and max: 0.63m) for fire₉ and 0.73m (min 0.58m and 0.84m) for fire₂. For ALT_{fire} , the minimum ALT is 0.51m (min: 0.39m and max: 0.62m) for fire₉ and the maximum is 0.72m (min: 0.55m and max: 0.84m) for fire₂. The mean ALT thins within increasing latitude for both fire and control areas with exceptions for fires_{2,5} for ALT_{fire} and fires_{2,4} for $ALT_{control}$. Comparing both, the means are greater for ALT_{fire} for fires_{4,5,7}, smaller than control area for the fires_{2,6} and equal for most of the fires_{1,3,8,9}. The fires_{1,3,8,9} do not show a significance. In most cases (fires_{1,3,8,9}), low changes occur with dALT between 0.0002m (fire₃) and 0.005 (fire₈), showing also no significance. A maximum dALT is shown for fire₄ with 0.05m. A significance is given for fires_{2,5,6,8}. No distinct south-north trend is apparent.

4. Results

fire	ALT _{fire} [m]			ALT _{control} [m]			p-value	dALT _{before} [m]	dALT _{after} [m]
	mean	min	max	mean	min	max			
1	0.67	0.48	0.77	0.67	0.49	0.77	0.2589	-0.003	0.0003
2	0.72	0.55	0.84	0.73	0.58	0.84	8.167e-08	-0.01	-0.005
3	0.65	0.51	0.78	0.65	0.51	0.77	0.9181	-0.0001	0.0002
4	0.64	0.49	0.78	0.60	0.45	0.73	2.2e-16	0.04	0.05
5	0.65	0.49	0.77	0.63	0.48	0.76	1.271e-10	0.01	0.02
6	0.61	0.47	0.74	0.63	0.48	0.78	8.322e-10	-0.015	-0.024
7	0.52	0.37	0.66	0.51	0.36	0.65	2.63e-08	0.011	0.012
8	0.51	0.38	0.64	0.51	0.36	0.65	0.8029	-0.0004	0.005
9	0.51	0.39	0.62	0.51	0.38	0.63	0.07035	-0.001	-0.005

Table 4.4.: Summary of ALT RMSE statistics, including mean, min and max of the study areas with corresponding p-values and the mean difference (dALT) before and after the fire event.

4. Results

4.1.3.1. Residual analysis of ALT

In the following Figure (Figure 4.7 and Appendix B: Figure B7 and Appendix B Table B2), the residuals are used to show whether the changes in ALT are due to a fire event or other factors. Fires_{2,3} show greater residuals with 0.82 and 0.86 for ALT_{fire} and 0.94 and 0.92 for ALT_{control}, respectively. Besides, all the other fires show greater values for fire areas than control areas at the year of fire (fire_{8,9}) or the year after (fire_{1,4,5,6,7}). Same as for GST, crossings of fire residuals with control residuals last longer in time after the fire until 4 years after the fire and gets less within the more north it gets until 1 year.

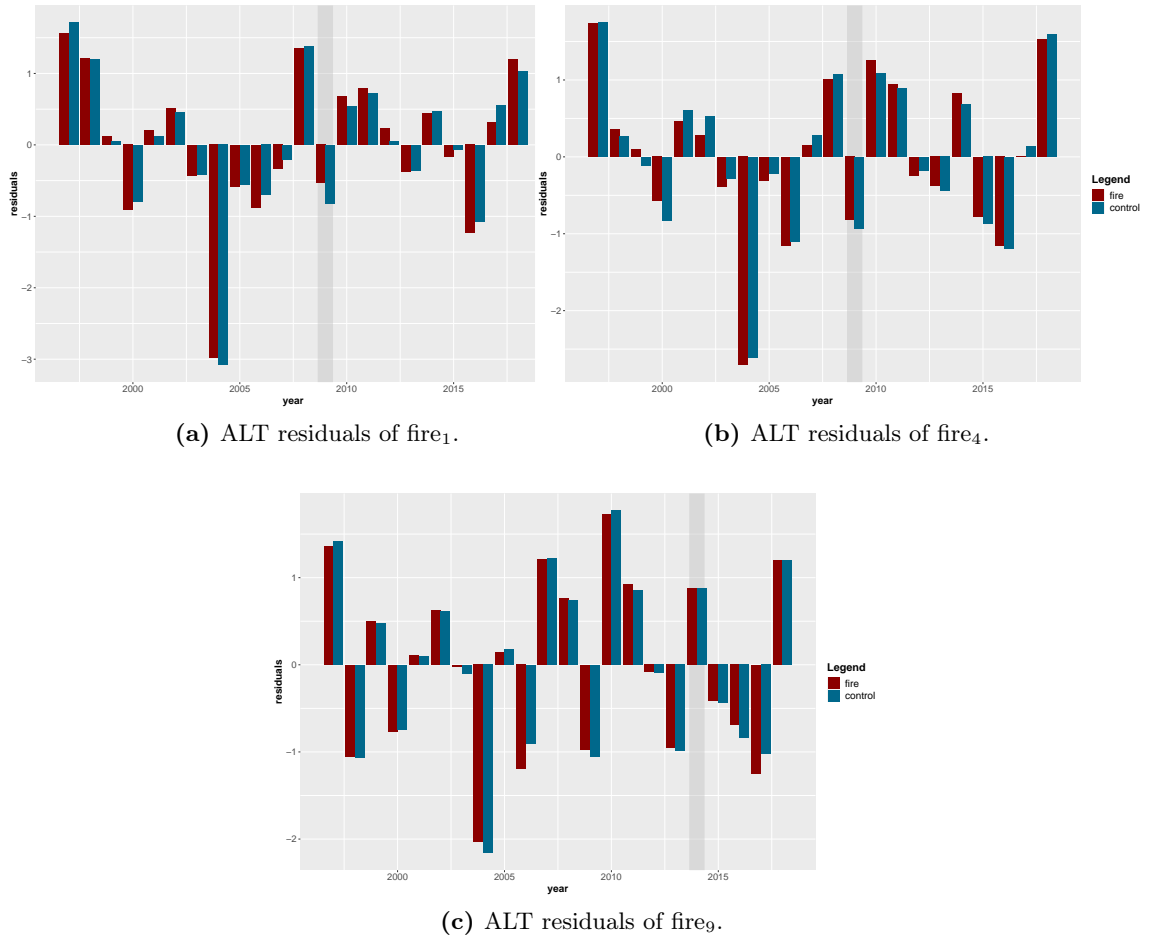


Figure 4.7.: ALT residuals over the time period from 1997-2018.

4.2. Trend analysis

4.2.1. Yearly summer mean LST

The following table (Table 4.5) displays the Sen's slopes t_s before and after the fire event, discriminating between fire and control areas, as well as before and after the fire. Comparing the Sen's slopes after the fire event of both, same patterns are visible, excluding fire₇. fire_{after} show a negative slope with $t_s = -0.13$, while a positive slope with $t_s = 0.09$ was calculated for the control_{after}. Apart from that, fires_{1,3,4} show negative trends in regard to the slopes of fire_{before}. Fires_{2,5,6,8,9} are showing an increase

4. Results

in temperature after the fire. The minimal Sen's slope occurs for fires_{8,9} with $ts = -0.07$ and $ts = 0.07$ respectively. The maximum increase with $ts = 1.02$ is visible for fire₃. Generally, the Sen's slopes show a greater increase after the fire for fires in the south than in the north.

fire	fire _{before}			fire _{after}			control _{before}			control _{after}		
	<i>ts</i>	<i>p</i>	<i>i</i>	<i>ts</i>	<i>p</i>	<i>i</i>	<i>ts</i>	<i>p</i>	<i>i</i>	<i>ts</i>	<i>p</i>	<i>i</i>
1	2.12	1	17.63	-0.31	0.12	27.37	1.50	1	20.53	-0.07	0.75	24.45
2	-0.07	1	25.23	0.66	0.22	21.20	-0.1	1	26.03	0.91	0.22	19.32
3	1.20	0.26	25.23	1.03	0.23	18.08	1.10	0.23	26.03	1.06	0.55	13.67
4	1.18	1	18.73	-0.31	0.15	27.021	1.70	1	17.63	-0.05	0.72	22.76
5	-2.578	1	22.70	-0.30	0.53	25.64	-3.85	1	24.18	-0.22	0.76	23.36
6	2.99	1	15.42	0.27	0.53	21.57	2.03	1	16.26	0.31	0.35	18.72
7	0.25	1	21.80	-0.13	0.59	21.91	-2.73	1	27.99	0.09	0.59	21.34
8	-4.05	0.08	28.32	-0.07	0.54	21.03	-4.01	0.08	28.33	-0.04	1	21.12
9	-2.19	0.31	23.42	0.07	1	17.38	-3.20	0.31	24.77	0.34	0.13	17.11

Table 4.5.: LST Sen's slopes before and after the fire event for the fire and control areas, together with p-value and intercept.

4.2.2. Yearly mean GST

Same trend analysis (Table 4.6) as for LST was done for GST, showing positive slopes for all fires in the control area with a minimum of $ts = 0.25$ for fire₁ and a maximum of $ts = 0.75$ for fire₃. All of them show a significant increase, except fire₅. Same holds true for the comparison of the slopes before and after the fire at the control area, resulting in increasing slopes, except for fire₁. A clear south-north pattern as for LST Sen's slopes is not apparent. Regarding the fire area, slopes increase after the fire for fires_{2,3,4,6,7,8,9}, meaning a decrease in temperature. Therefore, a cooling occurs for fire_{1,5}. The minimum slope is $ts = 0.30$ for the fire₁ and maximum $ts = 0.81$ for fire₂. Generally, the steepest slopes occur for the fire₂ ($ts = 0.82$) and fire₃ ($ts = 0.74$), as well as fire₈ ($ts = 0.75$) and fire₉ ($ts = 0.59$). Additionally, they are steeper for the fire area than control.

fire	fire _{before}			fire _{after}			control _{before}			control _{after}		
	<i>ts</i>	<i>p</i>	<i>i</i>	<i>ts</i>	<i>p</i>	<i>i</i>	<i>ts</i>	<i>p</i>	<i>i</i>	<i>ts</i>	<i>p</i>	<i>i</i>
1	0.52	0.001	-7.62	0.30	9.237e-08	-7.61	0.52	0.001	-7.79	0.26	7.653e-08	-7.62
2	-0.005	6.482e-06	-5.92	0.82	9.97e-05	-6.51	-0.01	6.745e-06	-5.87	0.62	8.556e-05	-6.39
3	0.03	1.186e-05	-5.89	0.74	6.296e-05	-6.29	0.02	1.399e-05	-5.79	0.76	5.416e-05	-6.28
4	0.34	0.004	-7.21	0.36	5.813e-08	-7.57	0.31	0.004	-7.50	0.38	4.506e-08	-7.92
5	0.35	0.003	-7.38	0.33	5.843e-08	-7.63	0.34	0.003	-7.48	0.53	0.34	-8.93
6	0.20	0.006	-6.06	0.38	6.769e-08	-7.41	0.20	8.841e-08	-5.49	0.40	0.006	-6.87
7	-0.83	0.004	-4.20	0.32	2.295e-07	-7.65	-0.78	0.004	-4.14	0.28	3.143e-07	-7.16
8	-0.29	1.722e-05	-5.78	0.75	4.273e-05	-8.21	-0.26	1.487e-05	-6.10	0.72	4.485e-05	-8.22
9	-0.33	1.925e-05	-5.66	0.59	2.914e-05	-8.10	-0.33	2.048e-05	-5.54	0.57	3.127e-05	-7.93

Table 4.6.: GST Sen's slopes before and after the fire event for the fire and control areas, together with p-value and intercept.

4. Results

4.2.3. Yearly mean ALT

Comparing the Sen's slopes (Table 4.7) for the fire area after the fire at the control and fire area show the same pattern, resulting in an decrease in thickness for all fires, except fire_{2,3}. The minimum for the control area is $ts = -0.001$ for fire₈ and the maximum $ts = 0.023$ for fire₃. The minimum for the fire area is $ts = -0.003$ for fire₇ and the maximum with $ts = 0.025$ for fire₂. For both, the last three fires display negative slopes, while the others are positive but compared to the condition before, they shrink. After the fire, for the fire area a significant decrease in ALT is visible for all fires, except fire_{8,9} with $p = 0.18$ and $p = 0.38$ respectively.

fire	fire _{before}			fire _{after}			control _{before}			control _{after}		
	<i>ts</i>	<i>p</i>	<i>i</i>	<i>ts</i>	<i>p</i>	<i>i</i>	<i>ts</i>	<i>p</i>	<i>i</i>	<i>ts</i>	<i>p</i>	<i>i</i>
1	0.065	0.132	0.545	0.007	0.001	0.668	0.059	0.135	0.564	0.007	0.001	0.666
2	0.005	0.003	0.691	0.025	0.029	0.700	0.003	0.003	0.717	0.020	0.033	0.719
3	0.006	0.003	0.639	0.024	0.030	0.618	0.006	0.003	0.637	0.023	0.023	0.623
4	0.061	0.129	0.516	0.004	0.001	0.655	0.059	0.124	0.479	0.004	0.001	0.612
5	0.057	0.131	0.531	0.005	0.001	0.650	0.058	0.129	0.515	0.005	0.001	0.635
6	0.060	0.125	0.488	0.005	0.001	0.612	0.063	0.127	0.498	0.009	0.001	0.618
7	0.007	0.054	0.507	-0.003	0.001	0.566	0.008	0.053	0.488	-0.003	0.001	0.553
8	0.007	0.002	0.507	-0.013	0.182	0.701	0.006	0.003	0.521	-0.001	0.026	0.541
9	-0.001	0.378	0.551	-0.022	0.385	0.609	0.003	0.003	0.523	-0.003	0.026	0.545

Table 4.7.: ALT Sen's slopes before and after the fire event for the fire and control areas, together with p-value and intercept.

4.3. Correlation analysis

Before correlating the LST data with GST and ALT, resampling of the LST data is needed to get more reliable results. The spatial resolution of the permafrost products is 926 m and for LST as already mentioned is 30 m. Therefore, LST was resampled to 926 m, giving the best correlation results. Calculations have been made only for the fire areas, regarding the yearly means of LST, GST and ALT (Table 4.8).

fire		GST		ALT	
		<i>rs</i>	<i>p</i>	<i>rs</i>	<i>p</i>
1	LST	-0.08	0.8	0.49	0.12
2	LST	-0.46	0.15	-0.09	0.80
3	LST	0.24	0.48	0.15	0.66
4	LST	-0.45	0.48	0.20	0.54
5	LST	-0.35	0.30	0.43	0.19
6	LST	-0.25	0.45	0.24	0.49
7	LST	-0.28	0.42	0.61	0.06
8	LST	0.02	0.98	0.22	0.58
9	LST	0.38	0.31	0.63	0.07

Table 4.8.: Correlation results of yearly mean LST with GST and ALT.

4. Results

Regarding the correlation between LST~GST, the spearman correlation coefficient r_s is the highest for the fire₂ with $r_s = -0.46$, fire₄ with $r_s = -0.45$ and fire_{5,9} with $r_s = -0.35$ and 0.38 , respectively. The lowest correlation occurs for fire₁ with $r_s = -0.08$ and fire₈ with $r_s = 0.017$. All in all, negative moderate correlations occur for the fires₁₋₇ with one exception of fire₃ and positive moderate correlations for fire_{8,9}.

Looking at the correlation between LST~ALT, the highest correlation coefficient occurs again for fire₉ with $r_s = 0.63$ and fire₇ with $r_s = 0.61$. Fires_{1,5} are also showing a quite moderate correlation with $r_s = 0.49$ and $r_s = 0.43$ respectively. Fire₂ shows the lowest correlation with $r_s = 0.09$. All results, for both GST and ALT are insignificant.

Negative correlation for LST~GST means an increase in LST results in a decrease of GST (meaning cooler temperatures), while a positive correlation means that with increasing LST the GST increases as well resulting in warmer ground temperatures. This holds true for the fires_{3,8,9}. For ALT, the positive correlation means with an increase in LST, the ALT increases. A negative correlation would lead to a decrease in ALT within increase of LST. This holds true for fire₂, the others all show positive correlations.

5. Discussion

5.1. LST

The Landsat LST used in this analysis has a spatial resolution of 30 m and was processed by using the SC-algorithm in the GEE (Jiménez-Muñoz and Sobrino, 2003; Sobrino et al., 2004), including products on the column water vapor (NCEP/NCAR). Even though, no ground-truth data as absolute referencing of LST products existed, plausible remote estimation of LST has been gained in previous studies applying the algorithm (Nill et al., 2019). Nevertheless, LST is very sensitive to short-term changes of insolation and air temperature, causing rapidly changing insolation rates and surface warming (Nill et al., 2019). Additionally, uncertainties evolve concerning permafrost ground properties, which are highly heterogeneous in space and time and influence the heat fluxes. Furthermore, investigating Landsat-based LST development is restricted to summer months, due to cloud and snow coverage also influencing the total amount of LST data per year. Therefore, lack of LST data, particularly from 2006 to 2010 causes uncertainties in time series. High temperatures already occur before the fire event as a consequence of one value for the entire year. For example, fire₂ shows one value as highest temperature of 28.76°C in 2006. Regarding the slopes, this results in an overestimation before the fire. Therefore, for the year 2010, many time series show very low values with 13.69°C for fire₃. This is also a result of fewer data per year. Consequently, the comparison between values before and after the fire should be regarded carefully. Disregarding the year of fire occurrence, some time series show great outliers, like fire₂ with the highest LST of 27°C in 2018. Besides the lack of data, this might be due to the warmest decades on record from 2011 – 2020 (WMO). As the strong increase in temperature is seen in both time series, fire and control, the impact of climate warming is prevalent. The standard deviation is quite high with 8°C, especially for the fire areas than control areas, and are highest around the fire year. Among others, this could be due to the misclassification of active burned pixels. Differences in LST may be partly caused by active fires, as flagged as invalid LST values in quality control, rather than post-fire effects. Even though the pixel size is quite accurate, pixels may cover mixing surface conditions of burned and unburned pixels mostly around the fire perimeter. Uncertainties due to pixel misclassification may also have evolved using the LandTrendr algorithm to detect fire areas. The LT algorithm has a low ability to detect low severity burned areas (Quintero et al., 2019), probably due to the phenological cycle and sun-angle. Another reason might be the complexity of the LT, including many control parameters adjusted to the predominant ecosystem type. Hence, a strong sensitivity to incorrect calibration is assumed (Quintero et al., 2019). Nevertheless, when studying the variations of post-fire regeneration of vegetation, the LT algorithm develops solid change metrics like year and duration (Quintero et al., 2019).

Regarding the year of disturbance and post-fire development of LST for the study areas, changes in

5. Discussion

LST are visible but vary in magnitude. Taiga has a stronger LST response than Tundra, as greater differences after the fire for southern regions with 2.05°C (fire_1) than northern regions with 0.61°C (fire_9) occur, regardless length of time series. Tundra fires lead to a slight difference of fire and control area in LST 1 year after the fire, with a relatively fast alignment of 1 to 3 years, leading to an exceedance of $\text{LST}_{control}$ in reference to LST_{fire} . Taiga wildfires have a warming effect on annual LST 1 year after the fire and result in an overall increasing trend in LST within the years after the fire. It takes 3 to 5 years to align to $\text{LST}_{control}$, but never reaches the same LST as for the control area at the end of the time series plot. Confirming the results, the warming effects 1 year after the wildfire have also been observed in several previous studies for other boreal forest permafrost regions (Oris et al., 2014; Randerson et al., 2006).

Regardless of the slopes before the fire due to uncertainties, both fire and control areas after the fire show the same pattern but with different intensities. They are generally higher for the fire area than the control area. Positive LST trends at the fire area are mainly seen for fires occurring in 2014 with exception of fire_6 also exhibiting a positive slope with $ts = 0.27$, but occurred in 2010. fire_8 occurred in 2014, but shows a negative slope with $ts = -0.07$. As fires in 2014 are not very well recovered yet due to the short time period of 6 years, the short-term warming trend after the fire is just visible. fire_6 has a very slow recovery rate, which might be the cause of the prevalent warming trend after 10 years. fire_8 shows a cooling effect, even though it occurred in 2014. This might be due to data uncertainties or other driving factors which are not included in this study. Otherwise, negative cooling trends are visible for fires occurring in 2009, probably due to the longer time for recovery. The steepness of slopes after the fire is greater in the south than in the north, due to greater changes in LST. On one hand, variances in fire occurrence (2009 and 2014) make it difficult to compare the areas and to make statements on the long-term effects of fires in 2014. On the other hand, the distinction between short-term warming effects (1-6 years) and long-term cooling effects (6-11 years) is pronounced.

As algorithmic model corrections are based on real sample data, improvements could be achieved by the combination of real-time monitoring images (like on-site monitoring or drone aerial surveys) with the already used historical remote sensing image. For comparison, Hu and Hu (2020) suggest the usage of more high-resolution, historical images for real sample selection, like QuickBird, Worldview, Pleiades, and other images. Additionally, downsampling of MODIS data with a higher temporal resolution seems to show promising results for mapping wildfires and burn severity (Kolden and Rogan, 2013).

5.1.1. NBR and dNBR

Compared to standard approaches for calculating the burn severity, where only one pre- and post-fire scene are used, the approach by Parks et al. (2018), which was applied in this study, uses a mean composite fire severity dataset. Hence, the greater validation statistics are leading to higher classification accuracies for most of the severity classes (Parks et al., 2018). Because of the compositing method, fire-induced ecological changes can be recorded more accurately as this method is less biased by pre-and post-fire scene mismatch. Additionally, the low severity burn should be treated with special care, as predominantly small changes in vegetation may be detected as such. The chances of misclassification increases if the composited image collection includes a long time period or when the

5. Discussion

distances between these periods gets to expanded. Therefore, it is crucial to know the exact time period of the wildfire as possible, before proceeding with the analysis. Regarding this information, an appropriate time window was designated to minimize the errors. (Kolden and Rogan, 2013) mentioned, that the image compositing, including the period one year after the fire, may not be suitable for all ecosystems. He argues that for the Arctic Tundra it may be better to use images derived directly after the fire/ snowmelt but before green-up the year after the fire. This was tested for fires₇₋₉, showing more high severity burn patches. But due to the short time period, no to very few images lead to the result, which leads to the beginning where one pre-and post-fire image causes uncertainties in results. Therefore, it could be possible that the BS was underestimated for fires₇₋₉, but due to the fewer amount of images, this method was rejected.

The NBR was used to determine whether the post-fire LST changes can be related to fire events and not other factors, which was confirmed for all fires. As the changes in LST are closely related to the prevailing vegetation type, burn severity, and hence recovery rate, the NBR and dNBR were additionally used as supporting data. In this study, the focus was on the recovery period for NBR and not NDVI. This has to be kept in mind when talking about vegetation recovery, as they both show different periods of generally 7-10 years for NDVI and even longer with 15-20 years for NBR until they return to pre-fire state (Shvetsov et al., 2019).

The NBR shows a direct decrease of surface vegetation after the wildfire event for all study sites, but the manifestation of the regeneration process is diverse. It ranges from a fast regrowth for the northernmost wildfires with a mean dNBR after the fire of -0.12 (fire₉), to intermediate regrowth for the more southernmost fires with 0.25 (fire₁). Outliers occur though. Fire₂ shows the highest dNBR with - 0.39 and fire₇ the lowest with -0.11. Hence, the fires in the south have experienced a more severe burn, than fires in the north.

This may be explained by the change in vegetation type from Larch forests to shrubland and burn severity, as driving factors of boreal forest restoration capacity and ecosystem resilience. Field studies also verified that herbaceous and shrub species growth was especially subject to an increase in NBR (Bright et al., 2019). This would explain the fast recovery of the Tundra fire areas, without reaching the control area for the studied time period. If the BS is low, as it is for the northernmost wildfires, vegetation can quickly recover to pre-fire states (Li et al., 2004). But even severe burns could have caused a faster recovery in the north, as it states preferable recovery conditions for shrubs and grasses (Chu et al., 2017) further intensifying Tundra shrubification (expansion of shrubs) and vegetation composition shifts (Sizov et al., 2021). On the positive side, this shift could lead to the enhancement of carbon sink (Kalliokoski et al., 2019). Overall, detailed comprehensive long-term satellite remote sensing data is of great importance and need. Therefore, the intermediate recovery of the southernmost wildfires may be a result of the high burn severity together with the existence of Larch trees. They recover best in sites of moderate burn severity, but not severe burn (Chu et al., 2017).

The main advantage of the burn severity analysis is given by the composite of the instantaneous wildfire impact and the regrowth of vegetation. As it is a change detection process, it is also possible that changes in the environment, which are not fire-related, may be mistakenly detected as wildfire damage. Non-fire-related changes could be changes in natural vegetation, other land cover changes, and deforestation. Even though, snow, clouds, and shadow masking have been applied in the pre-

5. Discussion

processing steps, masking algorithms sometimes still fail to remove all instances. For example, it is possible that shadows will not be caught entirely, leading to false detection afterward as dark shadow pixels can be assumed to be burned pixels or enhanced regrowth.

More studies are required around the northern permafrost landscapes, especially Tundra ecosystems, to get a deeper understanding of links between ecosystem processes and fire impacts. As fires are about to spread to the Tundra ecosystem in the past years, it is rather difficult to get long time series from remote sensing data. Additionally, the amount of Tundra wildfires to study on is small, leading to a comparison of one Tundra wildfire against 8 Taiga wildfires in this study. More wildfires including longer time series are necessary, to make more reliable future predictions.

5.2. GST and correlation with LST

The analysis of the coherence between GST and LST was impaired by uncertainties caused by the data basis. Permafrost data was just available as an entire yearly mean at a very coarse spatial resolution. Therefore, Landsat LST data was present with a high spatial resolution but just means of the summer months. To at least reduce the uncertainties due to the disparity of pixel sizes, the LST data were resampled for correlation, leading to better results. But still, due to different time periods, it is difficult to compare the datasets gaining absolute values and therefore reliable results. Even though, the correlation analysis fraught with uncertainties, conclusions on the coherences could be drawn comparing the trends and statistics of GST and ALT time series with LST time series. Based on the residuals, all visible changes in GST and ALT are related to the fire event, except fire₂ shows the contrary. As already mentioned, permafrost data is highly heterogeneous and as the resolution is very coarse, the contrast between fire and control could be diluted, causing an underestimation of means. Therefore, the choice of the control area could have caused uncertainties. As LST changes are also proofed to be fire-related by NBR, they can be compared with GST and ALT.

The times series, as well as the corresponding statistics, show that in generally differences after the fire are higher for the southernmost fires with 0.35°C (fire₁) and lower to the northernmost with -0.1°C (fire₉), with again a few exceptions given by fires_{3,5,6}, probably caused by permafrost heterogeneity. As time series for GST and ALT are longer and more consistent, slopes before the fire are more reliable than for LST.

For the control area, the slopes are all positive after the wildfire, possibly in relation to climate warming in the Arctic. Fire₁ shows an exception with a cooling effect, comparing Sen's slopes before and after the wildfire. As it is the southernmost area, possibly the great vegetation cover and occurrence of trees causes a shading effect. Therefore, the fire areas show slight changes in slope. Firstly, fires_{1,5} are showing a decreasing slope compared to the slopes before the fire, while all others increase. This means they show a cooling effect after the fire, instead of warming. GST is dependent on the surface organic layer, which controls the hydrological and thermal regimes closely with permafrost dynamics (Jin et al., 2008). Therefore, the decrease in fire₁ from 0.51°C to 0.30°C could be due to the long time period. As the fire occurred in 2009, the time of recovery is longer than for fires, which occurred in 2014. Within vegetation recovery over 11 years, might have caused the GST to get cooler again. The slight decreasing slope of fire₅ from 0.34°C before the fire and 0.32°C after the fire may also be a result

5. Discussion

of time since fire. The change in the degree of slope between fires_{1,5} may be caused by latitude changes. Slopes in the north (0.75°C for fire₈ and 0.59°C for fire₉) and south (0.81°C for fire₂ and 0.73°C for fire₃) are the highest. In the north probably due to the time since fire, which is a result of the strong increase. But as the control shows a nearly same pattern with less difference after the fire, gives reason to the assumption that climate warming could be a greater influence than in the south due to canopy. Time series show a great increase in GST since 2015 for most of the time series, which might be due to climate warming and could also influence the slope. Additionally, fires in the south have experienced a more severe burn, which might be the cause of the high value of 0.81°C. Comparing Sen's slopes of 2009/2010 wildfires, they are less steep than 2014, but slightly increase from south to north from 0.30 (fire₁) to 0.38 (fire₆). Even though the impact of fire on LST due to greater BS is higher in the south than in the north, the impact on GST seems to be slightly greater in the north than in the south regarding the slopes, even ranging from a negative trend before the fire to a positive trend after the fire. The comparison of 2014 fires occurring in the south ($ts = 0.73$ for fire₃) and north ($ts = 0.75$ for fire₈) shows almost the same value, even though the BS is higher in the south. As wildfires are predicted to be larger and more severe under a warmer future climate, this could cause great negative effects especially for permafrost in the Tundra.

Even though time series of GST and LST generally show a good positive consensus, the correlation analysis offers rather moderate correlation coefficients. Correlation results show a moderate positive correlation for fire₉ with $p = 0.39$ and fire₃ with $rs = 0.24$, meaning an increase in LST increases GST, causing a warmer soil surface. This can be mainly seen for fires occurring in 2014, except fire₂ with $rs = -0.46$. All other fires show a moderate negative correlation, meaning an increase in LST leads to a decrease in GST. The best correlation is given by fire₄ with $rs = 0.45$. As it is the fire area with the greatest extent of 243 km², calculated means from coarse GST pixels may have lead to more reliable results than for smaller fires. The correlation might increase though if longer averaging intervals (5-yr means) and longer times series will be present. Especially, the LST data for the non-summer months are needed to include inter-annual variability in the snow cover depth and duration.

Another way to improve the results would be the acquisition of more reliable permafrost data (in-situ or better resolution remote sensing data). Additionally, to solve the problem of temporal resolution, including MODIS data could be an option, especially when analyzing fire-affected areas with a greater extent than chosen fires in this study. Studies show a good agreement of MODIS-LST with ground surface temperature (Li et al., 2019). Even though in all plots effects of fire can be observed, some of them show warmer temperatures for the control area than for the fire. This might be due to the high spatial variability of permafrost ground temperatures. Therefore, the choice of the associated control areas might be reconsidered or a pixel-based regeneration index using time series similarity by Lhermitte et al. (2010) could be applied. The advantage of this approach is, that no reference maps are needed, minimizing the effect of spatial heterogeneity and noise. Despite limitations being prevalent, correlations between $LST \sim GST$ and $LST \sim ALT$ could have been improved by resampling LST data, showing moderate results.

5.3. ALT and correlation with LST

Changes in ALT times series after the fire are very low in magnitude. Hence, minimum changes regarding the mean dALT after the fire were observed for fire₃ with 0.0002 m and maximum changes are visible for fire₄ with 0.05 m. Uncertainties evolved for fires_{4,5} with generally greater ALT for the fire area over the entire time period and for fires_{2,6} with generally greater ALT for the control area over the entire time period. This may be due to the coarse spatial resolution as well as the strong heterogeneity of ALT. Hence, the control area may not be suitable. dALT shows the lowest values in the south with 0.0002 m (fire₃) and 0.0003 m (fire₁), even though the BS was the highest. Both show different processes in time series, resulting in a direct increase of ALT for fire₁ after the fire lasting for 4 years and adjusts over time within recovery. Therefore, fire₃ and also fire₂ display slight impacts on ALT only 4 years after the fire, with the ending of time series. Both scenarios might explain the low changes in ALT. Additionally, the organic layer (thermal conductivity and soil moisture) is the most important factor controlling ALT. If the organic layer is thick enough, which might be more predominant in the south due to higher vegetation intensity, it may not always affect the underlying permafrost. For example, Yoshikawa et al. (2002) suggest that if 7-12 cm of the organic layer in Alaskan boreal forests remains after a wildfire, the thermal impact on the permafrost becomes hardly apparent. Therefore, the fire severity is crucial for the post-fire ALT variation Li et al. (2021), influencing the organic layer thickness.

Fires_{4,5,6} show the greatest dALT after the fire ranging from 0.02 m to 0.05 m. But they are also fraught with uncertainties. Apart from that, all of them display a slight increase of ALT directly after the fire for 1-2 years and slowly adjust to $ALT_{control}$. Fires_{4,6} though, show another increase beginning in 2014, 4-5 years later. The same is visible for fires_{2,3}. The long time period after the fires and the increase nearly at the end of the time series might have caused the highest dALT values. Additionally, fires_{4,6} show the same pattern in NBR and dNBR with high burn severity and low recovery rates, which could have also caused an impact on the organic layer, resulting in an ALT increase. The northernmost fires_{8,9} show the same dALT of 0.005 m (fire₈) and -0.005 m (fire₉). Fire₈ points slight changes directly after the fire, while fire₉ shows rather a decrease of ALT, especially in 2017. But it is difficult to make reliable statements on the development of ALT, as time series are very short after the fire and it is possible, that both pass the same progress as fires in the south. But it is also possible that due to the low burn severity the organic layer was not really harmed. Even though the GST is an instant driver of ALT dynamics (Bai et al., 2018), slopes do not show the same trends for all fires.

All in all, ALT over time can have very different patterns, as it is dependent on many factors. Some studies show an insignificant increase in the first year, followed by a rapid increase in the second year. At the 8th to 10th year after the fire, a stabilisation of ALT occurs leading to maximum thawing between the 5th and 10th year after fire (Gibson et al., 2016; Holloway et al., 2020; Viereck, 1982). Therefore, some studies have shown that the ALT does not increase significantly during the first five years after a severe burn, but increases rapidly during the second five years, leading to a peak thaw depth at the 25th year after burn (Viereck et al., 2008). Hence, some time series might be too short to make reliable statements of post-fire ALT development.

Overlooking the slopes, the same development is confirmed. The slopes of the fire area after the

5. Discussion

fire compared to before, fire_{2,3} show an increase in ALT from 0.005 to 0.025 (fire₂) and 0.006 to 0.024 (fire₃), while all the others show a decrease of ALT after the fire event. Fire_{2,3} show an increase of ALT compared to the control area at the fourth year after the fire, stating at the same time the end of the time series. Longer time series, including recovery, may lead also to a negative trend. The strong increase is also visible for the control area and might be related to global warming in the past few years. Additionally, the severe burn for fires_{2,3} might have caused a thickening in ALT. Regarding fires in the north (2014) with slopes of $ts = -0.013$ (fire₈) and $ts = -0.022$ (fire₉), impacts of fire may not have occurred until 2018 or because of the low BS, the organic layer was not harmed enough to cause the ALT to increase. Looking at longer time series negative trends might be explained by the recovery, as within gradual restoration of vegetation and therefore regeneration of organic layer, the ALT gradually decreases (Nossov et al., 2013; Yoshikawa et al., 2002).

As last point, the coherence of LST and ALT shall be discussed, regarding their overlapping time series from 2006-2018. The moderate-good correlation between ALT and LST is also seen in the results of this study. The correlations show moderate positive trends ranging from $rs = 0.15$ (fire₃) to $rs = 0.63$ (fire₉) for all fires, except fire₂ with $rs = -0.09$ showing a negative trend. The positive trend would mean that with increasing LST, the ALT would increase as well. For fire₂, the ALT decreases within LST increase, possibly due to data uncertainties. Data for GST as well as ALT is insignificant. The correlation seems to be stronger in the north than in the south, probably due to direct effects and shorter time period after the fire event.

Nevertheless, the satellite analysis of frozen ground regarding its land surface characteristics remains challenging due to unfortunate conditions, such as constant cloud coverage, little brightness intensity, sharp sun angles, and technical limitations (Duncan et al., 2020). Additionally, large uncertainties are associated with the high spatial variability of permafrost ground and difficulties in the exact determination of LST due to heterogeneity.

6. Conclusion and outlook

Wildfires have a great influence on the permafrost environment, but their magnitude is dependent on various factors like organic layer thickness and vegetation type, soil moisture and soil type, elevation, burn severity, and vegetation recovery. In this study, the focus lay on the consideration of the burn severity together with recovery rate and the vegetation type regarding differences between Taiga and Tundra ecosystems.

On the basis of the calculated LST time series, conclusions and coherences to the impact on permafrost have been drawn, regarding GST and ALT. Short-term effects show a warming effect for both, Taiga and Tundra permafrost parameters together with an increase in LST. Even though the Tundra exhibits less burn severity and high recovery rates, the impact on permafrost is greater as Sen's slopes are steeper. Therefore, long-term effects show a cooling effect for the Taiga related to the vegetation recovery. Long-term trends for the Tundra could not be determined due to lack of data, as Tundra fires in the study area became only more predominant in the past 6 years. Fires are predicted to be larger, more severe, and higher in frequency related to future climate warming, which raises the concern that fires, especially in the Tundra due to dryer more flammable vegetation, will be more harmful to permafrost, contributing even more to positive climate feedback in Arctic permafrost regions, although this feedback may become negative if the fire frequency would long enough to allow the vegetation to recover and Arctic greening occurs. But regarding the current state of research, one can assume that for future wildfires the cooling effect from long-term post-fire LST and GST will be reduced due to climate change.

To improve future research, the data basis (in-situ and remote-sensing-based) especially for the Tundra needs to be improved including longer consistent time series. Additionally, the number of studied Tundra fires should be raised regarding other study sites along the Siberian Tundra regions, to include more reference data. As the last point, further major parameters impacting the permafrost, like soil moisture, should be studied and compared with present data to better understand the overall content and to make even more reliable future predictions.

Appendix A.

Values and coefficients

Parameter	Values
maxSegements	3
spikeThreshold	0.6
vertexCountOvershoot	4
preventOneYearRecovery	true
recoveryThreshold:	0.3
pvalThreshold:	0.1
bestModelProportion:	0.75
minObservationsNeeded:	6

Table A1.: Parameters used for the LT algorithm.

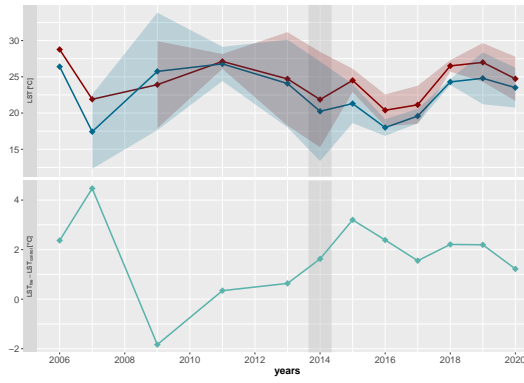
Sensor	Coefficients
Landsat-5 TM	[0.07518 -0.00492 1.03189
	-0.59600 -1.22554 0.08104
	-0.02767 1.43740 -0.25844]
Landsat-t ETM+	[0.06518 0.00683 1.02717
	-0.53003 -1.25866 0.10490
	-0.01965 1.36947 -0.24310]
Landsat-8 OLI-TIRS	[0.04019 0.02916 1.01523
	-0.38333 -1.50294 0.20324
	0.00918 1.36072 -0.27514]

Table A2.: Coefficients used to calculate the AFs.

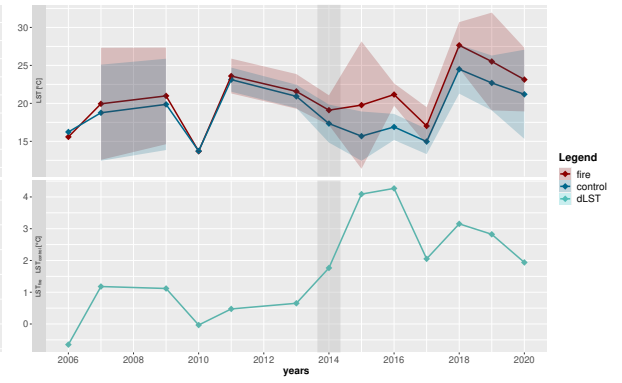
Appendix B.

Graphs and tables

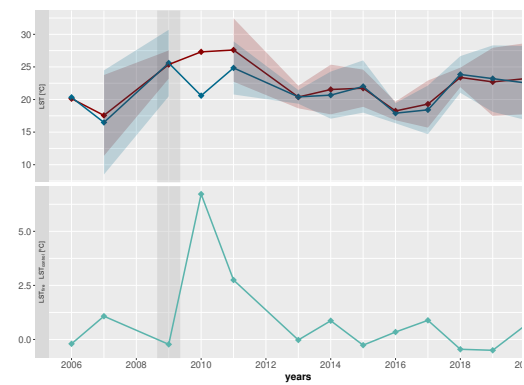
Appendix B. Graphs and tables



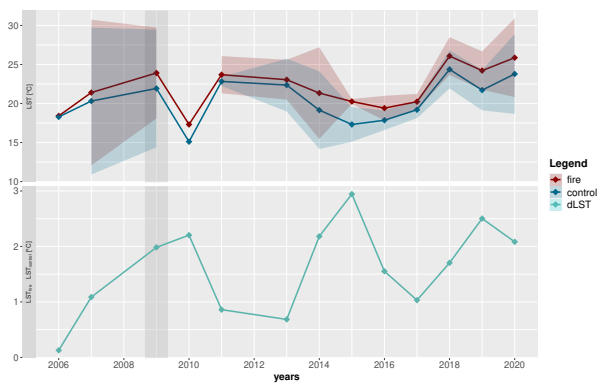
(b) Fire₂.



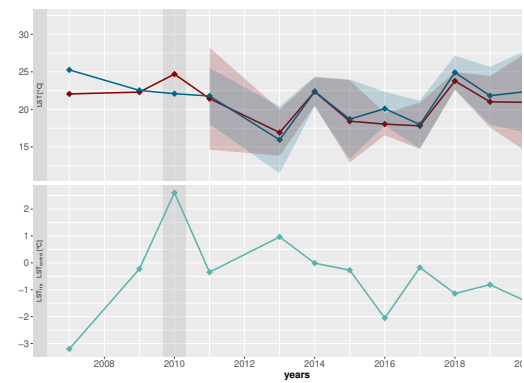
(c) Fire₃.



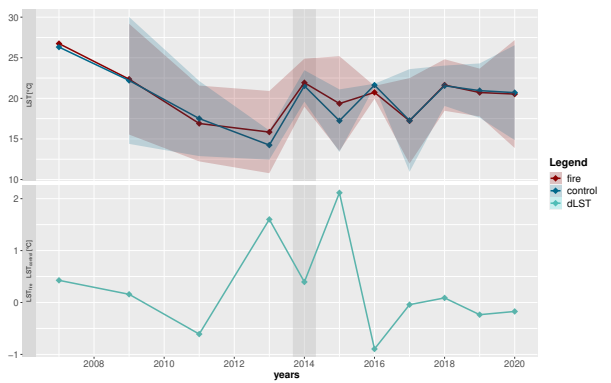
(d) Fire₅.



(e) Fire₆.



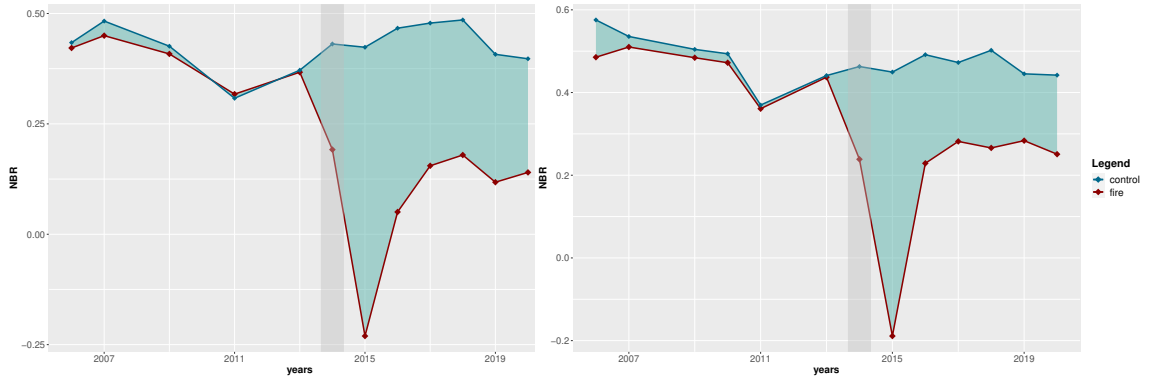
(f) Fire₇.



(g) Fire₈.

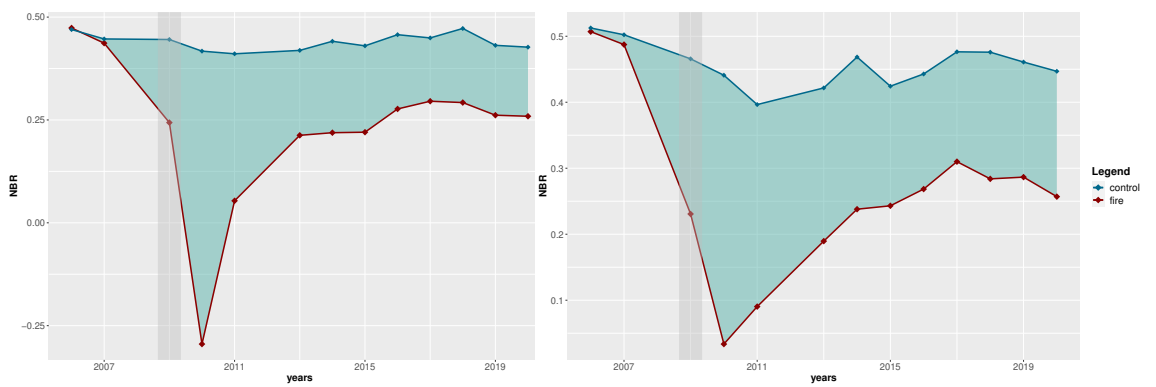
Figure B1.: Yearly summer mean LST time series of fire and control areas.

Appendix B. Graphs and tables



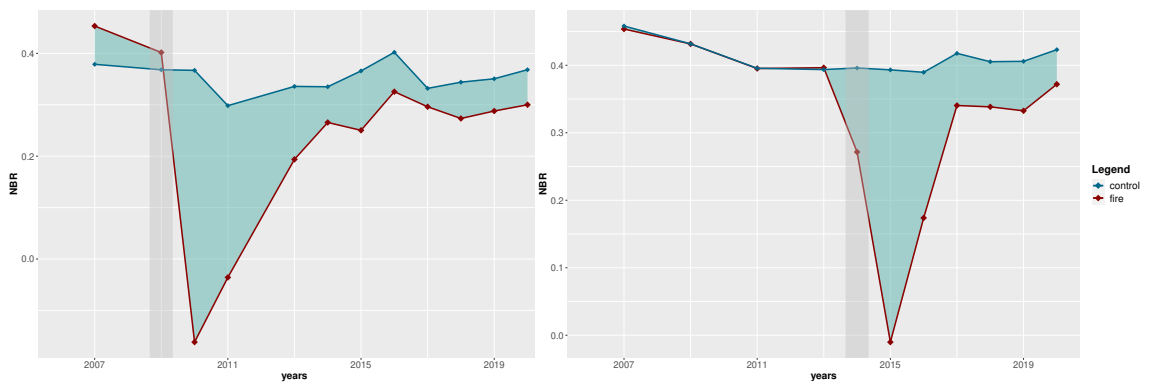
(a) Fire₂.

(b) Fire₃.



(c) Fire₅.

(d) Fire₆.

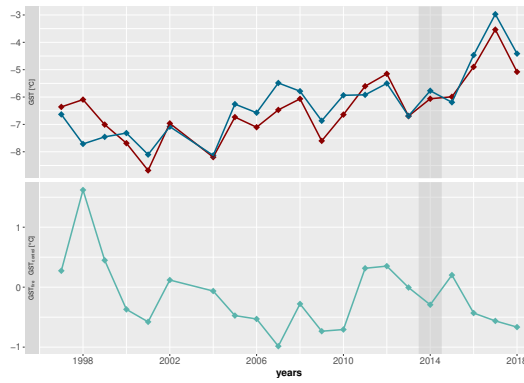


(e) Fire₇.

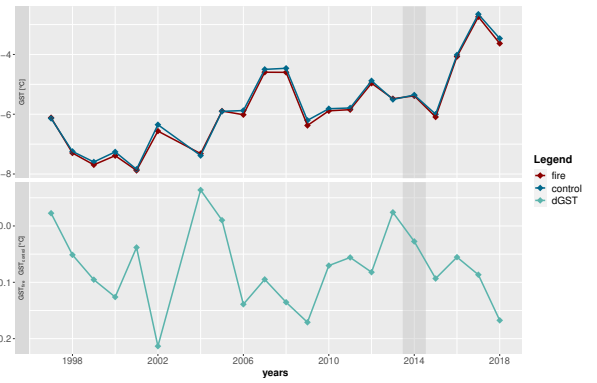
(f) Fire₈.

Figure B2.: Yearly summer mean NBR time series of fire and control areas.

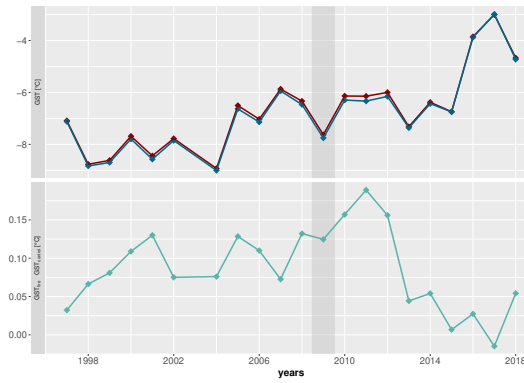
Appendix B. Graphs and tables



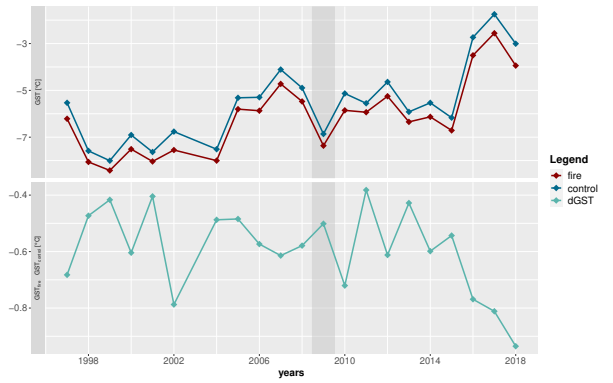
(a) Fire₂.



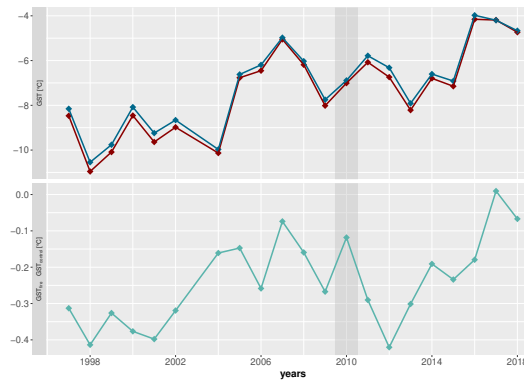
(b) Fire₃.



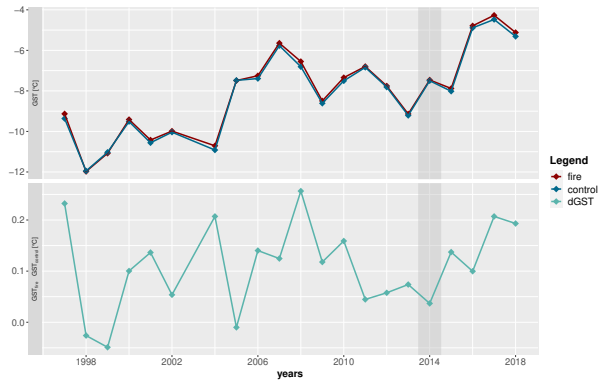
(c) Fire₅.



(d) Fire₆.



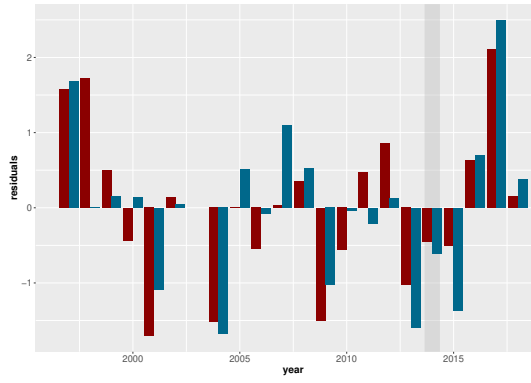
(e) Fire₇.



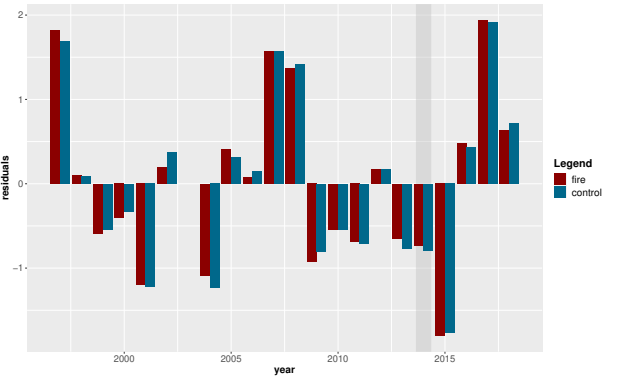
(f) Fire₈.

Figure B3.: Yearly mean GST time series of fire and control areas.

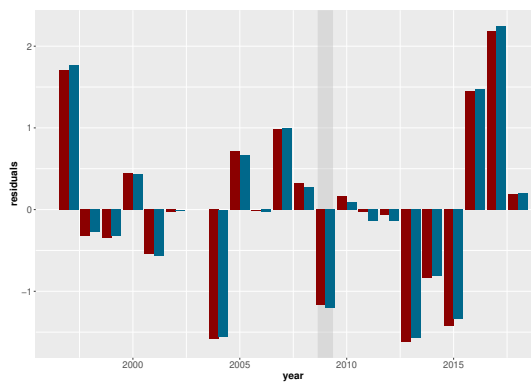
Appendix B. Graphs and tables



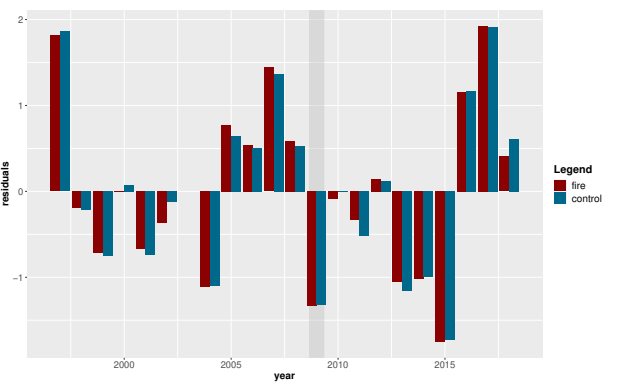
(a) Fire₂.



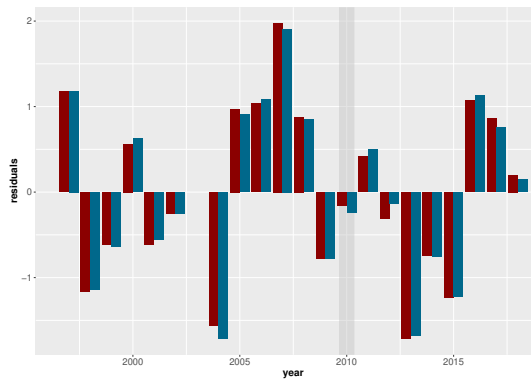
(b) Fire₃.



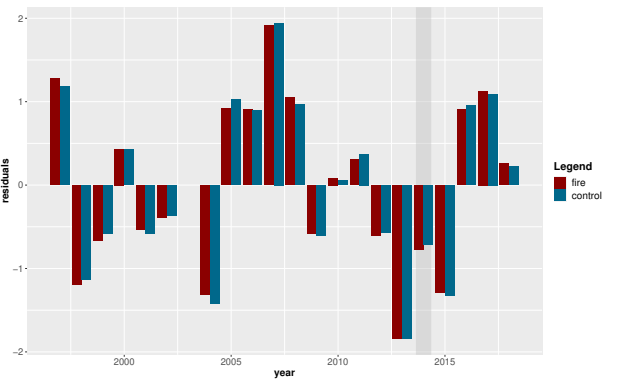
(c) Fire₅.



(d) Fire₆.



(e) Fire₇.



(f) Fire₈.

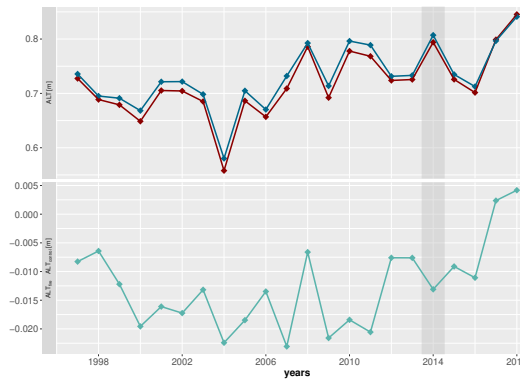
Figure B4.: Visualization of GST residuals.

Appendix B. Graphs and tables

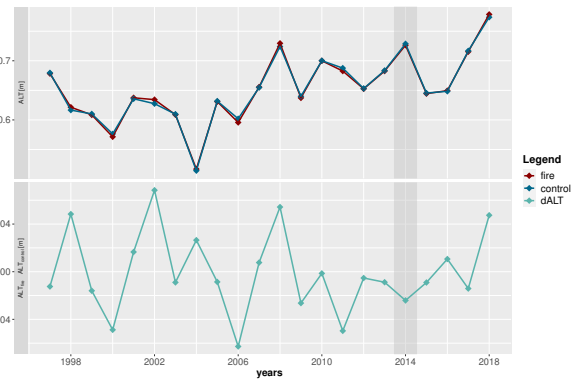
year	fire1	con1	fire2	con2	fire3	con3	fire4	con4	fire5	con5	fire6	con6	fire7	con7	fire8	con8	fire9	con9
1997	1.57	1.48	1.57	1.68	1.81	1.68	1.93	2.05	1.71	1.77	1.81	1.86	1.17	1.18	1.28	1.18	0.92	0.94
1998	1.72	1.61	1.72	0.01	0.10	0.08	-0.20	-0.13	-0.32	-0.27	-0.19	-0.21	-1.16	-1.14	-1.18	-1.12	-1.56	-1.56
1999	0.49	0.41	0.49	0.15	-0.59	-0.54	-0.34	-0.45	-0.35	-0.32	-0.71	-0.75	-0.61	-0.64	-0.66	-0.57	-0.62	-0.61
2000	-0.43	-0.388	-0.43	0.13	-0.40	-0.32	0.12	0.02	0.44	0.43	-0.00	0.07	0.56	0.63	0.43	0.43	0.52	0.48
2001	-1.70	-1.64	-1.70	-1.08	-1.20	-1.22	-0.70	-0.75	-0.54	-0.56	-0.67	-0.73	-0.61	-0.55	-0.53	-0.58	-0.38	-0.35
2002	0.13	0.21	0.13	0.04	0.20	0.37	0.05	0.09	-0.03	-0.01	-0.37	-0.12	-0.25	-0.24	-0.39	-0.36	-0.18	-0.19
2004	-1.52	-1.68	-1.52	-1.67	-1.09	-1.23	-1.34	-1.15	-1.58	-1.55	-1.11	-1.09	-1.56	-1.71	-1.31	-1.42	-1.43	-1.44
2005	-0.00	-0.07	-0.00	0.51	0.41	0.31	0.52	0.62	0.71	0.66	0.77	0.64	0.97	0.90	0.91	1.02	0.80	0.78
2006	-0.54	-0.38	-0.54	-0.07	0.07	0.15	-0.04	-0.11	-0.01	-0.03	0.54	0.50	1.03	1.07	0.90	0.89	0.99	1.00
2007	0.02	0.30	0.02	1.10	1.56	1.56	1.10	1.01	0.98	0.99	1.44	1.36	1.97	1.90	1.91	1.94	2.16	2.18
2008	0.34	0.52	0.34	0.53	1.36	1.42	0.28	0.15	0.32	0.27	0.58	0.53	0.87	0.84	1.05	0.96	1.16	1.19
2009	-1.50	-1.45	-1.50	-1.02	-0.92	-0.80	-1.19	-1.29	-1.17	-1.20	-1.32	-1.32	-0.77	-0.77	-0.58	-0.60	-0.33	-0.34
2010	-0.55	-0.46	-0.55	-0.03	-0.54	-0.54	0.06	0.01	0.16	0.08	-0.09	0.01	-0.15	-0.23	0.08	0.05	0.17	0.17
2011	0.47	0.18	0.47	-0.20	-0.69	-0.70	-0.24	-0.19	-0.03	-0.13	-0.33	-0.51	0.41	0.50	0.31	0.37	0.42	0.36
2012	0.85	0.64	0.85	0.12	0.16	0.16	0.04	0.13	-0.06	-0.14	0.14	0.11	-0.31	-0.13	-0.60	-0.56	-0.55	-0.51
2013	-1.02	-0.97	-1.02	-1.59	-0.64	-0.76	-1.33	-1.31	-1.62	-1.57	-1.05	-1.16	-1.71	-1.67	-1.84	-1.84	-1.77	-1.80
2014	-0.44	-0.37	-0.44	-0.60	-0.73	-0.79	-0.91	-0.91	-0.83	-0.80	-1.02	-0.99	-0.74	-0.75	-0.77	-0.71	-0.62	-0.58
2015	-0.50	-0.51	-0.50	-1.36	-1.80	-1.77	-1.54	-1.55	-1.42	-1.33	-1.75	-1.72	-1.23	-1.21	-1.29	-1.32	-1.33	-1.30
2016	0.63	0.89	0.63	0.69	0.47	0.43	1.24	1.30	1.44	1.47	1.16	1.16	1.06	1.13	0.90	0.94	0.83	0.83
2017	2.10	2.27	2.10	2.49	1.94	1.91	2.36	2.27	2.18	2.24	1.92	1.91	0.85	0.75	1.12	1.09	0.44	0.43
2018	0.15	-0.32	0.14	0.37	0.63	0.72	0.31	0.40	0.19	0.20	0.40	0.61	0.20	0.15	0.26	0.22	0.28	0.25

Table B1.: Residuals of GST.

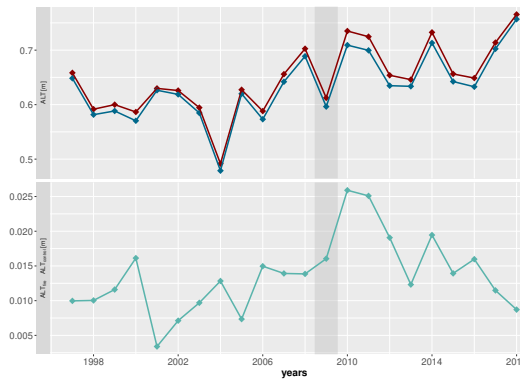
Appendix B. Graphs and tables



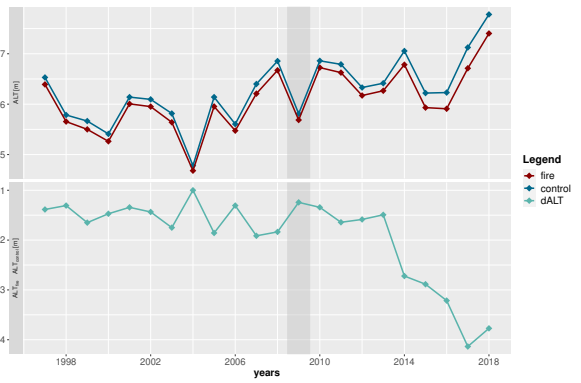
(a) Fire₂.



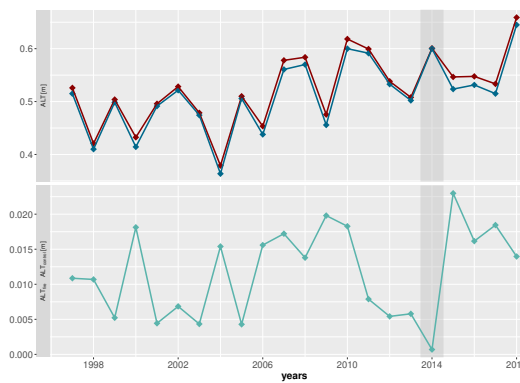
(b) Fire₃.



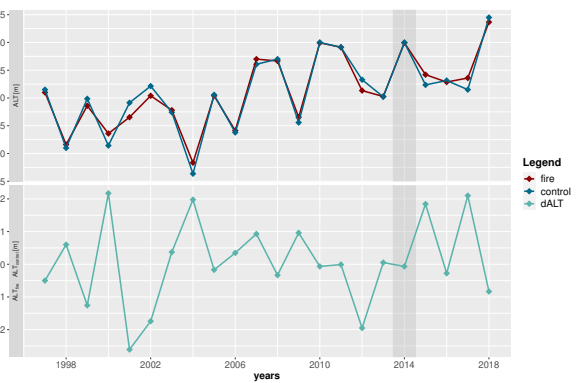
(c) Fire₅.



(d) Fire₆.



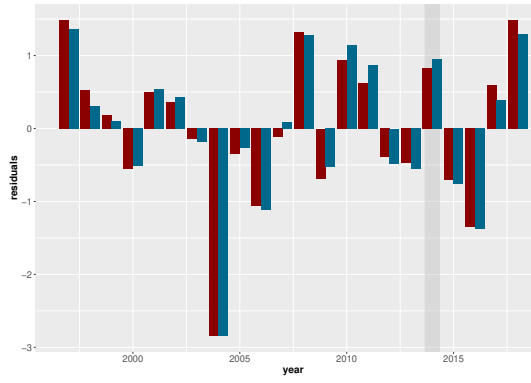
(e) Fire₇.



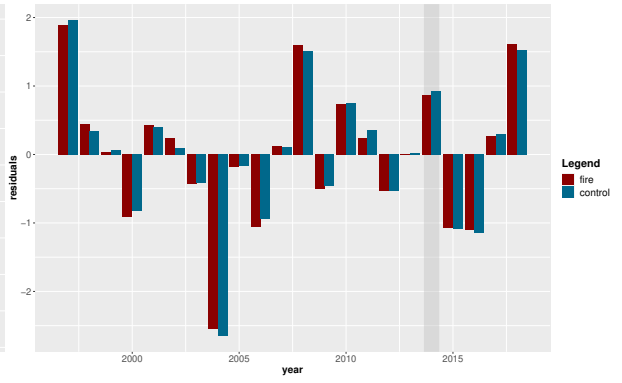
(f) Fire₈.

Figure B5.: Yearly mean ALT time series of fire and control areas.

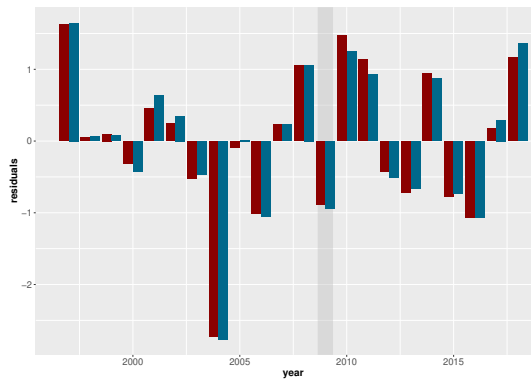
Appendix B. Graphs and tables



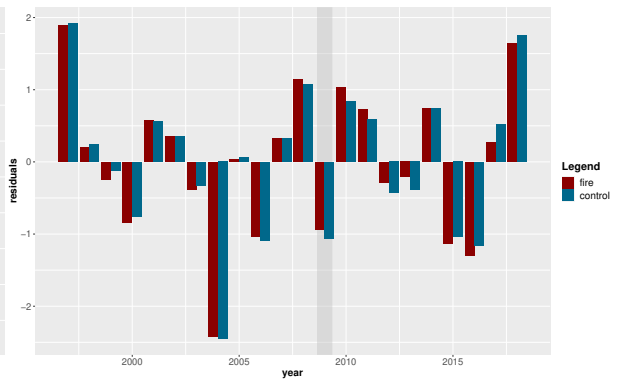
(a) Fire₂.



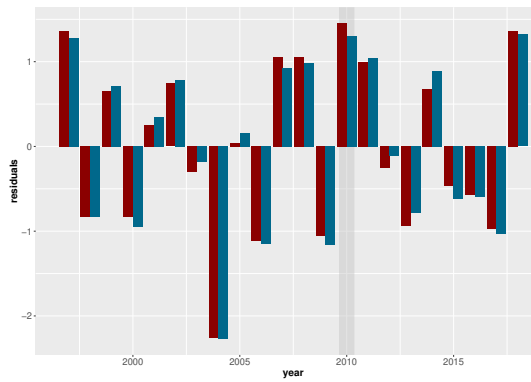
(b) Fire₃.



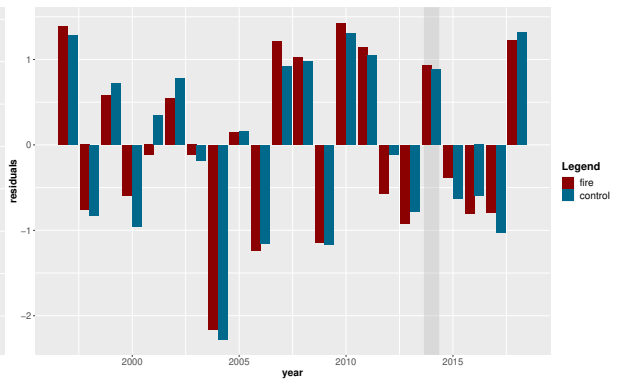
(c) Fire₅.



(d) Fire₆.



(e) Fire₇.



(f) Fire₈.

Figure B6.: Visualization of ALT residuals.

Appendix B. Graphs and tables

year	fire1	con1	fire2	con2	fire3	con3	fire4	con4	fire5	con5	fire6	con6	fire7	con7	fire8	con8	fire9	con9
1997	1.55	1.71	1.48	1.36	1.89	1.96	1.73	1.74	1.62	1.64	1.89	1.92	1.35	1.27	1.38	1.28	1.35	1.41
1998	1.21	1.20	0.52	0.31	0.44	0.34	0.35	0.26	0.05	0.06	0.19	0.24	-0.82	-0.82	-0.76	-0.82	-1.05	-1.06
1999	0.12	0.05	0.19	0.10	0.02	0.07	0.09	-0.11	0.09	0.08	-0.24	-0.12	0.65	0.71	0.58	0.71	0.49	0.47
2000	-0.90	-0.79	-0.55	-0.51	-0.91	-0.82	-0.57	-0.82	-0.31	-0.41	-0.84	-0.75	-0.82	-0.95	-0.59	-0.95	-0.76	-0.74
2001	0.20	0.12	0.50	0.54	0.43	0.40	0.45	0.60	0.45	0.63	0.57	0.56	0.25	0.34	-0.11	0.34	0.10	0.09
2002	0.50	0.44	0.36	0.43	0.24	0.09	0.28	0.52	0.25	0.34	0.35	0.35	0.74	0.78	0.54	0.78	0.63	0.61
2003	-0.42	-0.40	-0.14	-0.19	-0.43	-0.41	-0.38	-0.27	-0.51	-0.47	-0.38	-0.32	-0.30	-0.18	-0.11	-0.18	-0.02	-0.10
2004	-2.98	-3.08	-2.84	-2.84	-2.54	-2.65	-2.70	-2.60	-2.72	-2.76	-2.42	-2.45	-2.26	-2.27	-2.15	-2.27	-2.03	-2.16
2005	-0.58	-0.55	-0.34	-0.26	-0.18	-0.16	-0.30	-0.21	-0.09	0.01	0.03	0.06	0.04	0.16	0.14	0.16	0.14	0.17
2006	-0.87	-0.70	-1.05	-1.12	-1.05	-0.93	-1.15	-1.09	-1.01	-1.05	-1.03	-1.09	-1.11	-1.15	-1.24	-1.15	-1.19	-0.90
2007	-0.33	-0.20	-0.11	0.09	0.12	0.10	0.15	0.28	0.23	0.22	0.32	0.32	1.05	0.92	1.21	0.92	1.20	1.22
2008	1.35	1.37	1.32	1.27	1.60	1.51	1.01	1.07	1.05	1.06	1.14	1.07	1.05	0.98	1.02	0.98	0.76	0.74
2009	-0.53	-0.82	-0.68	-0.52	-0.50	-0.46	-0.82	-0.92	-0.88	-0.93	-0.93	-1.06	-1.05	-1.16	-1.13	-1.16	-0.97	-1.05
2010	0.67	0.54	0.93	1.13	0.73	0.75	1.25	1.08	1.46	1.24	1.04	0.84	1.45	1.30	1.42	1.30	1.72	1.77
2011	0.78	0.72	0.62	0.87	0.24	0.35	0.94	0.88	1.13	0.93	0.73	0.58	0.99	1.04	1.14	1.04	0.92	0.85
2012	0.23	0.04	-0.38	-0.47	-0.52	-0.52	-0.24	-0.17	-0.42	-0.51	-0.29	-0.43	-0.25	-0.11	-0.57	-0.11	-0.08	-0.09
2013	-0.36	-0.36	-0.47	-0.55	0.01	0.02	-0.37	-0.44	-0.71	-0.66	-0.21	-0.39	-0.94	-0.78	-0.91	-0.78	-0.95	-0.99
2014	0.43	0.46	0.82	0.94	0.86	0.92	0.82	0.68	0.94	0.87	0.73	0.74	0.67	0.88	0.93	0.88	0.88	0.87
2015	-0.16	-0.06	-0.71	-0.75	-1.07	-1.08	-0.77	-0.87	-0.76	-0.73	-1.12	-1.04	-0.46	-0.62	-0.38	-0.62	-0.41	-0.43
2016	-1.23	-1.07	-1.34	-1.37	-1.09	-1.14	-1.15	-1.18	-1.06	-1.06	-1.29	-1.15	-0.57	-0.59	-0.79	-0.59	-0.69	-0.84
2017	0.30	0.55	0.59	0.40	0.27	0.30	0.00	0.13	0.17	0.29	0.26	0.52	-0.97	-1.02	-0.78	-1.02	-1.24	-1.02
2018	1.19	1.03	1.48	1.29	1.61	1.52	1.52	1.59	1.16	1.35	1.63	1.75	1.35	1.32	1.23	1.32	1.19	1.19

Table B2.: Residuals of ALT.

Appendix B. Graphs and tables

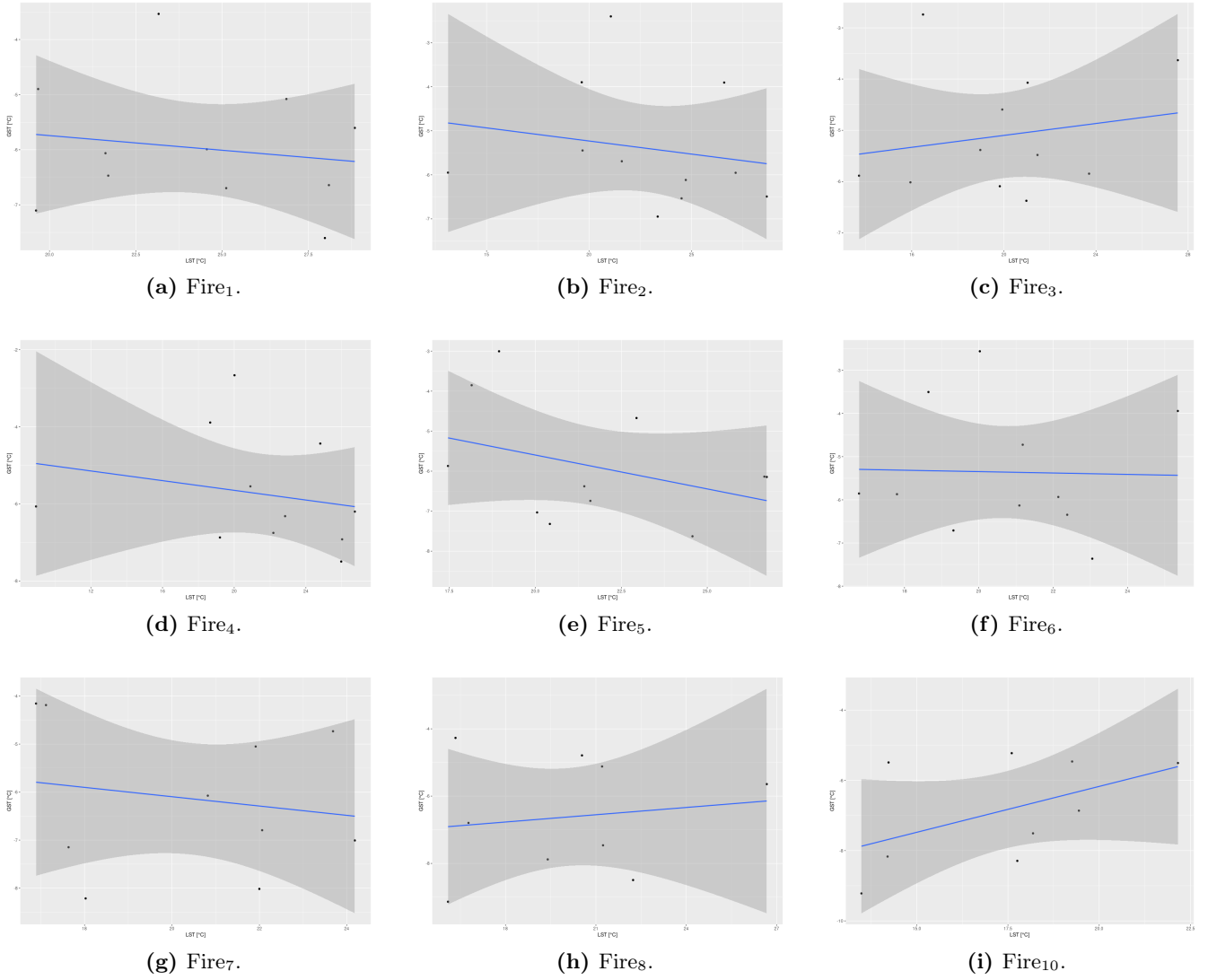


Figure B7.: Correlation of LST and GST.

Appendix B. Graphs and tables

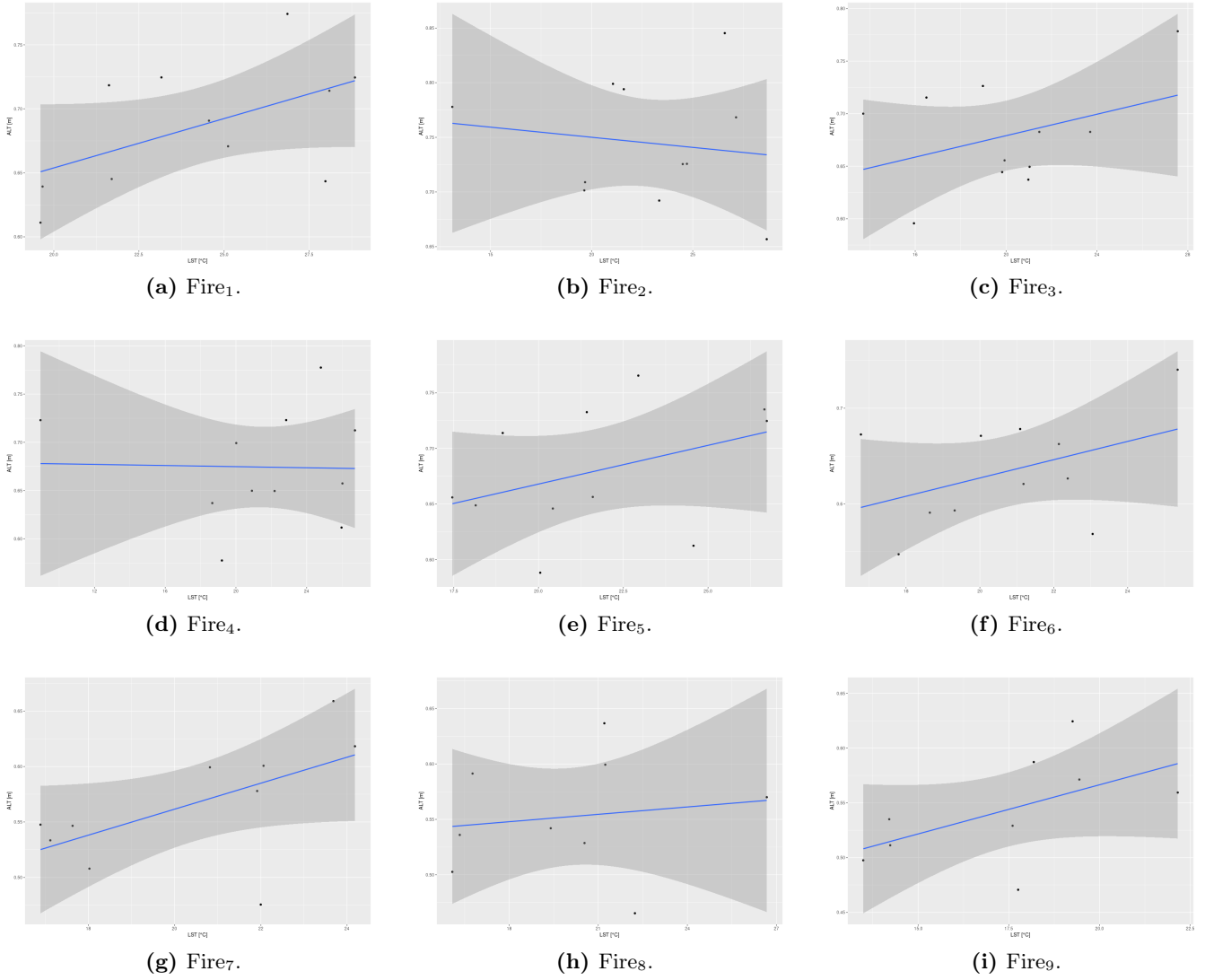


Figure B8.: Correlation of LST and ALT.

Bibliography

- Abbott, B. W., Jones, J. B., Schuur, E. A. G., Chapin III, F. S., Bowden, W. B., Bret-Harte, M. S., Epstein, H. E., Flannigan, M. D., Harms, T. K., Hollingsworth, T. N., et al. (2016). Biomass offsets little or none of permafrost carbon release from soils, streams, and wildfire: an expert assessment. *Environmental Research Letters*, 11(3):034014.
- Bai, X., Yang, J., Tao, B., and Ren, W. (2018). Spatio-temporal variations of soil active layer thickness in chinese boreal forests from 2000 to 2015. *Remote Sensing*, 10(8):1225.
- Barrett, K., Rocha, A. V., van de Weg, M. J., and Shaver, G. (2012). Vegetation shifts observed in arctic tundra 17 years after fire. *Remote Sensing Letters*, 3(8):729–736.
- Bartsch, A., Balzter, H., and George, C. (2009). The influence of regional surface soil moisture anomalies on forest fires in Siberia observed from satellites. *Environmental Research Letters*, 4(4):045021.
- Beck, P. S. A. and Goetz, S. J. (2011). Satellite observations of high northern latitude vegetation productivity changes between 1982 and 2008: ecological variability and regional differences. *Environmental Research Letters*, 6(4):045501.
- Brandt, J. P., Flannigan, M. D., Maynard, D. G., Thompson, I. D., and Volney, W. J. A. (2013). An introduction to Canada’s boreal zone: ecosystem processes, health, sustainability, and environmental issues. *Environmental Reviews*, 21(4):207–226.
- Bright, B. C., Hudak, A. T., Kennedy, R. E., Braaten, J. D., and Khalyani, A. H. (2019). Examining post-fire vegetation recovery with Landsat time series analysis in three western North American forest types. *Fire Ecology*, 15(1):1–14.
- Brown, J., Ferrians Jr, O. J., Heginbottom, J. A., and Melnikov, E. S. (1997). *Circum-Arctic map of permafrost and ground-ice conditions*. US Geological Survey Reston, VA.
- Brown, R. D. and Robinson, D. A. (2011). Northern Hemisphere spring snow cover variability and change over 1922–2010 including an assessment of uncertainty. *The Cryosphere*, 5(1):219–229.
- Carlson, T. N. and Ripley, D. A. (1997). On the relation between NDVI, fractional vegetation cover, and leaf area index. *Remote sensing of Environment*, 62(3):241–252.
- Chander, G., Markham, B. L., and Helder, D. L. (2009). Summary of current radiometric calibration coefficients for landsat MSS, TM, ETM+, and EO-1 ALI Sensors. *Remote sensing of environment*, 113(5):893–903.

Bibliography

- Chen, X., Vogelmann, J. E., Rollins, M., Ohlen, D., Key, C. H., Yang, L., Huang, C., and Shi, H. (2011). Detecting post-fire burn severity and vegetation recovery using multitemporal remote sensing spectral indices and field-collected composite burn index data in a ponderosa pine forest. *International Journal of Remote Sensing*, 32(23):7905–7927.
- Chu, T., Guo, X., and Takeda, K. (2017). Effects of burn severity and environmental conditions on post-fire regeneration in siberian larch forest. *Forests*, 8(3):76.
- Cohen, J., Screen, J. A., Furtado, J. C., Barlow, M., Whittleston, D., Coumou, D., Francis, J., Dethloff, K., Entekhabi, D., and Overland, J. (2014). Recent arctic amplification and extreme mid-latitude weather. *Nature geoscience*, 7(9):627–637.
- Cohen, W. B., Yang, Z., Healey, S. P., Kennedy, R. E., and Gorelick, N. (2018). A LandTrendr multispectral ensemble for forest disturbance detection. *Remote Sensing of Environment*, 205:131–140.
- de Groot, W. J., Flannigan, M. D., and Cantin, A. S. (2013). Climate change impacts on future boreal fire regimes. *Forest Ecology and Management*, 294:35–44.
- Duncan, B. N., Ott, L. E., Abshire, J. B., Brucker, L., Carroll, M. L., Carton, J., Comiso, J. C., Dinnat, E. P., Forbes, B. C., Gonsamo, A., et al. (2020). Space-based observations for understanding changes in the arctic-boreal zone. *Reviews of Geophysics*, 58(1):e2019RG000652.
- Epting, J., Verbyla, D., and Sorbel, B. (2005). Evaluation of remotely sensed indices for assessing burn severity in interior alaska using landsat TM and ETM+. *Remote Sensing of Environment*, 96(3-4):328–339.
- Escuin, S., Navarro, R., and Fernandez, P. (2008). Fire severity assessment by using NBR (Normalized Burn Ratio) and NDVI (Normalized Difference Vegetation Index) derived from Landsat TM/ETM images. *International Journal of Remote Sensing*, 29(4):1053–1073.
- Fernandes, R. and Leblanc, S. G. (2005). Parametric (modified least squares) and non-parametric (theil-sen) linear regressions for predicting biophysical parameters in the presence of measurement errors. *Remote Sensing of Environment*, 95(3):303–316.
- Forkel, M., Thonicke, K., Beer, C., Cramer, W., Bartalev, S., and Schmullius, C. (2012). Extreme fire events are related to previous-year surface moisture conditions in permafrost-underlain larch forests of Siberia. *Environmental Research Letters*, 7(4):044021.
- Fraser, R. H., Olthof, I., Kokelj, S. V., Lantz, T. C., Lacelle, D., Brooker, A., Wolfe, S., and Schwarz, S. (2014). Detecting landscape changes in high latitude environments using Landsat trend analysis: 1. Visualization. *Remote Sensing*, 6(11):11533–11557.
- French, H. M. (1999). *Permafrost*, pages 472–476. Springer Netherlands, Dordrecht.
- Garcia, M. L. and Caselles, V. (1991). Mapping burns and natural reforestation using Thematic Mapper data. *Geocarto International*, 6(1):31–37.

Bibliography

- Gauthier, S., Bernier, P., Kuuluvainen, T., Shvidenko, A., and Schepaschenko, D. (2015). Boreal forest health and global change. *Science*, 349(6250):819–822.
- Gibson, C., Olefeldt, D., Flannigan, M., Chasmer, L., and Thompson, D. K. (2016). Long term effects of wildfire on permafrost stability and carbon cycling in peatlands. In *AGU Fall Meeting Abstracts*, volume 2016, pages B53G–0584.
- Gibson, C. M., Chasmer, L. E., Thompson, D. K., Quinton, W. L., Flannigan, M. D., and Olefeldt, D. (2018). Wildfire as a major driver of recent permafrost thaw in boreal peatlands. *Nature communications*, 9(1):1–9.
- Goetz, S. J., Epstein, H. E., Bhatt, U. S., Jia, G. J., Kaplan, J. O., Lischke, H., Yu, Q., Bunn, A., Lloyd, A. H., Alcaraz-Segura, D., et al. (2010). Recent changes in Arctic vegetation: satellite observations and simulation model predictions. In *Eurasian Arctic land cover and land use in a changing climate*, pages 9–36. Springer.
- Gorelick, N., Hancher, M., Dixon, M., Ilyushchenko, S., Thau, D., and Moore, R. (2017). Google Earth Engine: Planetary-scale geospatial analysis for everyone. *Remote sensing of Environment*, 202:18–27.
- Gorokhov, A. and Fedorov, A. (2018). Current trends in climate change in Yakutia. *Geography and Natural Resources*, 39(2):153–161.
- Goward, S., Arvidson, T., Williams, D., Faundeen, J., Irons, J., and Franks, S. (2006). Historical record of Landsat global coverage. *Photogrammetric Engineering & Remote Sensing*, 72(10):1155–1169.
- Griffiths, P., Kuemmerle, T., Kennedy, R. E., Abrudan, I. V., Knorn, J., and Hostert, P. (2012). Using annual time-series of Landsat images to assess the effects of forest restitution in post-socialist Romania. *Remote Sensing of Environment*, 118:199–214.
- Guo, M., Li, J., Wen, L., and Huang, S. (2019). Estimation of CO₂ emissions from wildfires using OCO-2 data. *Atmosphere*, 10(10):581.
- Heim, R. J., Bucharova, A., Brodt, L., Kamp, J., Rieker, D., Soromotin, A. V., Yurtaev, A., and Hölzel, N. (2021). Post-fire vegetation succession in the Siberian subarctic tundra over 45 years. *Science of The Total Environment*, 760:143425.
- Hinzman, L. D., Bettez, N. D., Bolton, W. R., Chapin, F. S., Dyurgerov, M. B., Fastie, C. L., Griffith, B., Hollister, R. D., Hope, A., Huntington, H. P., et al. (2005). Evidence and implications of recent climate change in northern Alaska and other arctic regions. *Climatic change*, 72(3):251–298.
- Hollingsworth, T. N., Breen, A. L., Hewitt, R. E., and Mack, M. C. (2021). Does fire always accelerate shrub expansion in Arctic tundra? Examining a novel grass-dominated successional trajectory on the Seward Peninsula. *Arctic, Antarctic, and Alpine Research*, 53(1):93–109.

Bibliography

- Holloway, J. E., Lewkowicz, A. G., Douglas, T. A., Li, X., Turetsky, M. R., Baltzer, J. L., and Jin, H. (2020). Impact of wildfire on permafrost landscapes: A review of recent advances and future prospects. *Permafrost and Periglacial Processes*, 31(3):371–382.
- Hu, Y., Fernandez-Anez, N., Smith, T. E., and Rein, G. (2018). Review of emissions from smouldering peat fires and their contribution to regional haze episodes. *International Journal of Wildland Fire*, 27(5):293–312.
- Hu, Y. and Hu, Y. (2020). Detecting forest disturbance and recovery in Primorsky Krai, Russia, using annual Landsat time series and multi-source land cover products. *Remote Sensing*, 12(1):129.
- Hugelius, G., Loisel, J., Chadburn, S., Jackson, R. B., Jones, M., MacDonald, G., Marushchak, M., Olefeldt, D., Packalen, M., Siewert, M. B., et al. (2020). Large stocks of peatland carbon and nitrogen are vulnerable to permafrost thaw. *Proceedings of the National Academy of Sciences*, 117(34):20438–20446.
- Ivanova, G., Ivanov, V., Kukavskaya, E., and Soja, A. (2010). The frequency of forest fires in Scots pine stands of Tuva, Russia. *Environmental Research Letters*, 5(1):015002.
- Jiménez-Muñoz, J. C., Cristóbal, J., Sobrino, J. A., Sòria, G., Ninyerola, M., and Pons, X. (2008). Revision of the single-channel algorithm for land surface temperature retrieval from Landsat thermal-infrared data. *IEEE Transactions on geoscience and remote sensing*, 47(1):339–349.
- Jiménez-Muñoz, J. C. and Sobrino, J. A. (2003). A generalized single-channel method for retrieving land surface temperature from remote sensing data. *Journal of geophysical research: atmospheres*, 108(D22).
- Jiménez-Muñoz, J. C., Sobrino, J. A., Skoković, D., Mattar, C., and Cristóbal, J. (2014). Land surface temperature retrieval methods from Landsat-8 thermal infrared sensor data. *IEEE Geoscience and remote sensing letters*, 11(10):1840–1843.
- Jin, H., Sun, G., Yu, S., Jin, R., and He, R. (2008). Symbiosis of marshes and permafrost in Da and Xiao Hinggan Mountains in northeastern China. *Chinese Geographical Science*, 18(1):62–69.
- Kalliokoski, T., Aalto, T., Bäck, J., Ezhova, E., Franz, D., Haapanala, S., Juurola, E., Kerminen, V.-M., Kolari, P., Kulmala, L., et al. (2019). Carbon sink and CarbonSink+: from observations to global potential.
- Keeley, J. E. (2009). Fire intensity, fire severity and burn severity: a brief review and suggested usage. *International journal of wildland fire*, 18(1):116–126.
- Kennedy, R. E., Yang, Z., and Cohen, W. B. (2010). Detecting trends in forest disturbance and recovery using yearly Landsat time series: 1. LandTrendr—Temporal segmentation algorithms. *Remote Sensing of Environment*, 114(12):2897–2910.
- Key, C. H. and Benson, N. C. (2006). Landscape assessment (LA). In: *Lutes, Duncan C.; Keane, Robert E.; Caratti, John F.; Key, Carl H.; Benson, Nathan C.; Sutherland, Steve; Gangi, Larry*

Bibliography

- J. 2006. FIREMON: Fire effects monitoring and inventory system. Gen. Tech. Rep. RMRS-GTR-164-CD. Fort Collins, CO: US Department of Agriculture, Forest Service, Rocky Mountain Research Station. p. LA-1-55, 164.
- Kharuk, V., Kasischke, E. S., and Yakubailik, O. (2007). The spatial and temporal distribution of fires on Sakhalin Island, Russia. *International Journal of Wildland Fire*, 16(5):556–562.
- Kharuk, V. and Ponomarev, E. (2017). Spatiotemporal characteristics of wildfire frequency and relative area burned in larch-dominated forests of Central Siberia. *Russian Journal of Ecology*, 48(6):507–512.
- Kharuk, V. I., Dvinskaya, M. L., Petrov, I. A., Im, S. T., and Ranson, K. J. (2016). Larch forests of middle Siberia: long-term trends in fire return intervals. *Regional environmental change*, 16(8):2389–2397.
- Kim, Y., Kimball, J. S., Zhang, K., and McDonald, K. C. (2012). Satellite detection of increasing Northern Hemisphere non-frozen seasons from 1979 to 2008: Implications for regional vegetation growth. *Remote Sensing of Environment*, 121:472–487.
- Kolden, C. A. and Rogan, J. (2013). Mapping wildfire burn severity in the Arctic tundra from down-sampled MODIS data. *Arctic, Antarctic, and Alpine Research*, 45(1):64–76.
- Kovacs, K., Ranson, K. J., Sun, G., and Kharuk, V. I. (2004). The relationship of the terra MODIS fire product and anthropogenic features in the central Siberian landscape. *Earth Interactions*, 8(18):1–25.
- Krylov, A., McCarty, J. L., Potapov, P., Loboda, T., Tyukavina, A., Turubanova, S., and Hansen, M. C. (2014). Remote sensing estimates of stand-replacement fires in Russia, 2002–2011. *Environmental Research Letters*, 9(10):105007.
- Lantz, T. C., Gergel, S. E., and Henry, G. H. (2010). Response of green alder (*Alnus viridis* subsp. *fruticosa*) patch dynamics and plant community composition to fire and regional temperature in north-western Canada. *Journal of Biogeography*, 37(8):1597–1610.
- Lentile, L. B., Morgan, P., Hudak, A. T., Bobbitt, M. J., Lewis, S. A., Smith, A. M., and Robichaud, P. R. (2007). Post-fire burn severity and vegetation response following eight large wildfires across the western United States. *Fire Ecology*, 3(1):91–108.
- Lhermitte, S., Verbesselt, J., Verstraeten, W. W., and Coppin, P. (2010). A pixel based regeneration index using time series similarity and spatial context. *Photogrammetric Engineering & Remote Sensing*, 76(6):673–682.
- Li, X., Jin, H., He, R., Huang, Y., Wang, H., Luo, D., Jin, X., Lü, L., Wang, L., Li, W., et al. (2019). Effects of forest fires on the permafrost environment in the northern Da Xing’anling (Hinggan) mountains, Northeast China. *Permafrost and Periglacial Processes*, 30(3):163–177.
- Li, X.-Y., Jin, H.-J., Wang, H.-W., Marchenko, S. S., Shan, W., Luo, D.-L., He, R.-X., Spektor, V., Huang, Y.-D., Li, X.-Y., et al. (2021). Influences of forest fires on the permafrost environment: A review. *Advances in Climate Change Research*.

Bibliography

- Li, X.-z., Xu-gao, W., Yuan-man, H. U., Fan-hua, K., and Fu-ju, X. (2004). Influence of forest fire on vegetational succession in Daxing'anling. *Journal-Fujian College of Forestry*, 24(2):182–187.
- Li, Z.-L., Tang, B.-H., Wu, H., Ren, H., Yan, G., Wan, Z., Trigo, I. F., and Sobrino, J. A. (2013a). Satellite-derived land surface temperature: Current status and perspectives. *Remote sensing of environment*, 131:14–37.
- Li, Z.-L., Wu, H., Wang, N., Qiu, S., Sobrino, J. A., Wan, Z., Tang, B.-H., and Yan, G. (2013b). Land surface emissivity retrieval from satellite data. *International Journal of Remote Sensing*, 34(9-10):3084–3127.
- McCarty, J. L., Smith, T. E. L., and Turetsky, M. R. (2020). Arctic fires re-emerging. *Nature Geoscience*, 13(10):658–660.
- Miller, J. D. and Thode, A. E. (2007). Quantifying burn severity in a heterogeneous landscape with a relative version of the delta Normalized Burn Ratio (dNBR). *Remote Sensing of Environment*, 109(1):66–80.
- Moritz, M. A., Parisien, M.-A., Batllori, E., Krawchuk, M. A., Van Dorn, J., Ganz, D. J., and Hayhoe, K. (2012). Climate change and disruptions to global fire activity. *Ecosphere*, 3(6):1–22.
- Murton, J. B., Edwards, M. E., Lozhkin, A. V., Anderson, P. M., Savvinov, G. N., Bakulina, N., Bondarenko, O. V., Cherepanova, M. V., Danilov, P. P., Boeskorov, V., et al. (2017). Preliminary paleoenvironmental analysis of permafrost deposits at Batagaika megaslump, Yana uplands, northeast Siberia. *Quaternary Research*, 87(2):314–330.
- Nil, L., Ullmann, T., Kneisel, C., Sobiech-Wolf, J., and Baumhauer, R. (2019). Assessing spatiotemporal variations of Landsat land surface temperature and multispectral indices in the Arctic Mackenzie delta region between 1985 and 2018. *Remote Sensing*, 11(19):2329.
- Nossov, D. R., Jorgenson, M. T., Kielland, K., and Kanevskiy, M. Z. (2013). Edaphic and microclimatic controls over permafrost response to fire in interior Alaska. *Environmental Research Letters*, 8(3):035013.
- Oris, F., Asselin, H., Ali, A. A., Finsinger, W., and Bergeron, Y. (2014). Effect of increased fire activity on global warming in the boreal forest. *Environmental Reviews*, 22(3):206–219.
- Parastatidis, D., Mitraka, Z., Chrysoulakis, N., and Abrams, M. (2017). Online global land surface temperature estimation from Landsat. *Remote sensing*, 9(12):1208.
- Parks, S. A., Dillon, G. K., and Miller, C. (2014). A new metric for quantifying burn severity: the relativized burn ratio. *Remote Sensing*, 6(3):1827–1844.
- Parks, S. A., Holsinger, L. M., Voss, M. A., Loehman, R. A., and Robinson, N. P. (2018). Mean composite fire severity metrics computed with Google Earth Engine offer improved accuracy and expanded mapping potential. *Remote Sensing*, 10(6):879.

Bibliography

- Pearson, R. G., Phillips, S. J., Loranty, M. M., Beck, P. S., Damoulas, T., Knight, S. J., and Goetz, S. J. (2013). Shifts in Arctic vegetation and associated feedbacks under climate change. *Nature climate change*, 3(7):673–677.
- Philipp, M., Dietz, A., Buchelt, S., and Kuenzer, C. (2021). Trends in satellite earth observation for permafrost related analyses—A Review. *Remote Sensing*, 13(6):1217.
- Ponomarev, E., Masyagina, O., Litvintsev, K., Ponomareva, T., Shvetsov, E., and Finnikov, K. (2020). The effect of post-fire disturbances on a seasonally thawed layer in the permafrost larch forests of central Siberia. *Forests*, 11(8):790.
- Ponomarev, E., Shvetsov, E., and Kharuk, V. (2018a). The intensity of wildfires in fire emissions estimates. *Russian Journal of Ecology*, 49(6):492–499.
- Ponomarev, E., Shvetsov, E., and Usataya, Y. O. (2018b). Determination of the energy properties of wildfires in Siberia by remote sensing. *Izvestiya, Atmospheric and Oceanic Physics*, 54(9):979–985.
- Ponomarev, E. I., Kharuk, V. I., and Ranson, K. J. (2016). Wildfires dynamics in Siberian larch forests. *Forests*, 7(6):125.
- Pörtner, H.-O., Roberts, D. C., Masson-Delmotte, V., Zhai, P., Tignor, M., Poloczanska, E., Mintenbeck, K., Nicolai, M., Okem, A., Petzold, J., et al. (2019). IPCC special report on the ocean and cryosphere in a changing climate. *IPCC Intergovernmental Panel on Climate Change: Geneva, Switzerland*, 1(3).
- Quintero, N., Viedma, O., Urbieto, I. R., and Moreno, J. M. (2019). Assessing landscape fire hazard by multitemporal automatic classification of Landsat time series using the Google Earth Engine in West-Central Spain. *Forests*, 10(6):518.
- Randerson, J. T., Liu, H., Flanner, M. G., Chambers, S. D., Jin, Y., Hess, P. G., Pfister, G., Mack, M. C., Treseder, K. K., Welp, L. R., et al. (2006). The impact of boreal forest fire on climate warming. *science*, 314(5802):1130–1132.
- Rocha, A. V., Loranty, M. M., Higuera, P. E., Mack, M. C., Hu, F. S., Jones, B. M., Breen, A. L., Rastetter, E. B., Goetz, S. J., and Shaver, G. R. (2012). The footprint of Alaskan tundra fires during the past half-century: implications for surface properties and radiative forcing. *Environmental Research Letters*, 7(4):044039.
- Romps, D. M., Seeley, J. T., Vollaro, D., and Molinari, J. (2014). Projected increase in lightning strikes in the United States due to global warming. *Science*, 346(6211):851–854.
- Rosas, J., Houborg, R., and McCabe, M. F. (2017). Sensitivity of Landsat 8 surface temperature estimates to atmospheric profile data: A study using modtran in dryland irrigated systems. *Remote Sensing*, 9(10):988.
- Sapozhnikov, V. and Krechetov., A. (1982). Meteorological and geophysical aspects of underground cables lightning damage. *In Atmospheric electricity*, page 256–258.

Bibliography

- Schuur, E. A., McGuire, A. D., Schädel, C., Grosse, G., Harden, J., Hayes, D. J., Hugelius, G., Koven, C. D., Kuhry, P., Lawrence, D. M., et al. (2015). Climate change and the permafrost carbon feedback. *Nature*, 520(7546):171–179.
- Sekertekin, A. and Bonafoni, S. (2020). Sensitivity analysis and validation of daytime and nighttime land surface temperature retrievals from Landsat 8 using different algorithms and emissivity models. *Remote Sensing*, 12(17):2776.
- Sen, P. K. (1968). Estimates of the regression coefficient based on Kendall’s tau. *Journal of the American statistical association*, 63(324):1379–1389.
- Serreze, M. C. and Barry, R. G. (2011). Processes and impacts of Arctic amplification: A research synthesis. *Global and planetary change*, 77(1-2):85–96.
- Shvetsov, E., Ponomarev, E. I., Kharuk, V., and Ponomareva, T. (2019). Monitoring of post-fire effects and vegetation recovery in larch forests of Central Siberia using remote sensing observations. In *AGU Fall Meeting Abstracts*, volume 2019, pages GC21E–1282.
- Sizov, O., Ezhova, E., Tsymbarovich, P., Soromotin, A., Prihod’ko, N., Petäjä, T., Zilitinkevich, S., Kulmala, M., Bäck, J., and Köster, K. (2021). Fire and vegetation dynamics in northwest Siberia during the last 60 years based on high-resolution remote sensing. *Biogeosciences*, 18(1):207–228.
- Sobrino, J. A., Jiménez-Muñoz, J. C., and Paolini, L. (2004). Land surface temperature retrieval from Landsat TM 5. *Remote Sensing of environment*, 90(4):434–440.
- Sobrino, J. A., Jiménez-Muñoz, J. C., Sòria, G., Romaguera, M., Guanter, L., Moreno, J., Plaza, A., and Martínez, P. (2008). Land surface emissivity retrieval from different VNIR and TIR sensors. *IEEE transactions on geoscience and remote sensing*, 46(2):316–327.
- Stone, M. (2020). A heat wave thawed siberia’s tundra. now, it’s on fire. *National Geographic*.
- Stow, D. A., Hope, A., McGuire, D., Verbyla, D., Gamon, J., Huemmrich, F., Houston, S., Racine, C., Sturm, M., Tape, K., et al. (2004). Remote sensing of vegetation and land-cover change in Arctic Tundra Ecosystems. *Remote sensing of environment*, 89(3):281–308.
- Theil, H. (1992). A rank-invariant method of linear and polynomial regression analysis. In *Henri Theil’s contributions to economics and econometrics*, pages 345–381. Springer.
- Trofaier, A. M., Westermann, S., and Bartsch, A. (2017). Progress in space-borne studies of permafrost for climate science: Towards a multi-ECV approach. *Remote Sensing of Environment*, 203:55–70.
- Veraverbeke, S., Stavros, E. N., and Hook, S. J. (2014). Assessing fire severity using imaging spectroscopy data from the airborne visible/infrared imaging spectrometer (AVIRIS) and comparison with multispectral capabilities. *Remote Sensing of Environment*, 154:153–163.
- Viereck, L. A. (1982). *Effects of fire and firelines on active layer thickness and soil temperatures in interior Alaska*. US Forest Service.

Bibliography

- Viereck, L. A., Werdin-Pfisterer, N. R., Adams, P. C., and Yoshikawa, K. (2008). Effect of wildfire and fireline construction on the annual depth of thaw in a black spruce permafrost forest in interior Alaska: a 36-year record of recovery. In *In: Kane, Douglas L.; Hinkel, Kenneth M., eds. Proceedings of the Ninth International Conference on Permafrost; June 29-July 3, 2008; Fairbanks, AK: 1845-1850.*
- Vlassova, L., Perez-Cabello, F., Nieto, H., Martín, P., Riaño, D., and De La Riva, J. (2014). Assessment of methods for land surface temperature retrieval from Landsat-5 TM images applicable to multiscale tree-grass ecosystem modeling. *Remote Sensing*, 6(5):4345–4368.
- Voigt, C., Lamprecht, R. E., Marushchak, M. E., Lind, S. E., Novakovskiy, A., Aurela, M., Martikainen, P. J., and Biasi, C. (2017). Warming of subarctic tundra increases emissions of all three important greenhouse gases-carbon dioxide, methane, and nitrous oxide. *Global Change Biology*, 23(8):3121–3138.
- Wang, F., Qin, Z., Song, C., Tu, L., Karnieli, A., and Zhao, S. (2015). An improved mono-window algorithm for land surface temperature retrieval from Landsat 8 thermal infrared sensor data. *Remote sensing*, 7(4):4268–4289.
- Westermann, S., Duguay, C. R., Grosse, G., and Kääb, A. (2015). 13 remote sensing of permafrost and frozen ground.
- Yoshikawa, K., Bolton, W. R., Romanovsky, V. E., Fukuda, M., and Hinzman, L. D. (2002). Impacts of wildfire on the permafrost in the boreal forests of interior Alaska. *Journal of Geophysical Research: Atmospheres*, 107(D1):FFR–4.
- Zhao, S., Zhang, S., Cheng, W., and Zhou, C. (2019). Model simulation and prediction of decadal mountain permafrost distribution based on remote sensing data in the Qilian Mountains from the 1990s to the 2040s. *Remote Sensing*, 11(2):183.
- Zhu, L., Liu, X., Wu, L., Tang, Y., and Meng, Y. (2019). Long-term monitoring of cropland change near Dongting lake, China, using the LandTrendr algorithm with landsat imagery. *Remote Sensing*, 11(10):1234.
- Zhu, Z. and Woodcock, C. E. (2014). Continuous change detection and classification of land cover using all available Landsat data. *Remote sensing of Environment*, 144:152–171.